

**Experimental investigations of the lunar photoelectron
environment and related dust dynamics**

by

Adrienne Rathert Dove

B.S., University of Missouri, Columbia, 2006

M.S., University of Colorado, 2009

A thesis submitted to the
Faculty of the Graduate School of the
University of Colorado in partial fulfillment
of the requirements for the degree of
Doctor of Philosophy
Department of Astrophysical and Planetary Sciences

2012

This thesis entitled:
Experimental investigations of the lunar photoelectron environment and related dust dynamics
written by Adrienne Rathert Dove
has been approved for the Department of Astrophysical and Planetary Sciences

Mihály Horányi

Scott Robertson

Frances Bagenal

David Brain

Jack Burns

Date _____

The final copy of this thesis has been examined by the signatories, and we find that both the content and the form meet acceptable presentation standards of scholarly work in the above mentioned discipline.

Dove, Adrienne Rathert (Ph.D., Planetary Science)

Experimental investigations of the lunar photoelectron environment and related dust dynamics

Thesis directed by Prof. Mihály Horányi

Airless bodies in space are exposed to a variety of charging environments in which a balance of currents due to plasma processes determines the surface charge. In the inner solar system, photoelectron emission is the dominant charging process on sunlit surfaces due to the intense solar UV radiation. This results in a positive surface potential with a photoelectron sheath above the surface. Conversely, the unlit side of the body will charge negatively due the collection of the fast-moving solar wind electrons. The interaction of charged dust grains with these positively and negatively charged surfaces, and with the photoelectron and plasma sheaths, may explain the occurrence of dust lofting, levitation and transport above the lunar surface and on other airless bodies. This dust has been recognized as a potential hazard to future exploration of dusty planetary surfaces, due to its abrasive and adhesive nature.

In this thesis, the initial investigation explores the mechanisms that control adhesion of dust grains to insulating and conducting surfaces. Unfortunately, there is little known about the mechanisms of adhesion on widely varying surface types, but van der Waals and electrostatic forces are the dominant forces that are taken into consideration in these studies, which measures the adhesive forces between $\leq 25 \mu\text{m}$ JSC-1 lunar simulant grains and various surfaces in vacuum using a centrifugal force detachment method. UV irradiation effects on surface adhesion were also examined.

In order to better understand the plasma processes at work on sunlit surfaces, we have performed laboratory experiments to study the physics of photoelectron sheaths above both conducting and insulating surfaces in vacuum. The first set of experiments determines the characteristics of photoelectron sheaths generated over a conducting Zr surface that is large in comparison to the Debye length of the sheath. These characteristics are derived from cylindrical Langmuir probe

measurements, and are compared with the results from 1D PIC-code simulations to gain a greater understanding of the sheath physics. To study the photoelectron sheath above an insulating material, a portion of this conducting surface is covered with insulating material. CeO_2 is used both in powdered and solid disk form, and un-sieved JSC-1 is used to represent planetary surfaces. Electron densities and temperatures of the photoelectron plasma are measured with a single-sided planar Langmuir probe. The measurements taken above the CeO_2 are compared with those taken above the Zr to observe the differences in photoemission, and to determine how the insulating surface modifies the structure of the photoelectron sheath. The densities above the surfaces are only found to have a modest dependence on the surrounding surface bias, and the plasma potentials measured above the insulating surfaces are significantly different than those above the Zr, due to the fact that the insulating materials float to an equilibrium potential independent of the surrounding surface bias. These measurements indicate that plasma probes above a planetary body can accurately determine potentials and densities above the surfaces, valuable information for understanding the charging environment of spacecraft and other objects.

Dedication

To my grandpa and papaw, who will not see this, but without whom I would not be here ... who showed me the beauty of building things by hand, how to use the air brake on a car, that sometimes it's good to clown around, and that you will find luck if you know where to look.

Acknowledgements

This is the product of an endeavor that started many years ago when I first fell in love with space, and through the years I have been felt nothing but encouragement to pursue whichever path I chose.

To my advisors and mentors: Brian, Jen, and Chris, who encouraged me from the beginning; Jack, who has been a strong advocate and a great resource; Scott, who showed me how to work and have fun in the lab; and Mihály, who is an endless source of ideas and enthusiasm, and who I have been privileged to work with. To Zoltan, who really started this by inviting me to come watch a fun movie about dust on the Moon. To Xu, who showed me that its a good idea to just start an experiment, even if you don't know what will happen, and with whom I have had excellent discussions about plasma probes and life.

To my theoretical sidekick Andrew, who has an unquenchable love of plasma physics, and Shannon, who has made these past few years in the lab so much more enjoyable. To all of my friends and teammates who have made my years at grad school some of the best of my life.

And finally, to my family. To Kathy, Alex, and Mamaw, I am so glad we could spend these years so close to each other. To Justin, for sticking with me through the ups and inevitable downs that come with this path, and believing in me wholeheartedly. And to my parents, who have always provided immense support, love, and encouragement, even when I told them I was going to do something crazy like jump out of an airplane or get a Ph.D.

Contents

Chapter

1	Introduction	1
1.1	Lunar plasma and dust environment	1
1.1.1	Lunar surface observations	3
1.2	Sheaths	7
1.2.1	Plasma sheaths	7
1.2.2	Photoelectron sheaths	9
1.3	Previous relevant work	10
1.3.1	Theoretical	10
1.3.2	Experimental	11
1.4	Thesis motivation and structure	19
2	Mitigation of dust adhesion to surfaces by surface modification	22
2.1	Theory and background	23
2.2	Surface modification	25
2.2.1	Materials	26
2.2.2	Contact angles	26
2.2.3	Surface properties	27
2.3	Contact charging	27
2.4	Adhesion experiments	28

2.4.1	Experimental setup	28
2.4.2	Less than 25 μm JSC-1	33
2.4.3	Less than 25 μm LHT	36
2.4.4	UV-irradiated substrates	37
2.5	Discussion of adhesion results	38
3	Experimental apparatus and data analysis	41
3.1	Description of the apparatus	41
3.2	Langmuir probe operation and theory	44
3.2.1	Characteristic Langmuir probe traces	45
3.2.2	Probe current equations	49
3.2.3	Langmuir probe analysis	51
3.3	Characterizing the electron populations in the chamber	52
3.3.1	Diagnostics with the Zr table	53
4	Experimental studies of photoemission above a Zr surface	59
4.1	Apparatus	60
4.1.1	Photoemission Probe	61
4.1.2	Langmuir Probe	62
4.2	Experimental results	63
4.2.1	Current-voltage characteristics of the emitting surface	63
4.2.2	Langmuir probe data	67
4.3	Density profiles in photoelectron sheaths	70
4.4	Discussion of Zr surface photoelectron sheath results	72
5	Photoelectron plasmas above insulating surfaces with varied material properties	75
5.1	Charge balance of an insulating surface	76
5.2	Experimental Setup	76

5.3	Experimental results	79
5.3.1	Current measurements	79
5.3.2	Potential measurements	82
5.3.3	Densities	87
5.4	Discussion and conclusion	93
6	Summary and Future Work	96
6.1	Dust adhesion and surface modification	96
6.2	Photoelectron Sheaths	98
	Bibliography	103
	Appendix	
A	Additional diagnostic techniques and troubleshooting	109
A.1	Characterizing the photoelectron gas	109
A.2	Techniques to reduce the excess electron population	111
A.2.1	Diagnostics with a grid	111
A.2.2	Using a magnetic field to reduce the excess electron population	111
A.2.3	Combination of the biased grid and magnetic fields	114
A.3	Results of troubleshooting	121
B	Paper and presentations	124
B.1	Published papers	124
B.2	Papers in preparation	124
B.3	Selected Presentations	125

Tables

Table

2.1	Contact angles and surface energy	27
2.2	Contact charging measurements	28
2.3	Adhesion force and spinning speed of tests	35
2.4	Virgin and treated surface force differences	37
3.1	Data from the Zr surface swept beneath a biased grid	56
4.1	Comparison of photoelectron sheath parameters	65
4.2	Photoelectron characteristics determined from Langmuir probe sweeps above the Zr surface	69
5.1	Material Properties	79
5.2	Relative probe collection currents over insulating surfaces.	80
5.3	Relative photoemission currents over insulating surfaces.	80
5.4	Plasma properties derived from planar probe data over insulting surfaces.	83
A.1	Ratio of collection to emission current on the Zr table as a function of the current in the magnetic coils and the grid bias.	121
A.2	Voltage at the peak of the derivative of the (20-point smoothed) Zr table sweeps as a function of the current in the magnetic coils and the grid bias.	123

Figures

Figure

1.1	Lunar plasma environment	2
1.2	Surveyor lunar horizon glow images	4
1.3	CPLEE lunar eclipse observations	5
1.4	LEAM observations of impact events, from Colwell et al. (2007)	6
1.5	Plasma potentials and photoelectron sheath schematic	7
1.6	Photoemissive characteristics measured by Willis et al. (1973)	12
1.7	Schematic of the experimental setup from Sickafoose et al. (2001)	13
1.8	Photoemission from Zr surface from Sickafoose et al. (2001)	15
1.9	Schematic of experimental setup from Wang et al. (2008)	16
1.10	Probe sweeps and electron energy distributions from Wang et al. (2008)	17
1.11	Charge on Zn particles as a function of distance from a photocathode, from Sickafoose et al. (2001)	18
2.1	Contact charging measurements	29
2.2	Experimental setup for adhesion experiments	31
2.3	SEM images pre- and post-spin	31
2.4	Histogram of particle sizes pre- and post-spin	32
2.5	Adhesion results for JSC-1	34
2.6	Adhesion results on UV-exposed surfaces	38

3.1	Diagram of basic setup inside of the experimental chamber	42
3.2	Example Langmuir probe curves	46
3.3	Langmuir probe sweep with and without graphite from Wang et al. (2008)	48
3.4	Sample table sweeps and derivatives, illustrating the effect of the grid.	54
3.5	Table sweeps for varying grid biases	55
3.6	Floating potential on the table as a function of grid bias	57
4.1	Diagram of experimental apparatus	60
4.2	Measured photoemission current density from UV lamp sources	62
4.3	I-V curves from the Zr surface	64
4.4	Zr surface floating potentials as a function of grid bias	66
4.5	Cylindrical Langmuir probe sweeps above the Zr surface	68
4.6	Photoelectron population and density with height	71
4.7	Comparisons of 1-D PIC simulations with Langmuir probe measurements	73
5.1	Diagram and images of setup for insulator experiments	78
5.2	Probe sweeps over insulators and Zr when the Zr surface is biased to 0 V.	81
5.3	Floating potentials as a function of radial distance over the surface	84
5.4	Plasma potentials as a function of radial distance over the surface	86
5.5	Floating potentials as a function of surface bias.	88
5.6	Plasma potentials as a function of surface bias.	89
5.7	Density as a function of surface bias.	90
5.8	Electron density as a function of radial distance over the surface.	92
6.1	Sample Cassini Langmuir probe sweep from Olson et al. (2010)	99
A.1	Spherical probe sweeps near the wall and in the center of the chamber	110
A.2	Second derivatives of sweeps in Fig. A.1	112
A.3	New and old grid comparison sweeps	113

A.4 Spherical probe sweeps in the presence of a magnetic field	115
A.5 Effects of magnetic field direction	116
A.6 Effect of grid height on sweeps	118
A.7 Effect of magnetic fields on Zr surface sweeps	119
A.8 Derivatives of sweeps in Fig. A.7	120
A.9 New and old grid comparison sweeps	122

Chapter 1

Introduction

1.1 Lunar plasma and dust environment

Airless bodies in space are exposed to a variety of charging environments in which the surface charge is determined by a balance of plasma currents to and from the surface. As shown in Fig. 1.1, these charging processes on the lunar surface are ultimately driven by the Sun. Interactions with the solar wind provide the primary source of charged particles to much of the lunar surface, and on the lunar dayside, photoemission from the dusty regolith that is exposed to intense ultraviolet (UV) radiation becomes the dominant charging mechanism. This results in a net positive surface charge. The lunar night-side, however, charges predominantly negatively as fast-moving solar wind electrons impact the surface. Events such as solar storms and passages through the terrestrial magnetosheath add to the complexity of these charging environments, and these events may also create very strong electric fields at the lunar surface.

Plasma processes interact with a lunar surface that is made complex not only by topography, but also by the layer of regolith that covers most of the surface. Lunar regolith includes the finest fractions of the lunar soil, which have been produced by repeated meteorite bombardment onto the lunar surface over the course of the Moon's history. Today, micrometeorite bombardment continues to stir up the regolith, and potentially lofts a small percentage of that dust into the exosphere. Because the lunar regolith is an insulating material, it charges to a potential that balances the plasma currents to and from the surface of each particle. The presence of strong electric fields generated by these currents may also drive lofting, levitation, and/or motion of the dust above the

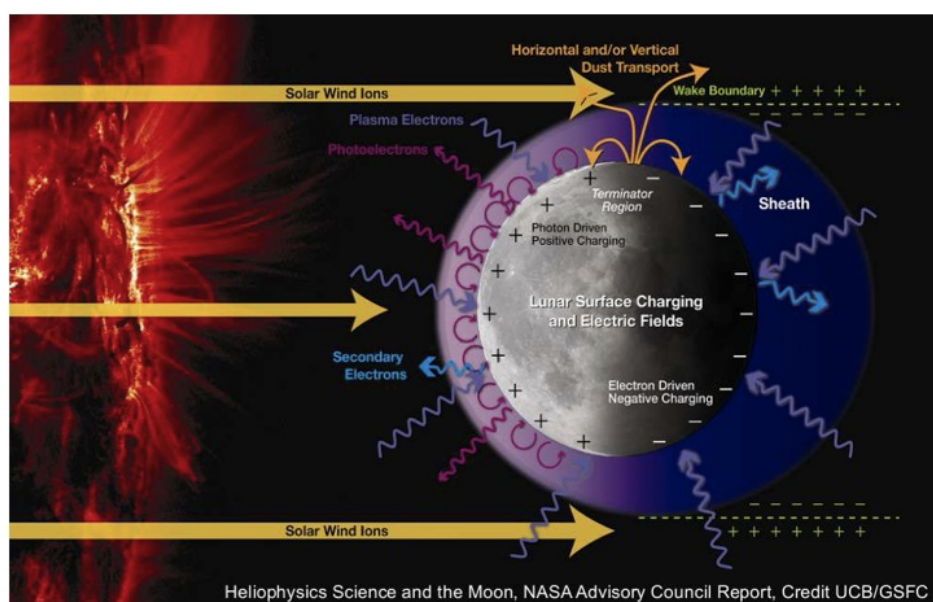


Figure 1.1: A broad overview of the plasma environment around the Moon, highlighting the importance of the Sun in driving these processes. [NAC/GSFC/UCB]

surface.

1.1.1 Lunar surface observations

Current interest in the interactions between the lunar near-surface plasma environment and the lunar regolith is primarily motivated by a handful of observations from instrumentation placed on the lunar surface. Prior to the Apollo missions, Surveyor 5, 6, and 7 landers observed a phenomena which occurred around lunar sunset, and has since been called the lunar “horizon glow”. The surveyor television cameras recorded images (Fig. 1.2) that Rennilson and Criswell (1974) interpreted to be lofted dust particles that were forward-scattering sunlight toward the cameras. Models using scattering theory predicted an average dust particle radius of 5-10 μm with an optical depth of $\tau \sim 10^{-6}$ being lofted a few tens of cm above the lunar surface. This height is similar to the Debye length above the surface, which further suggests that electrostatic levitation processes could play an important role.

Several instrument packages were left on the lunar surface by the Apollo missions to study the lunar dust and plasma environment. The Suprathermal Ion Detector Experiment (SIDE) measured the energy of ions at the lunar surface and found a dayside potential of about +10 V (Freeman and Ibrahim, 1975). Data from the Charged Particle Lunar Environment Experiment (CPLEE) detected electrons with energies of up to 200 V that had been accelerated through a potential above the lunar surface. Additionally, during a fortuitous total lunar eclipse, UV-stimulated photoemission ceased, and CPLEE measured a corresponding dropout of electrons (Fig. 1.3).

The Lunar Ejecta and Meteorites experiment was placed on the lunar surface to measure cosmic dust impacts, but instead measured a population of slow speed particles that is suggestive of transport above the lunar surface. As shown in Fig. 1.4, these events were strongly peaked at sunrise, with a smaller feature around sunset. Not only did this provide one of the most concrete pieces of evidence of dust motion above the lunar surface, but the imbalance in the sunrise and sunset rates also suggested that these micron-sized particles were experiencing net migration and transport.

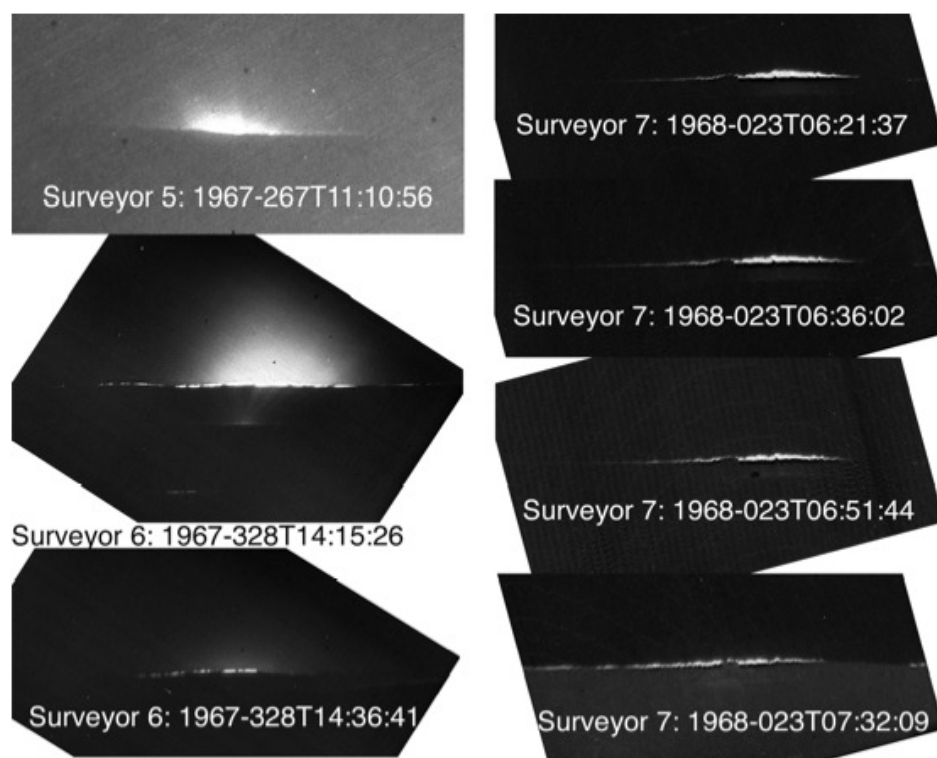


Figure 1.2: Unprocessed images of the lunar horizon glow from Surveyors 5, 6, and 7. Zodiacal light is seen in the images from Surveyors 5 and 6. From Colwell et al. (2007).

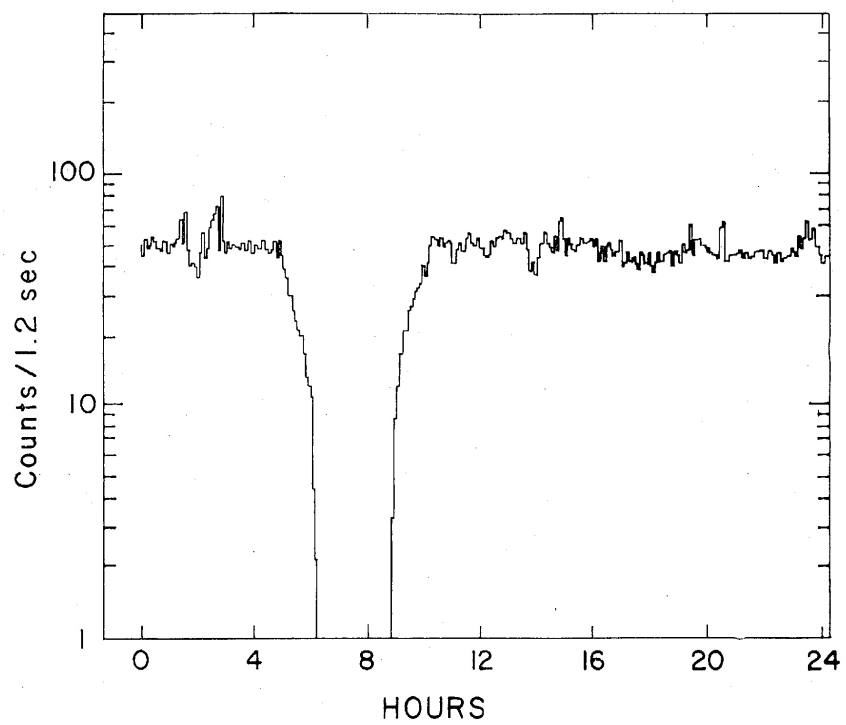


Figure 1.3: 5-min averaged count rate of 40 eV electrons measured by the Apollo 14 CPLEE instrument. A lunar eclipse is marked by the photoelectron signal dropout. From Reasoner and Burke (1973).

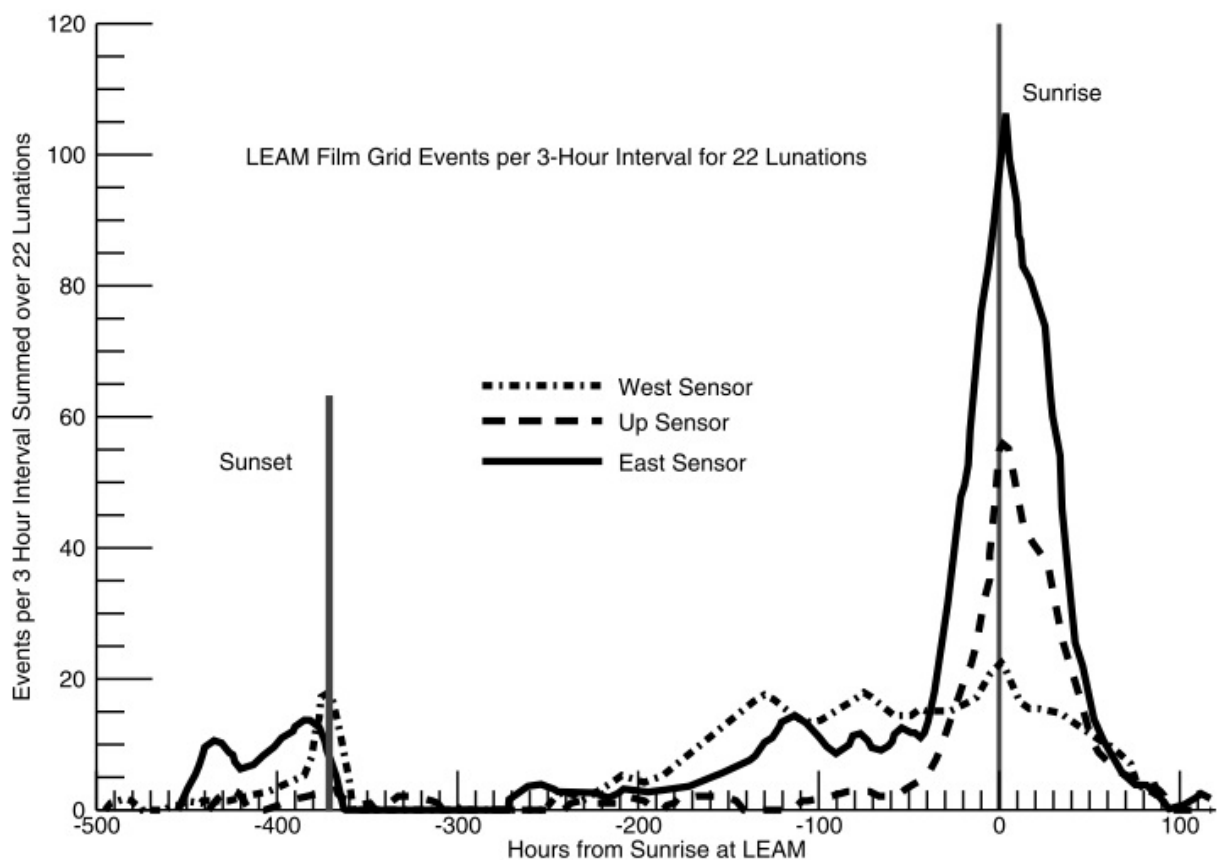


Figure 1.4: Number of impact events per 3-hour intervals integrated over 22 lunations. The large increases at terminator crossings persist for several hours before and after sunrise and before the smaller increase at sunset, suggesting particles may be launched on long trajectories from the terminator. From Colwell et al. (2007).

1.2 Sheaths

Surfaces exposed to plasma charge to an equilibrium floating potential controlled by current exchange between the surface and the near-surface plasma. In space, these currents are due to the incoming flux of particles from the solar wind, UV-induced photoemission, and secondary electron emission. On the lunar dayside, UV photoemission dominates, resulting in a net positive charge, while the nightside charges negatively due to the collection of solar wind electrons. These cases both result in the formation of a sheath, a region above the surface in which the potential changes over a characteristic length scale. In this section, we describe the basic physics behind sheath formation, and then focus on the specific case of photoelectron sheaths, which are the focus of this thesis.

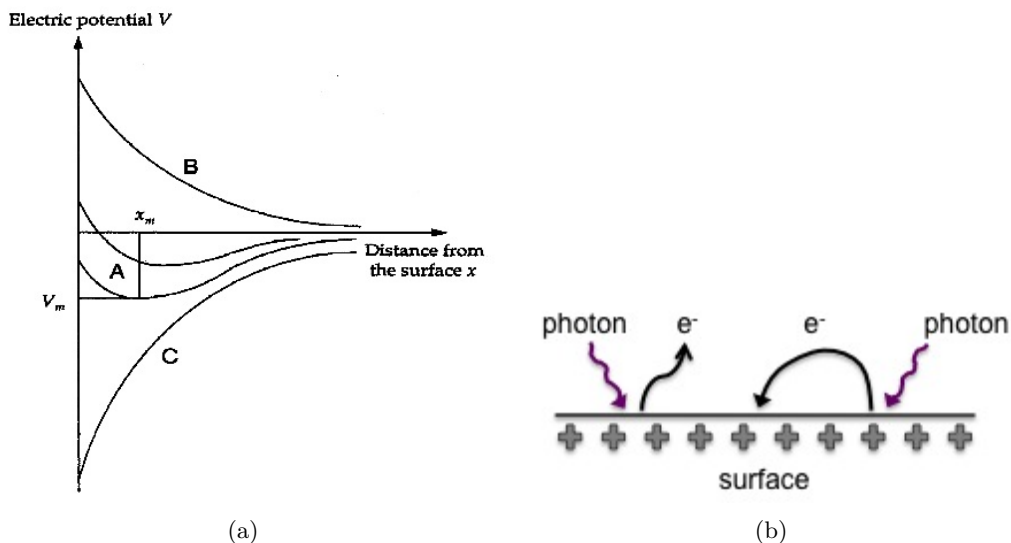


Figure 1.5: (a) Theory curves showing three possible cases of the plasma potential above a surface (from Nitter et al. (1998)), and (b) a cartoon illustrating the formation of a photoelectron sheath above a surface.

1.2.1 Plasma sheaths

Classical plasmas are quasi-neutral, meaning that the electron and ion densities are equal. Because electron thermal velocities are typically much greater than ion thermal velocities (this

is true in the solar wind), when exposed to a plasma, a surface will initially become negatively charged due to the more rapid collection electrons. This results in an imbalance within the plasma that creates a non-neutral layer above the surface called the plasma sheath. Within the sheath, the potential falls from the plasma potential to the surface potential so that the sheath effectively shields the bulk plasma from surface effects. The characteristic length scale for the sheath is given by the Debye length, which is defined as

$$\lambda_D = \left(\frac{\varepsilon_0 T_e}{n_e E} \right)^{1/2} \approx 700 \sqrt{T_e / n_e}, \quad (1.1)$$

where ε_0 is the permittivity of free space, k is Boltzmann's constant, e is the elementary charge, T_e is the electron temperature in eV, and n_e is the electron density. This assumes that the electron energy distribution function is Maxwellian.

Plasma physics literature abounds with theoretical descriptions of sheaths, and much numerical modeling has been done to determine plasma profiles above surfaces. Nitter et al. (1998) demonstrated that there are three possible potential profiles that can form above surfaces in plasma, shown in Fig. 1.5(a). Case C is that of a typical plasma, in which the potential profile monotonically increases above the surface and asymptotes to zero at infinity. Case B results when the surface charges to a more positive potential than the ambient plasma, so that the potential profile monotonically decreases to reach the plasma potential. Finally, a more complex case of non-monotonic potentials can occur when the minimum of the potential lies at some distance above the surface, as in Case A, resulting in distinct populations of electrons. Both Cases A and B can occur above a photoemitting surface in space; which forms will depend on the ambient plasma conditions and the relative strengths of the plasma and photoelectron currents.

Whenever a sheath forms above a surface, a vertical electric field is generated. As dust particles on a surface build up an increasingly negative charge due to collection of electrons, there is a chance that they will become detached from the surface and then transported through the plasma sheath. While the specific mechanisms causing the dust particles to lift off the surface are unclear, it is possible to model the trajectories of these particles based on charging and gravitational

balance equations (Nitter et al., 1994, 1998; Stubbs et al., 2006).

1.2.2 Photoelectron sheaths

A photoelectron sheath forms above a surface when photoemission is the sole or dominant charging process. The photoemitting surface will float to a potential determined by the difference energy of the incoming photons and the photoelectric work function of the surface. In equilibrium, there will be a net positive surface potential, and photoelectrons will be emitted from and will return to the surface, as depicted in Fig. 1.5(b).

Photoelectron sheaths surround UV-illuminated spacecraft and airless natural bodies in space (Whipple, 1981). Immediately above the sunlit lunar surface, for example, the most populous species are the photoelectrons emitted from its dusty surface (Colwell et al., 2007). The photoelectrons largely determine the plasma environment of sunlit instruments on spacecraft and of instrument packages on the dayside lunar surface. As a result, corrections for photoelectron sheath effects are made for field and wave experiments (Cully et al., 2007), electron energy analyzers (Scime et al., 1994; Scudder et al., 2000), and ion energy analyzers (Olsen, 1982; Sojka et al., 1984). Electrons of spacecraft origin are easily observed (Szita et al., 2001) and must be removed from energy spectra in order to obtain the distribution of electrons of geophysical origin.

Sheaths consisting only of electrons emitted from a surface were first considered in the context of thermionic vacuum tubes (Tonks and Langmuir, 1929). Electrons from heated cathodes have a temperature near 0.2 eV that is determined by the cathode temperature. Photoelectrons, in contrast, have an energy spectrum that is typically several electron volts in width, as determined by the photon spectrum and the work function of the surface (Grard, 1973b,a; Feuerbacher et al., 1978). Early theoretical work on the physics of Debye shielding in a noneutral plasma has been well-established for magnetized test particles (Davidson, 1971). More recent work by Kremer et al. (2007) has shown that, even for non-neutral plasmas, the standard equations for Maxwellian electrons in a neutral plasma can be applied to the charging currents to plasma probes.

As in the case of a plasma sheath, a photoelectron sheath generates a vertical electric field

above the surface, which here acts to return electrons to the surface. Because individual dust particles may charge positively due to photoemission, once they detach from the surface they can be levitated in the photoelectron sheath. Additionally, patches on the lunar surface (or any other airless body that is covered with insulating regolith) may differentially charge due to effects of uneven illumination or varied plasma currents. This can lead to horizontal electric fields in addition to the vertical fields, setting up an even more dynamic environment for the motion of charged dust particles.

1.3 Previous relevant work

1.3.1 Theoretical

A significant body of work has used theoretical and numerical modeling to investigate the characteristics of photoelectron sheaths and the interactions between dust and plasma environments. Early work was motivated by observations of large surface potentials on the surfaces of spacecraft (Whipple, 1981). Theories have been developed to model the plasma characteristics near a variety of surfaces, including spherical satellites comparable in radius to the Debye shielding length (Schröder, 1973; Tunaley and Jones, 1973; E. C. Whipple, 1976), and flat surfaces with (Guernsey and Fu, 1970; Fu, 1971) and without (Grard and Tunaley, 1971) a neutralizing plasma present as a boundary condition. Theoretical modeling based on Vlasov-Poisson equations have found sheath potential profiles for spherical spacecraft (Whipple, 1981) and above the Moon modeled as a planar surface (Grard and Tunaley, 1971; Singer and Walker, 1962; Walbridge, 1973). Walbridge (1973); Tunaley and Jones (1973); Grard and Tunaley (1971); Singer and Walker (1962) all present analyses of photoelectron sheath characteristics with relevance to the lunar case.

Typical lunar photoelectron sheath dimensions are tens of centimeters to a few meters above the surface (Walbridge, 1973). Grard and Tunaley (1971) found that, regardless of the energy distribution, the photoelectron layer will have a shielding distance, analogous to the Debye length,

that can be written as

$$\lambda_e = \left(a \frac{\epsilon k T_e}{n_e e^2} \right)^{1/2} \quad (1.2)$$

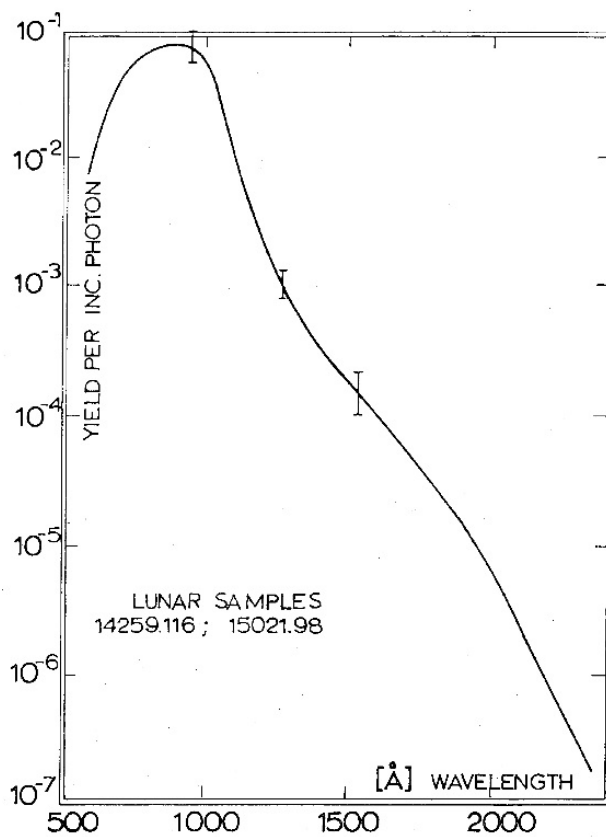
where a is a coefficient near unity that depends on the electron energy distribution function (Grard and Tunaley, 1971). For a photoelectron plasma, we often set $a = 2/3$ (Sickafoose et al., 2001; Grard, 1995; Grard and Tunaley, 1971).

Of additional interest for this research are processes governing charging and motion of dust grains in plasma environments. Many review papers have been published which describe dust grain charging in various astrophysical and planetary environments (Goertz, 1989; Mendis and Rosenberg, 1994; Horanyi, 1996). Early work by Pelizzari and Criswell (1978) and used a numerical model to simulate dust transport at the lunar terminator region, and this was followed up by additional theoretical calculations by Borisov and Mall (2006). Nitter et al. (1998) present specific calculations for the motion of dust particles in a photoelectron sheath above a surface in space. More specifically, Colwell et al. (2007) thoroughly reviews lunar surface dust, plasma charging phenomena, and models of dust lofting and levitation above the surface. Recently, Poppe and Horányi (2010) presented a detailed study combining the effects of the lunar photoelectron sheath and the inflowing solar wind flux and evaluating the role of the resulting plasma environment on dust dynamics. One of the sustained problems throughout many of these models is the difficulty in getting large grains off the lunar surface.

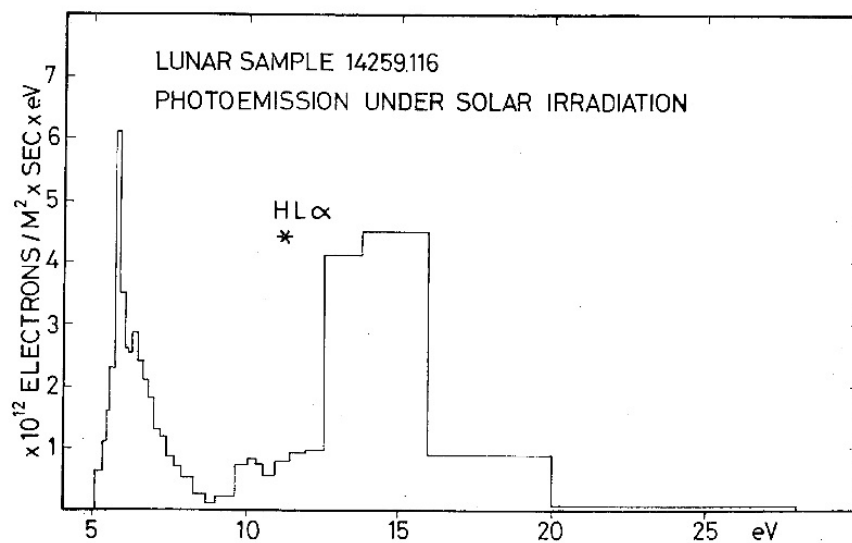
1.3.2 Experimental

In order to make a prediction about the currents due to photoemission from the lunar surface, Willis et al. (1973) measured the photoelectric yield of the lunar surface fines exposed to various wavelengths of ultraviolet light (Fig. 1.6(a)). By convolving this yield function with the known solar illumination spectrum, they modeled the differential photoelectron flux expected from the lunar soil during standard solar illumination conditions, as shown in Fig. 1.6(b).

Some laboratory work has also been done to characterize photoelectron sheaths that are generated above surfaces exposed to UV illumination. Initial experiments conducted by Sickafoose



(a)



(b)

Figure 1.6: (a) Differential photoelectric yield of lunar dust samples as a function of wavelength, (Willis et al., 1973). (b) Modeled differential photoelectron flux from lunar soil as a function of emitted photoelectron energy, determined by convolving the measured yield with the solar spectrum (taken from Hinteregger et al. (1964)).

et al. (2001) were designed to measure charging on dust grains, but also performed some initial characterization of the photoelectron sheath. Photoemission was generated by illuminating a Zr surface with a 1 kW Hg-Xe arc lamp with a quartz envelope, f/1.0 quartz collimating lens, and a rear reflector. Because all of the optical components in this system were made of quartz, although the lamp produced a broad spectrum, a low wavelength (high energy) cutoff of 200 nm (6.2 eV) is set by the quartz transmittance. The photocathode here was a vertically oriented Zr disk, 12.5 cm in diameter, illuminated by the collimated beam with a radius of about 10 cm.

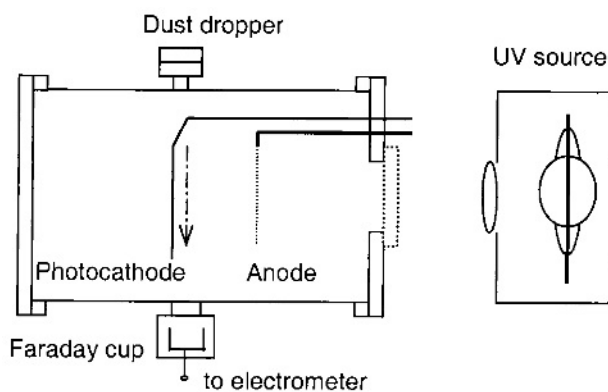


Figure 1.7: Schematic of the experimental setup from Sickafoose et al. (2001). A Zr photocathode is illuminated by a UV source from the right, and the anode is in place to provide a reference bias surface to characterize the photoelectron population.

The photoelectron sheath was characterized using the retarding potential analysis method, such that a 15 cm square of Ni mesh was placed a few cm in front the photocathode, between it and the UV lamps, and biased to -4.5 V to repel electrons from the walls. Then the current on the photocathode was measured as a function of the bias potential. The derivative of the sweeps is related to the electron energy distribution function, $f(z)$ for electron velocities perpendicular to the plate. Fig 1.8(a) shows the measured current as a function of the bias potential. At negative biases, the current is negative due to emission from the probe, and at positive biases it is approximately zero, which indicates that very few electrons are collected. The electron energy function is shown by the points in Fig 1.8(b), and the solid line is a least-squares fit to the data using a κ -distribution with an average electron energy of 1.42 eV. In this setup, the surface produces a typical photoemission

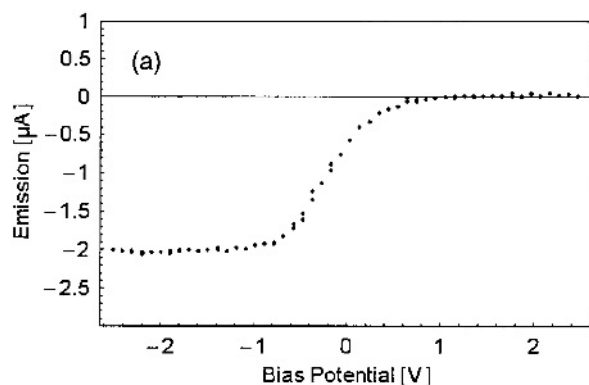
current of about $20 \mu\text{A}$, and a photoelectron density of $2.5 \times 10^4 \text{ cm}^{-3}$, which is doubled when the surface is floating and the emitted electrons return to the surface.

While this sheath was suitable for the desired dust charging experiments, it was limited in that the diameter of the illuminated surface was only about 2.5 times the calculated sheath thickness ($\sim 4 \text{ cm}$). If the photoemitted electrons are modeled as having a Maxwellian energy distribution with a mean energy $\frac{1}{2}kT_e$ given by the measured mean photoelectron energy (1.1 eV), then the sheath profile above the surface will be given by

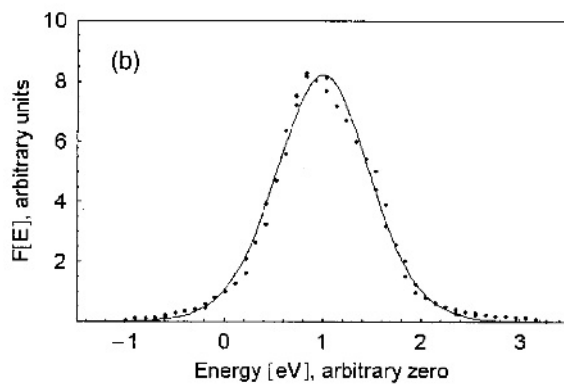
$$n_e(z) = n_0 \left[1 + \frac{z}{\sqrt{2}\lambda_e} \right]^{-2}, \quad (1.3)$$

where n_0 is the electron number density at $z=0$. Because emitted photoelectrons have a high energy cutoff set by the wavelength of the incident light and the surface work function, however, the density probably falls off more quickly than given here.

Studies of probes in a photoelectron environment have been conducted by Wang et al. (2008). In these experiments, a 13x13 cm square of Zr was illuminated by a 1000-W Hg-Xe arc lamp that also had quartz elements, and thus a low-wavelength cutoff of 200 nm (6.2 eV) (the experimental setup is shown in Fig. 1.9). To measure the characteristics of the emitted electron population, a cylindrical Ni wire probe (4.4 cm long, 0.02 cm in diameter) and a spherical stainless steel ball probe (0.3 cm in diameter) were each placed about 1 cm above the Zr surface. The probes had the same surface area so that their sweeps could be directly compared. As expected from probe theory, the two probes measured the same current in the emitting and electron retardation regions (Fig. 1.10(a)), and then begin to deviate in the electron collection region (see Chapter 3 for a detailed description of Langmuir probe measurement techniques). Additionally, the second derivatives of probe characteristics give the electron energy distribution function, $f_E(\epsilon)$, which was approximately the same for the two probes (within 10%), Fig 1.10(b). The biggest limitation of this experiment was that, due to the characteristics of the illumination, the sheath dimensions were small; however, this set of experiments provided a basic demonstration of the use of Langmuir probes in a photoelectron plasma.



(a)



(b)

Figure 1.8: (a) Photoemission current from a Zr cathode as a function of the bias potential, and (b) the derivative of the current (points), from which the electron energy distribution function of electrons moving perpendicular to the plate is determined. The solid line is a least-squares fit to the data using a κ -distribution. From Sickafosse et al. (2001).

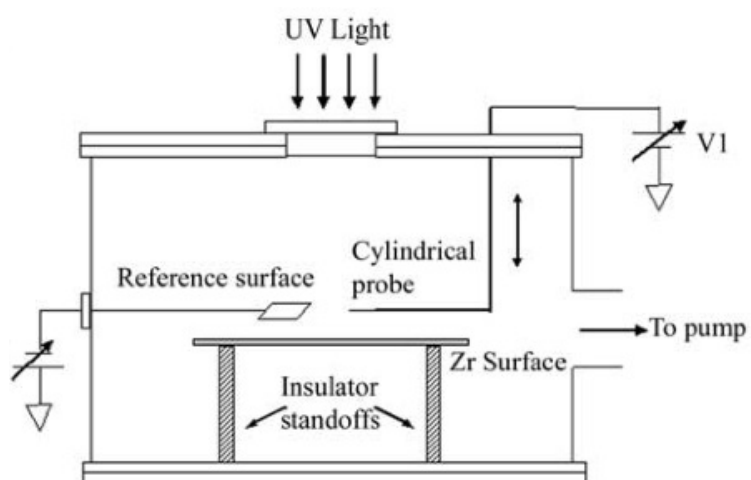
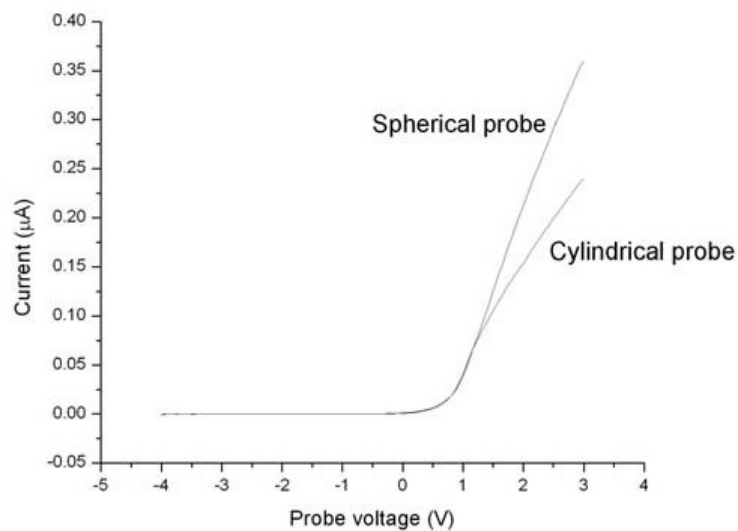
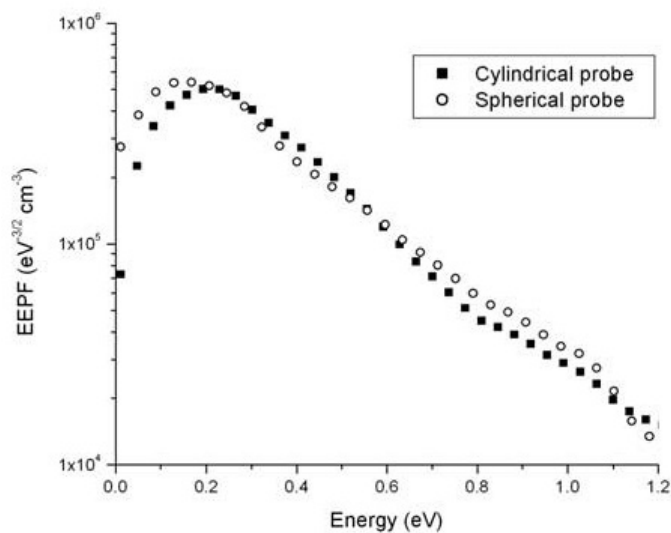


Figure 1.9: Diagram of the experimental apparatus used in Wang et al. (2008) for photoemission studies.



(a)



(b)

Figure 1.10: (a) $I - V$ characteristics of the cylindrical and spherical probes 0.5 cm above a Zr surface, and (b) the electron energy distributions from both probes, derived from the second derivative of the currents. From Wang et al. (2008).

Several sets of experiments have also demonstrated dust charging, lofting, and levitation in plasma environments. In the setup shown in Fig. 1.7, dust dropped in front of the photoemitting surface was observed to charge differently based on its distance from the surface (Fig. 1.11), governed by the balance between photoemission from the dust grain itself and collection of electrons emitted from the Zr surface. Following these experiments, Sickafoose et al. (2002) successfully demonstrated lofting and levitation of dust grains in plasma above a biased, conducting plate. Finally, Wang et al. (2009) observed the horizontal and vertical movement of dust grains that were placed on a conducting, biased surface in a plasma. Measurements of the potential structures above the insulating surfaces showed the presence of a non-monotonic potential structure above the surface that produced an upward- and outward-pointing electric field, causing dust lift-off from the surface.

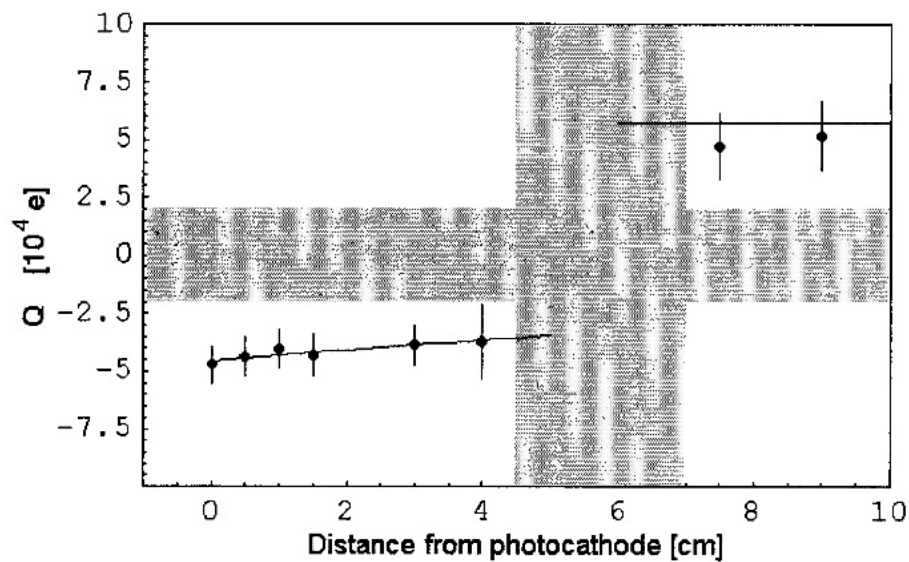


Figure 1.11: Charge measured on Zinc particles as a function of the distance at which they fell in front of the photocathode. The gap in the data indicates the region in which charges were below the detection threshold. The two points farthest from the photocathode lie near the expected charge due to photoemission from the grain itself, and indicate that the grains are falling outside of the strong sheath region. From Sickafoose et al. (2001).

1.4 Thesis motivation and structure

Prior to the Apollo missions, little was known about the lunar dust and plasma environment. Surveyor images first hinted at the occurrence of electrostatic dust lofting above the lunar surface, and much theoretical work has since been done to understand the lunar plasma near-surface environment and related dust dynamics. Experimental work, however, has lagged behind, primarily because the Moon and other airless bodies in space present a challenging environment for laboratory studies. The primary motivation of this thesis is thus

- to design and build a setup to explore the physics of photoelectron sheaths above surfaces in vacuum;
- to utilize this setup to understand probe behavior and measurements above these surfaces; and
- to understand how surface charging conditions change the resulting photoelectron sheath and probe measurements.

By conducting laboratory experiments that probe basic plasma processes, we aim to gain insight into how those processes operate on the lunar surface, and to explore how these laboratory probe techniques can be utilized on the lunar surface. The results from this thesis will thus inform the design of future probes for taking in situ measurements above the surface of the Moon and other planetary bodies, provide insight into the nature of the photoelectron plasma environment above these surfaces, and provide a unique laboratory setup for continued experimentation of lunar plasma and dust phenomena.

In addition to understanding the properties of the lunar near surface environment, a strong research driver is the lunar dust itself. Lunar dust has been recognized as one of the greatest hazards in continued lunar exploration due to its tenacious adhesion to everything with which it comes into contact. Unfortunately, there is little known about the mechanisms of adhesion on widely varying surface types. Surface energy, roughness, mechanical properties and electronic properties are all

known to contribute to the adhesion characteristics. An optimal solution to mitigate dust adhesion would be to identify the dominant components of the adhesive force and to reduce that force by surface modification. Thus, in Chapter 2, we look at the mechanisms that control adhesion of dust to surfaces. We use a centrifugal force detachment technique to measure adhesion forces of grains on surfaces, and complement this with surface property analyses. These experiments are undertaken in order gain greater insight into the relative roles of various forces on adhesion, in an effort to find ways to mitigate the adhesion onto surfaces.

For the remainder of the thesis, I focus on creation and analyses of photoelectron sheaths above surfaces in vacuum and bulk surface charging. These experiments, the diagnostic tools, and the theory behind the analyses are described in Chapter 3 to set the stage for the following chapters. With this background established, Chapter 4 discusses measurements taken above a large, planar Zr surface that is illuminated by UV radiation with a narrow wavelength distribution around a central wavelength of 172 nm. The retarding potential analysis method is used first to measure the characteristics of the electron populations emitted from the Zr surface. Then, measurement are taken throughout the resulting photoelectron sheath using a cylindrical Langmuir probe to measure the plasma potential and the photoelectron properties as a function of height above the surface. These measurements are compared with the results from numerical simulations using a 1-D PIC code to model the experimental setup.

In Chapter 5, complexity is added to this setup by placing insulating materials on the Zr surface. A single-sided planar Langmuir probe is used to measure the currents and the characteristics of the electron populations above these surfaces. Interesting potential structures result from this setup, and inform us about charge balance of photoemitting insulating surfaces, as well as the charging currents that develop between two differently-biased surfaces. These are the first measurements of this kind over insulating surfaces with differential potentials, and are highly relevant to the lunar surface, as well as other bodies in space, where regions of differential charging occur in close proximity.

Finally, I will summarize the results of this study, including how it has advanced our understanding of photoelectron sheath measurements above surfaces in space, and discuss some of the implications for future laboratory and spacecraft studies in Chapter 6.

Chapter 2

Mitigation of dust adhesion to surfaces by surface modification

Adhesion of dusty regolith to spacecraft surfaces is a significant concern to those who are interested in developing robust mechanical and optical systems, as well as systems compatible with extensive human exploration of these dusty surfaces. Here we present research that was undertaken in collaboration with Ball Aerospace and Technology Corporation (BATC), to understand the forces controlling adhesion, and how these forces might be controlled to mitigate adhesion. Ball has developed a contamination mitigation process that reduces the adhesion of molecular and particulate contaminants, such as lunar dust, to a wide range of surfaces. This technique relies upon a surface modification of a substrate and is thus called a “passive” solution, as compared with “active” mitigation methods which rely on the availability of power, disposable materials, or other hardware. This approach can be used for any application which requires contamination control; for example, during fabrication of contamination sensitive products, or in space, where this method can prevent or reduce particulate buildup on sensitive optics in dusty environments.

The remainder of this chapter is constructed as follows. We describe the physical results of this modification on the surface in Section 2.2. Contact charging measurements for electrostatic (image) force calculations are described in Section 2.3. Adhesion experiments with less than 25 μm JSC-1 and Lunar Highlands Type (LHT) simulants, and experiments analyzing the effects of UV irradiation on surface adhesion are shown in Section 2.4. We summarize and discuss these results in Section 2.5.

2.1 Theory and background

Adhesion of dust and powders to surfaces has been an area of study for many years (Zimon, 1969; Mizes et al., 2000). The factors mediating adhesion are extensive; van der Waals forces, electrostatic forces, chemical bonding, capillary forces, oxidation, and magnetic forces, are just a few examples. While some forces are reduced in the lunar environment, others are expected to be much higher due to the charging effects of the solar wind and UV ionization (Abbas et al., 2007). The primary forces responsible for adhesion of dust to surfaces are short-range van der Waals forces and long-range electrostatic forces (Walton, 2007).

Van der Waals forces are driven by the intermolecular or interparticle forces acting between two materials in close contact, combining the effects of interactions between permanent dipoles (Keesom interaction), induced dipoles (Debye induction) and instantaneous induced dipoles (London dispersion force) (Israelachvili, 1985). An equation for the van der Waals force, F_{vdW} , between a smooth spherical particle and a flat surface is (Walton, 2008),

$$F_{vdW} = \frac{AR}{6D^2}, \quad (2.1a)$$

where R is the radius of the sphere, D is the spacing between the sphere and the surface and $D \ll R$. The Hamaker constant, A , can be estimated from surface energy as (Burnham et al., 1990)

$$A = 12\pi D_0^2 \Delta\gamma, \quad (2.1b)$$

where $D_0 \sim 0.2$ nm and $\Delta\gamma = \sqrt{\gamma_p \gamma_s}$, where γ_p and γ_s are the surface energies of the particle and the substrate, respectively. Surface energy is the work required to separate a unit area of two surfaces in contact.

Real particles and surfaces have varying roughness and mechanical properties, both of which affect spacing, and thus the van der Waals force. More sophisticated theoretical approaches combine the effects of particle roughness, Young's modulus, Poisson ratio, surface energy and interfacial surface energy (Li et al., 2006; Derjaguin et al., 1975; Rabinovich et al., 2000). Reasonable agreement

between theories which consider surface roughness and experimental data was achieved using 6 μm smooth spherical alumina particles in contact with surfaces with well defined asperity distributions, ranging from 30 to 240 nm roughness. The adhesive force ranged from 2.4 nN for 30 nm roughness to 1.2 nN for 240 nm roughness (Gotzinger and Peukert, 2004).

Coulombic attraction is the other dominant force in particle adhesion. Surfaces of interest may already possess a charge *before* they come into contact (due to external environmental conditions such as photoemission, controlled charging, etc.), and they will thus be attracted (or repulsed) dependent on the signs and magnitudes of their charges and the surfaces of interest. An example of this is the controlled charging of toner particles in xerography; the toner is charged positively before exposure to the charged drum, thus adhering to areas which have been negatively charged. A slightly different scenario arises when two surfaces with different work functions come in contact; in this case, *during* contact, electrons transfer from the material of lower magnitude work function to the material with higher magnitude work function (Harper, 1967; Sternovsky et al., 2001), resulting in modified charges on the surfaces. Contact electrification measurements between 5 μm polystyrene (PS) spheres and gold or highly oriented pyrolytic graphite surfaces demonstrated that adhesion correlates with the amount of charge transfer (Gady et al., 1998).

For a charged dielectric spherical particle contacting a planar conducting surface, the attractive Coulombic force, namely the image force, is given by

$$F_i = -\alpha \frac{Q^2}{16\pi\epsilon_0 R^2}, \quad (2.2)$$

where Q is the charge uniformly distributed on the particle surface, R is the radius of the particle, ϵ_0 is the permittivity of free space, and α is a correction factor which depends on the polarizability of the dielectric particle. However, the total charged area on a particle whose charge results from contact represents a small portion of the total particles surface area, i.e., the charge is not uniformly distributed on the particle's surface. It is found that the measured image forces on toner particles exceed the predictions from Equation 2.2 by factors of 5 to 50 (Hays, 1995). Based on these discrepancies, Hays (1995) developed a model based on localized charge patches that calculates the

electrostatic force as

$$F_e = \frac{\sigma A_c}{2\epsilon_0}, \quad (2.3)$$

where the charge density $\sigma = Q/A_t$, A_c is the charged area that contacts the surface, and A_t is the total charged area of the surface.

In the last several years, significant effort has been expended to evaluate and mitigate lunar dust adhesion for lunar exploration purposes (Hyatt et al., 2007). Various means of reducing adhesion have been attempted, such as by improving surface conductivity (Agui et al., 2006) or reducing the van der Waals interaction (Peters, 2009). Methods have also been developed for removing adhered dust particles, including mechanical vibration, wiping and brushing, using a noncontacting electromagnetic brush with oscillating EM fields, or using electric fields to remove particles (Clark, 2009; Immer et al., 2006). These methods are still in their infancy and limited quantitative adhesion data is available.

2.2 Surface modification

A proprietary ion beam process was previously developed for mitigation of molecular contamination (Crowder and Haley, 2008). This method is thought to successfully reduce molecular adhesion due to a reduction in surface energy of the substrate material. Further development has been undertaken to enhance and broaden this effect for reduction of particle adhesion to substrates. In this process, precursor gases are supplied into an ion source where a plasma is formed. The positive ions are selectively extracted from the plasma and accelerated out of the ion source, providing an ion beam that is directed at the sample surfaces. No apparent net growth or removal of the materials results from this process. The effectiveness of the process relies upon the choice of precursor gases, gas flow rate, vacuum pressure, ion energy, ion current, distance between the substrate and ion source, and deposition time.

2.2.1 Materials

For these experiments, we use conductive black Kapton (DuPont, P/N 275XC), GE 124 high purity fused quartz (Ted Pella, P/N 26013), and test grade p-type silicon (Wafer World, P/N 1195). Black Kapton was vacuum baked for 24 hours at 100° C. Quartz samples were cleaned with a multistep process as follows: (1) detergent clean using de-ionized water, (2) rinse with de-ionized water, (3) rinse with isopropyl alcohol, (4) rinse with methanol, and (5) dry with nitrogen gas. Silicon wafers were used as received. JSC-1 simulant was sieved to the size fraction desired, and stored in a vacuum bell jar to reduce the risk of contamination and effects of humidity. In between experiments, the particles remaining on the substrate were removed with compressed air, and then the substrate was wiped clean with ethanol.

2.2.2 Contact angles

The surface energy of a solid can be determined by measuring the contact angle, θ , the angle which which a liquid (with known surface energy) meets the solid substrate. An equation relating these parameters is given as

$$\cos(\theta) = -1 + 2\sqrt{\frac{\gamma_{solid}}{\gamma_{liquid}}}e^{-\beta(\gamma_{liquid}-\gamma_{solid})^2}, \quad (2.4)$$

where $\beta = 0.00001247$, and γ_{solid} and γ_{liquid} are the surface energy of the solid and liquid used in the measurements, respectively (Kwok and Neumann, 2000). A goniometer (First Ten Angstroms Model FTA 1000 Drop Shape Instrument) is used to measure contact angles with NanoPure water used as the liquid probe, and both the receding and advancing angle are recorded.

Surface energies of black Kapton, silicon, and quartz are calculated using Eq. 2.4 and listed in Table 2.1. The proprietary treatment process decreases the surface energy of the silicon and quartz substrates by about 60%, while the Kapton shows an approximately 180% increase in surface energy after treatment. These calculations assume that surface morphology is not influencing contact angle.

Table 2.1: Contact angles and corresponding surface energy, γ_{solid} , assuming $\gamma_{liquid} = 72 \text{ mJ/m}^2$.

Surface		Angle ($^\circ$)		γ_{solid} (mJ/m^2)	
Type	Treatment	Mean	Std. Dev.	Mean	$\pm\sigma$
Kapton	Untreated	80.4	2.54	24.8	$\pm_{1.8}^{1.9}$
	Treated	16.4	0.53	69.9	$\pm_{0.2}^{0.2}$
Silicon	Untreated	38.1	2.13	58.1	$\pm_{1.5}^{1.6}$
	Treated	86.8	1.20	20.3	$\pm_{8.0}^{8.0}$
Quartz	Untreated	29.3	1.84	63.8	$\pm_{1.1}^{1.0}$
	Treated	77.3	0.98	27.1	$\pm_{0.7}^{0.8}$

2.2.3 Surface properties

We measure surface roughness on three locations each on a virgin silicon wafer and a virgin black Kapton substrate using optical profilometry (Zygo NewView 5032 Optical Profilometer). The RMS roughness is reported for a 0.14 by 0.11 mm area on each surface with 5 Å resolution. The roughness of virgin silicon was measured to be $\sim 1.5 \text{ nm}$, and that of virgin black Kapton was $\sim 230 \text{ nm}$.

2.3 Contact charging

We experimentally measured the charges on JSC-1 particles due to contact with the virgin and treated surfaces. The experiments were performed in a cylindrical stainless steel vacuum chamber 51 cm in diameter and 28 cm in height that was evacuated to a base pressure of 10^{-6} torr by a turbo-molecular pump (Wang et al., 2007b). We attached the surfaces to a horizontal aluminum plate, with a small central hole in the surface and a larger hole in the plate to allow particles to pass through. The $< 1 \text{ mm}$ diameter of the small hole allows for individual particle drops. Particles were placed on the surface with an attempt to make the inter-particle spacing greater than the particle sizes in order to minimize contact between particles and maximize contact with the surface being tested. Nominally, the particles are uncharged, although no active measures were taken to ensure that all dust particles were discharged before contact with the surface. Thus, the measured charge on a particle is derived from charge exchange between the surface and the particle. A pulse signal

to a solenoid activates an agitator to vibrate the plate, so that particles fall through the central hole down into a Faraday cup. The Faraday cup is attached to an electrometer that calibrates pulse height to the charge of the particle (Wang et al., 2007b). Electrical noise in the circuit sets a lower limit of $\pm 3 \times 10^4 e$ on the charges. Complex signals generated by multiple particles dropping at once are rejected during analysis.

We measured charges on 180 - 212 μm JSC-1 particles in contact with both virgin and treated Black Kapton substrates in vacuum. Histograms of the charge distributions are shown in Fig. 2.1. Each histogram is fitted to a Gaussian distribution, $f(x) = b \cdot \exp[-(x - \mu)^2/2\sigma^2]$, where b is a constant, μ is the mean of the charging data, and σ is the standard deviation. The resulting least-squares Gaussian fits to the data are shown as the solid lines in Fig. 2.1. The measured charges (mean charge \pm standard deviation from the Gaussian fits) are listed in Table 2.2. We find that the charge on particles in contact with the treated surface is about 3 times smaller than the charge on particles in contact with the virgin surface.

Table 2.2: Contact charging measurements of 180 - 212 μm JSC-1 particles on black Kapton in vacuum (at 10^{-6} Torr). Mean and standard deviations are determined by Gaussian fits to the histogrammed data.

Surface	Charge ($\times 10^5 e$)	$\pm \sigma$ ($\times 10^5 e$)
Virgin	-2.34	3.21
Treated	-0.741	0.807

2.4 Adhesion experiments

2.4.1 Experimental setup

A centrifugal force technique was used to measure the adhesive forces between dust particles and the substrates (Salazar-Banda et al., 2007). Dust grains were distributed on the substrates attached to a 2.5 cm diameter roller. The centrifugal force on the particles is determined from the rotation rate as

$$F_c = mR\omega^2, \tag{2.5a}$$

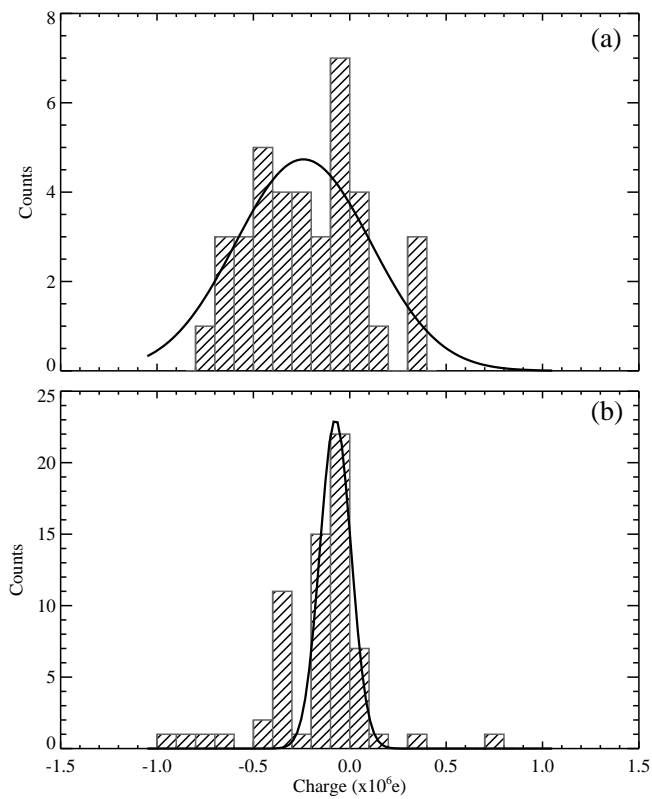


Figure 2.1: Contact charging measurements between 180 and 212 μm JSC-1 lunar simulant particles and (a) virgin and (b) treated black Kapton, in vacuum. Solid lines are Gaussian fits to the histogrammed data. Corresponding means and standard deviations are listed in Table 2.2.

where m is the mass of the particle, R is the radius of the roller, and ω is the angular speed of rotation. Thus, the maximum adhesion force before detachment, F_{ad} is equal to

$$F_{ad} = -(F_c + F_g), \quad (2.5b)$$

where $F_g = mg$ is the gravitational force. Particles detach from the surface when the roller spins above a critical speed such that this combination of forces exceeds the adhesive force on the roller.

Centrifugal force measurements were performed in the same vacuum chamber as the contact charging measurements. An external motor drives a shaft that passes through a vacuum feedthrough into the chamber. Spinning speeds are set by the constraints of the feedthrough to maintain vacuum at a base pressure of 10^{-6} torr. Two gears are employed between the motor driven shaft and the roller shaft within the chamber to triple the spin rate of the roller and achieve greater forces. A video camera is mounted externally to the vacuum chamber, looking through a window perpendicular to the substrates. An external lamp provides optimal surface illumination for imaging.

Dust was distributed evenly on the surface by agitating it through a $63 \mu\text{m}$ sieve until a thin layer covered the substrate. In each trial, we attempted to completely cover the substrate with a monolayer of dust so that the measured forces are those between the surface and the particles. In reality, it is quite difficult to achieve a true monolayer and we will be measuring the effects of inter-particle forces in addition to the particle-surface adhesion forces.

Each sample was spun in increments between 0 - 1500 RPM. At each increment, the roller was spun for about 30 seconds, stopped, and an image was taken of the surface. The lighting was consistent between images in an experiment to avoid changes of the image background. After a clean surface baseline brightness was subtracted from each image, the brightness of each image was normalized to the brightness at 0 RPM. The percentage of remaining dust particles was determined by the total normalized brightness at each rotation rate.

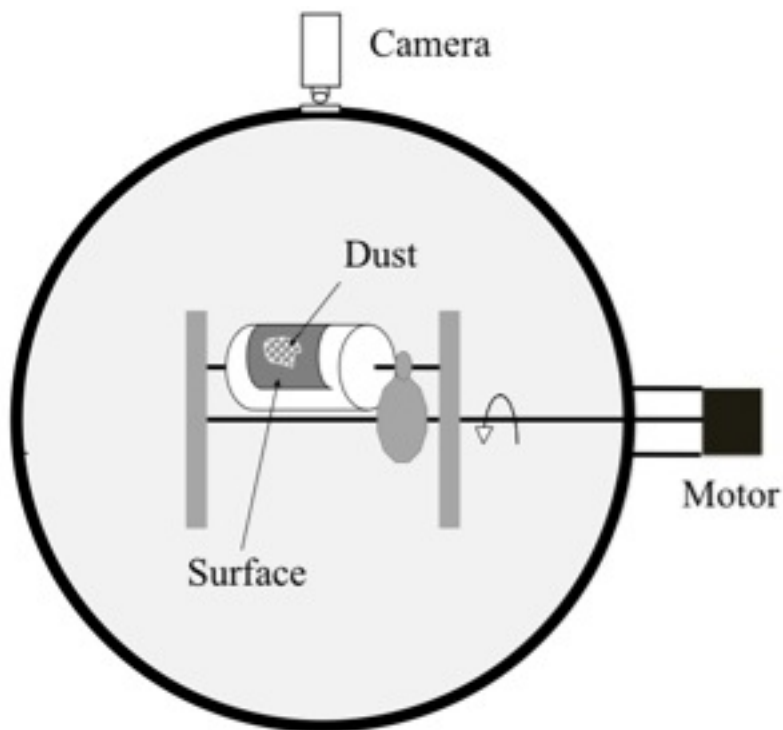


Figure 2.2: Schematic of the experimental setup used for adhesion experiments. The chamber is 51 cm in diameter and 28 cm in height, and the motor is attached through a vacuum feedthrough to drive the gears and the roller. Surfaces are attached to the roller apparatus, and then dust is placed on the surfaces for each experiment. A lamp that provides surface illumination is not shown.

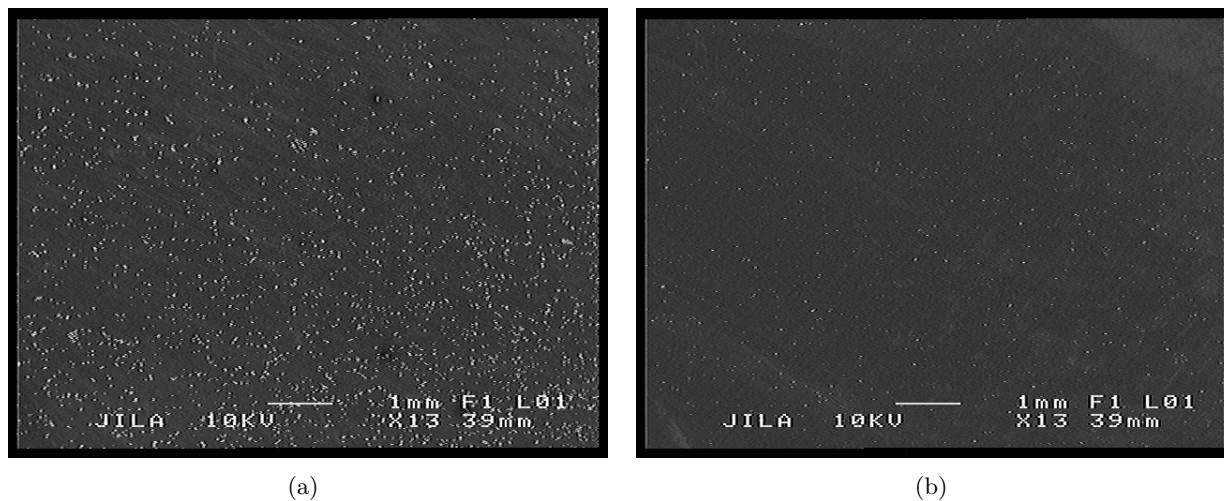


Figure 2.3: Sample SEM images showing dust deposition on black Kapton surfaces (a) pre-spin and (b) post-spin.

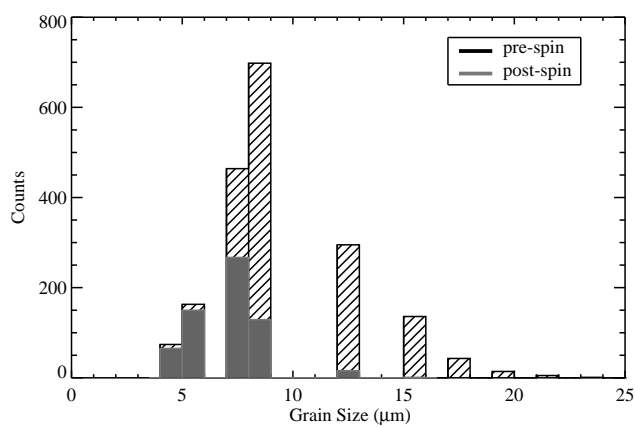


Figure 2.4: Histogram of the distribution of JSC-1 lunar simulant particles on the black Kapton surfaces pre-spin (black hashed) and post-spin (grey solid).

2.4.2 Less than 25 μm JSC-1

Initial experiments were performed on all substrates with $< 25 \mu\text{m}$ JSC-1 grains. Dust was deposited onto the surface as shown in high magnification scanning electron microscope (SEM) images, Fig. 2.3. For the most part, individual grains were deposited on the surface; a relatively small proportion of deposited dust was as part of larger agglomerates. The size distribution of the particles is shown in Fig. 2.4. Each experiment was performed with two valid runs. We plot the percentage of remaining dust as a function of the centrifugal acceleration (in terms of g's) for virgin and treated substrates in Fig. 2.5 for black Kapton, silicon, and quartz. In these figures, the line is a fit to the results, and the plotted data points represent the range of measured values. It is evident that all of the treated surfaces shed dust at lower forces than the virgin surfaces, typically with large differences at lower speeds and greater total shedding. It is important to note that dust is not completely shed in any of the experiments; in each case, the amount of dust shed either slows down or plateaus at higher rotation rates. By analyzing before and after SEM images such as those shown in Fig. 2.3, it is found that the remaining population is predominantly $< 8 \mu\text{m}$ particles, as seen in the distribution in Fig. 2.4. We interpret this as being due to the fact that the forces are never great enough to make these small particles detach from the surface, as the maximum force they feel is about 3×10^{-10} N. This type of phenomenon has been reported in the literature (Mullins et al., 1992). Adhesive forces are calculated at the rotation rate that shed 50% of dust particles and are shown in Table 2.3. The particle size used for these calculation is $8 \mu\text{m}$, a lower limit of the shed particles. The measured adhesive forces are likely underestimated due to the vibration of the spinning roller. Treated silicon and quartz show $\sim 40\%$ and $\sim 24\%$ reductions in adhesive force, respectively, as compared to the virgin surfaces, while treated black Kapton shows a $\sim 64\%$ reduction.

As described previously, the van der Waals force is proportional to the Hamaker constant, which can, in turn, be defined in terms of surface energy, Eq. 2.1a. For silicon and quartz, the surface energies were reduced by 65% and 58%, respectively, after the treatment, which would

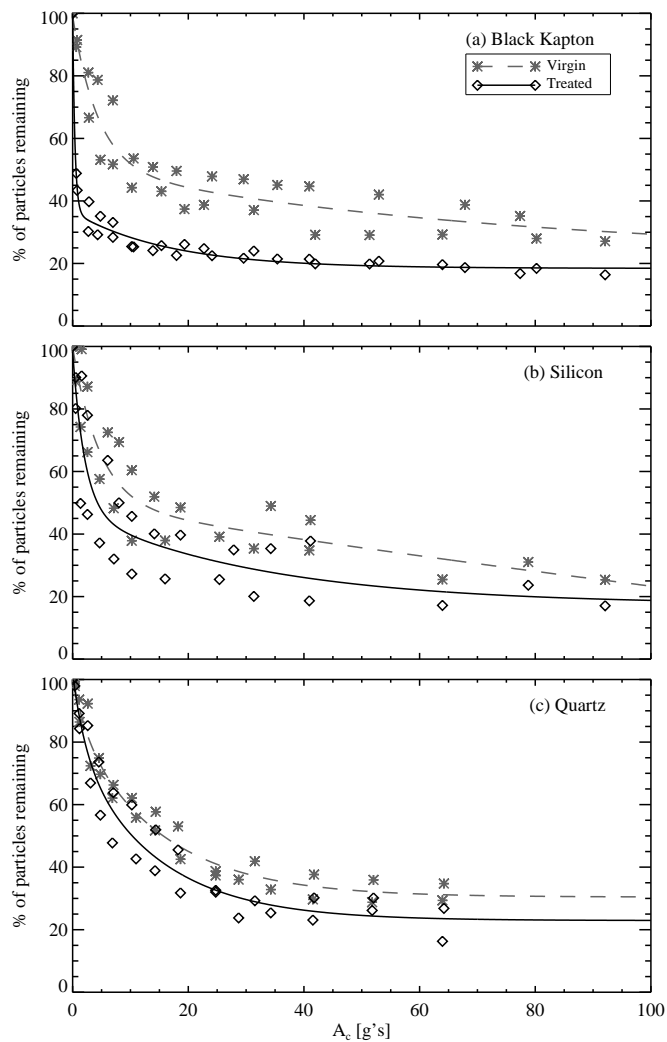


Figure 2.5: Adhesion force experiment results for less than $25 \mu\text{m}$ JSC-1 particles deposited on virgin and treated (a) black Kapton, (b) silicon, and (c) quartz substrates. The solid and dashed lines are fits to the results, while the data points represent the spread in measured values.

Table 2.3: Speeds at which approximately 50% of particles remain on the surface, and the corresponding force on 8 μm particles, calculated from Eq. 5b.

	Speed ($\pm\sigma_{low}^{high}$) (RPM)	Mean $+\sigma_{high}$ (nN)	Mean (nN)	Mean $-\sigma_{low}$ (nN)
Black Kapton				
Virgin	678 (\pm_{185}^{137})	0.13	0.099	0.068
Treated	145 (\pm_1^1)	0.036	0.036	0.036
Silicon				
Virgin	675 (\pm_{193}^{88})	0.12	0.098	0.066
Treated	425 (\pm_{207}^{106})	0.073	0.059	0.040
Quartz				
Virgin	756 (\pm_{49}^{13})	0.17	0.11	0.10
Treated	596 (\pm_{114}^{104})	0.10	0.084	0.066

suggest corresponding decreases in the van der Waals force of 40% and 35%. Conversely, the surface energy of the treated black Kapton surface was increased by 182%, which results in an increase of 68% in the van der Waals force. However, because black Kapton is conductive, there is also an attractive electrostatic (image) force between dust particles and the surface. This force is estimated to decrease by 90% after treatment due to reduced contact charging. Because the magnitude of the electrostatic forces is so much greater, the calculated total adhesive force for black Kapton is thus reduced by 87%. Table 2.4 lists the difference in the van der Waals, electrostatic, and total adhesive forces between the treated and virgin surfaces for all three substrates. The following self-consistent assumptions are made for the calculations:

- (a) Because JSC-1 particles are composed of 50% SiO_2 by weight, we assign the particles the value of surface energy for SiO_2 , 65 mJ/m^2 .
- (b) We assume that the van der Waals force is the dominant factor for adhesion on the insulating quartz and derive a contact distance, $D = 35 \text{ nm}$, which we expect is largely due to the particle surface roughness. This value is much greater than the roughness of silicon (1.5 nm), and much less than the roughness of black Kapton (230 nm), therefore we chose $D = 35 \text{ nm}$ for the quartz and silicon calculations, and $D = 230 \text{ nm}$ for the black Kapton calculations.
- (c) The total charge on an $8 \text{ }\mu\text{m}$ particle is estimated to be $-9.36 \times 10^3 e$ and $-2.96 \times 10^3 e$ for virgin and treated surfaces, respectively, by linearly extrapolating the measured charge shown in Table 2 (Sternovsky et al., 2001).
- (d) The patch charge model, Eq. 2.3, is used for calculating the electrostatic force, and we assume that the charged contact area is 15% of the total surface area.

2.4.3 Less than $25 \text{ }\mu\text{m}$ LHT

While JSC-1 is a suitable simulant for many purposes, it is not representative of the regolith fines over the entire lunar surface. For this reason, we have also analyzed all three surface types

Table 2.4: Difference between the forces on treated and virgin surfaces, where negative and positive signs indicate a decreased or increased force, respectively, on the treated surface.

	Black Kapton	Silicon	Quartz
ΔF_{vdW}	+1.1x10 ⁻¹²	-4.1x10 ⁻¹¹	-3.9x10 ⁻¹¹
ΔF_e	-8.5x10 ⁻¹¹	N/A	N/A
$\Delta F_{ad,calculated}$	-8.4x10 ⁻¹¹	-4.1x10 ⁻¹¹	-3.9x10 ⁻¹¹
$\Delta F_{ad,measured}$	-6.3x10 ⁻¹¹	-3.9x10 ⁻¹¹	-2.6x10 ⁻¹¹

using LHT (Lunar Highlands Type) simulant, ground and sieved to < 25 μm -sized particles. Likely due to the large cohesion force between particles, the LHT was found to clump and created net “larger” particles during our grinding and sieving procedure and during deposition on the surfaces. These “larger” particles are more easily removed from the surfaces than would be the case for the individual particles. It appears that there is very little difference in removal force of the LHT particles from the virgin and treated surfaces, with only the quartz surfaces showing removal at significantly different forces. Because of the uncertain nature of the particle populations, we will not comment more on this simulant here.

2.4.4 UV-irradiated substrates

Surfaces in space will be exposed to solar radiation, including highly energetic ultraviolet photons. Thus, we have exposed all of the substrates to UV-light to understand what effect this radiation might have on the surfaces and on the effectiveness of dust adhesion mitigation. Dust-free surfaces are placed in the center of the vacuum chamber and are exposed to UV light for 2 hours. The UV light is generated by a 1kW Xe-Hg arc lamp, which has a wavelength cutoff at 200 nm. In Fig. 2.6, the performance of the virgin and treated substrates (control) are compared to the performance of the same surfaces after they have been exposed to strong UV light. The virgin black Kapton surfaces shed dust at similar speeds. On the other hand, the treated black Kapton surface is likely to benefit from the UV-irradiation, shedding particles at lower forces, and also shedding a greater overall percentage of particles. The silicon surfaces show less affect, with only slightly increased forces required to shed the dust. Both virgin and treated quartz surfaces are

most affected by the UV-irradiation, showing dramatically increased adhesion.

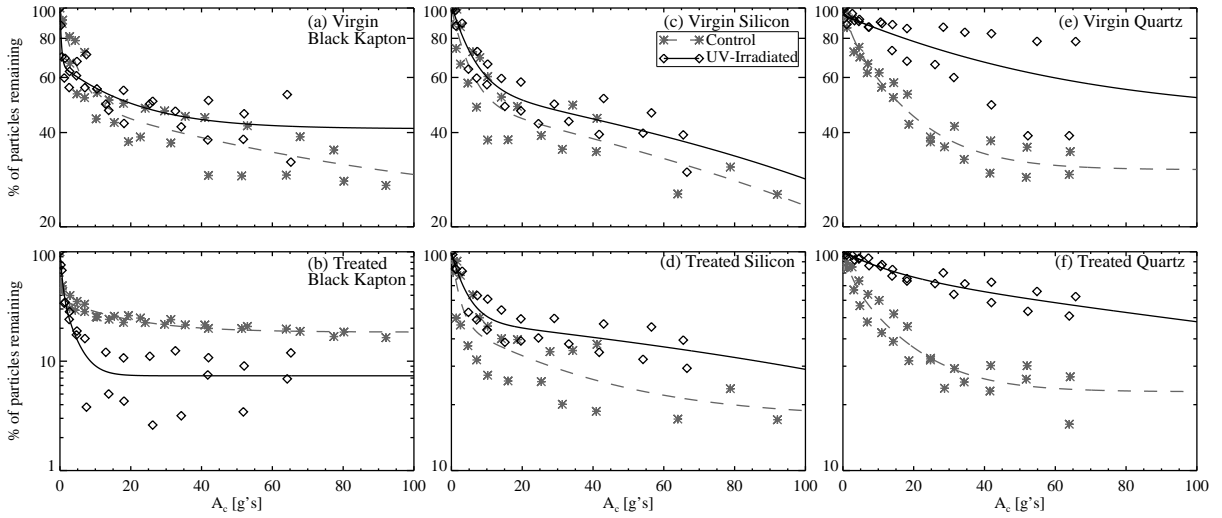


Figure 2.6: Adhesion force experiment results for less than $25 \mu\text{m}$ JSC-1 particles deposited on both control and UV-irradiated virgin and treated black Kapton, silicon, and quartz substrates. The solid and dashed lines are fits to the results, while the data points represent the spread in measured values.

2.5 Discussion of adhesion results

Black Kapton, silicon, and quartz substrates have been modified (treated) by ion beam bombardment. Adhesion between lunar simulants and the virgin/treated surfaces has been measured in vacuum, and results indicate that all treated surfaces exhibit significantly reduced adhesion. We have analyzed the surface energy of all substrates, and observe that it is reduced for silicon and quartz after treatment, contributing to a reduction in the van der Waals forces. Treatment increases the surface energy, and thus the van der Waals force, of black Kapton; however, the electrostatic (image) force decreases due to the reduced contact charging more than the increase in the van der Waals force. Thus, there is a net decrease in total adhesive force for treated black Kapton. Substrates have also been exposed to UV radiation and then dusted for adhesion measurements. Both virgin and treated quartz surfaces are most affected by the UV-irradiation, showing significantly

increased adhesion.

We have only considered the effect of van der Waals forces on the adhesion of lunar simulant to silicon and quartz substrates here, and electrostatic image forces were also considered for adhesion to black Kapton. However, additional forces arise on insulating and semiconducting surfaces. For instance, charge transfer between the insulating lunar simulant and the insulating quartz can create an attractive Coulombic force. Forces on the silicon surfaces can be even more complicated due to the limited conductivity, but, while they could affect dust adhesion, these forces are still not well-understood.

Additionally, physical characteristics of the surface play an important role in adhesion because they determine the area of interaction and distance between the surface of a particle and that of a substrate. Changes in surface roughness will increase or decrease the van der Waals forces, as described above, and can also affect the electrostatic forces by changing the area of the particle that comes in contact with the substrate. This latter effect will also arise due to changes in the hardness of a surface, especially for highly deformable surfaces, such as black Kapton. The surface roughness of silicon is more than an order of magnitude smaller than the estimated surface roughness of the JSC-1 particles, so that changes in roughness after treatment would likely have a negligible effect on the adhesion forces. On the other hand, the surface roughness of black Kapton is large enough to reduce the van der Waals force to be significantly smaller than the electrostatic (image) force. In this case, a small change in surface roughness due to modification would also have a negligible effect on the adhesion forces. Surface hardness is not well-characterized in our experiments and merits further investigation.

A large fraction lunar regolith is composed of micron- and submicron-sized fine dust particles that are produced by meteor impacts onto the lunar surface. The angular and therefore abrasive nature of lunar dust has been recognized as a hazard to spacesuits and equipments; it was found to adhere tenaciously to space suits and other materials during the Apollo missions (Gaier, 2005b). Dust adhered on instruments may damage mechanical components, clog sensors, and degrade performance of the optical components. It can also affect thermal optical properties such as

absorptance and emittance and thus influence thermal radiation of instruments to space, possibly leading to dangerous increases in temperature (Gaier, 2009b). In these experiments, we have used a broad range of analyses to identify the effects that van der Waals and electrostatic forces have on adhesion of lunar simulant to varied surfaces. This study has provided insight into a complex problem, and further work with these techniques and the results of this study are being used to work toward a solution for passive mitigation of lunar dust adhesion.

Chapter 3

Experimental apparatus and data analysis

In the following chapters, the results from a variety of UV photoemission experiments are presented. The framework behind those experiments is discussed here. First we provide a description of the experimental apparatus, then discuss the theory behind the probe analysis and how it has been applied in this case, and finally, the diagnoses that have been used to characterize the photoelectron environment in the chamber prior to subsequent experiments.

3.1 Description of the apparatus

Experiments are conducted in a stainless steel cylindrical chamber, the main body of which measures 82-cm high, with a 6-cm internal diameter (Fig. 3.1). The operational area in which measurements are made inside the chamber is typically smaller than this full height, as described below. Numerous ports are available for the addition of diagnostic tools. These ports are arranged radially around the chamber at different heights, and are used for both mechanical and electrical feedthroughs. For most experiments the chamber is pumped down to a base pressure on the order of 10^{-6} Torr with a roughing pump and a turbomolecular pump.

OSRAM Xeradex xenon-excimer lamps (OSR, 2009) are used to produce ultraviolet radiation inside the chamber. Pulsed discharge inside the lamps produces short-lived xenon excimer molecules that quickly dissociate, emitting radiation centered at 172 nm (7.21 eV). The peak of the radiation distribution has a FWHM of 14 nm; approximately 99% of the radiation is emitted in the UV, with only a small percentage in the visible and infrared portions of the spectrum. Because they do not

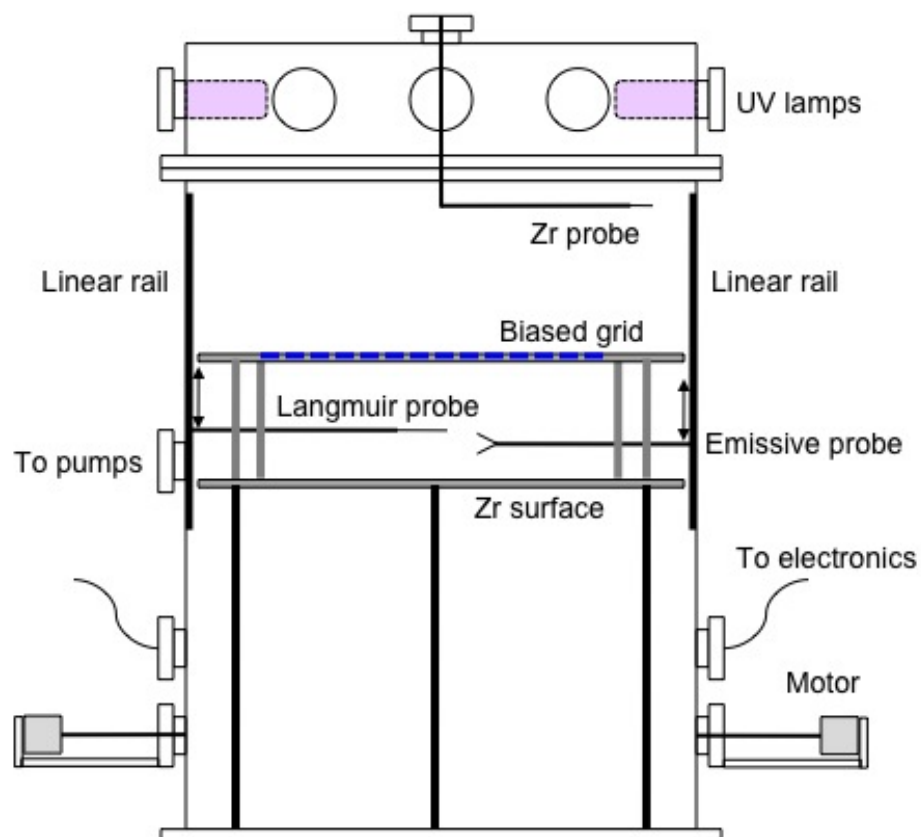


Figure 3.1: Diagram of the chamber. Diagnostic tools and the associated mechanical equipment that were developed for this thesis are labeled.

create a significant amount of heating, it is possible to place these lamps inside the chamber, which creates a significant advantage in terms of utilizing all of the emitted light (since it does not have to pass through a window that sets a wavelength cutoff determined by the window material). Except where noted otherwise, the experiments described herein utilize four of these lamps, equally spaced around the chamber, placed in ports that are located a few inches from the top of the chamber.

A table on which we can place surfaces of interest for the photoelectron studies is constructed from a 20-inch diameter, 1/8-inch thick aluminum sheet. The table top is mounted on 18-inch long, 3/4-inch diameter aluminum rods that sit in nylon caps to insulate the table from the rest of the chamber. The height of the table is determined so that the surfaces will be at the level of several ports around the outside of the chamber and to ensure the surfaces receive a significant flux of photons from the UV lamps above. For most of the experiments presented in this work, sheets of Zr foil cover the surface of the Al table; this is frequently referred to as the Zr surface. An additional grid that is placed above the table is described below.

Several types of Langmuir probes and an emissive probe were built to take measurements in the volume above the surfaces. This setup is designed to allow vertical movement of the probes inside the chamber (perpendicular to the surfaces). KERK linear motion rails (www.haydonkerk.com) are mounted on aluminum supports and placed on opposite sides of the interior of the chamber (Fig. 3.1). The rails allow 20" of vertical travel. They are each controlled by an externally mounted motor that is attached to a linear feedthrough, and then connected to the rail via a flexible shaft. Probes can be mounted to each rail and independently controlled to provide simultaneous measurements, with input/output from the probes controlled by connections through electrical feedthroughs on separate flanges.

A significant portion of this work utilizes a cylindrical wire Langmuir probe that is mounted on the rails in order to take measurements throughout the vertical extent of the plasma. A single-sided planar Langmuir probe was also constructed on a linear feedthrough so that it can be moved horizontally above (parallel to) the surface and measure radial variations; this probe was also modified to be used on the vertical rails. Additional probes were built for specific diagnostics. A

1-inch square Zr flag probe is inserted into the chamber through a flange on the top of the chamber. The probe is moved manually over a vertical range of about 18-inches, and can be rotated 180° within the chamber. Some measurements are taken with a 2-inch spherical copper probe that is coated with colloidal graphite in order to reduce emission from the probe (graphite has a higher work function and has been shown to reduce photoemission (Wang et al., 2008)).

Finally, a washer and grid are placed above the table (shown in Fig. 3.1) in order to reduce the population of electrons from the interior surfaces of the chamber that enter the measurement volume, and to provide an equipotential reference surface for measurements (the reasons and effectiveness of this technique are described below). Several versions of the grid were constructed in an effort to optimize the effectiveness of the setup. For most of the experiments presented here, a stainless steel washer with an outer diameter of 58 cm and an inner diameter of 28 cm supports a circular nickel wire mesh grid which has $\sim 74\%$ transmission. Nickel mesh was chosen because it has a relatively low photoelectric yield and a higher work function than the Zr surface. The grid is attached to an external BNC connector so it can be biased to desired voltages by a power supply. In order to isolate the grid from the table, the washer is connected to ceramic standoffs whose sizes can be changed to vary the height of the grid above the table. In this way, the grid can be placed at an optimal distance to reduce excess electrons but allow measurement of a large volume of the photoelectron sheath that forms above the surface. Additionally, a sheet of copper can be suspended in the space above the grid and attached to an external power supply. This “collector” can be biased to positive voltages to draw electrons from the grid up and away from the experimental volume.

3.2 Langmuir probe operation and theory

Langmuir probes operate by placing a small collector in a low-temperature plasma and measuring the net current while sweeping the voltage on the probe. Ideally the size of the probe will be such that it creates a minimal disturbance of the plasma. By assuming Maxwell-Boltzmann distributions, one can determine the plasma electron density, n_e and temperature, T_e , as well as

the floating potential of the probe, V_{fl} , and the local plasma potential, V_{pl} . Some of these quantities can be determined for non-Maxwellian plasma populations, but the theory is less well-established. Langmuir probes offer the distinct advantage over many other plasma measurement techniques in that they provide local measurements, as opposed to averaging over a large volume of plasma, as is done in spectroscopy or microwave propagation measurements. In this section we will describe the basic operation of a Langmuir probe, how the plasma quantities are determined, and the considerations that must be taken into account for pure electron plasmas.

3.2.1 Characteristic Langmuir probe traces

Figure 3.2 illustrates the basic features of a Langmuir probe characteristic current-voltage ($I - V$) curve, divided into three distinct regions, which are each used to glean information about the plasma characteristics (note that this version of the $I - V$ curve is given for a plasma with only electron populations). In order to obtain such a curve, a bias voltage, V_b , is applied to a probe immersed in plasma, and the bias is swept from negative to positive voltages. At bias voltages more positive than the local plasma potential, $V_b > V_{pl}$, the probe collects electrons; this is called the electron saturation region. At bias voltages more negative than the local plasma potential, $V_b < V_{pl}$, in a typical plasma the probe will collect ions, and this region is called the ion saturation region. In a photoelectron plasma, there is no ion collection current; however, if the probe itself is photoemitting, the resulting current will appear as an ion collection current in this region. In this work, we will typically refer to this as the photoemission current, an example of which is shown in the inset in Fig. 3.2. The floating potential, V_{fl} , is where the currents balance and the net current equals zero, and the region in between V_{fl} and V_{pl} is referred to as the electron retardation region.

For most Langmuir probe sweeps, the floating potential, V_{fl} , is easily determined. In a typical plasma, the floating potential is the value at which the ion and electron currents balance so that there is no net current to the probe. For a pure electron plasma, it is not possible to determine this value since there will not be an ion current, and the $I - V$ curve will not cross at $I = 0$

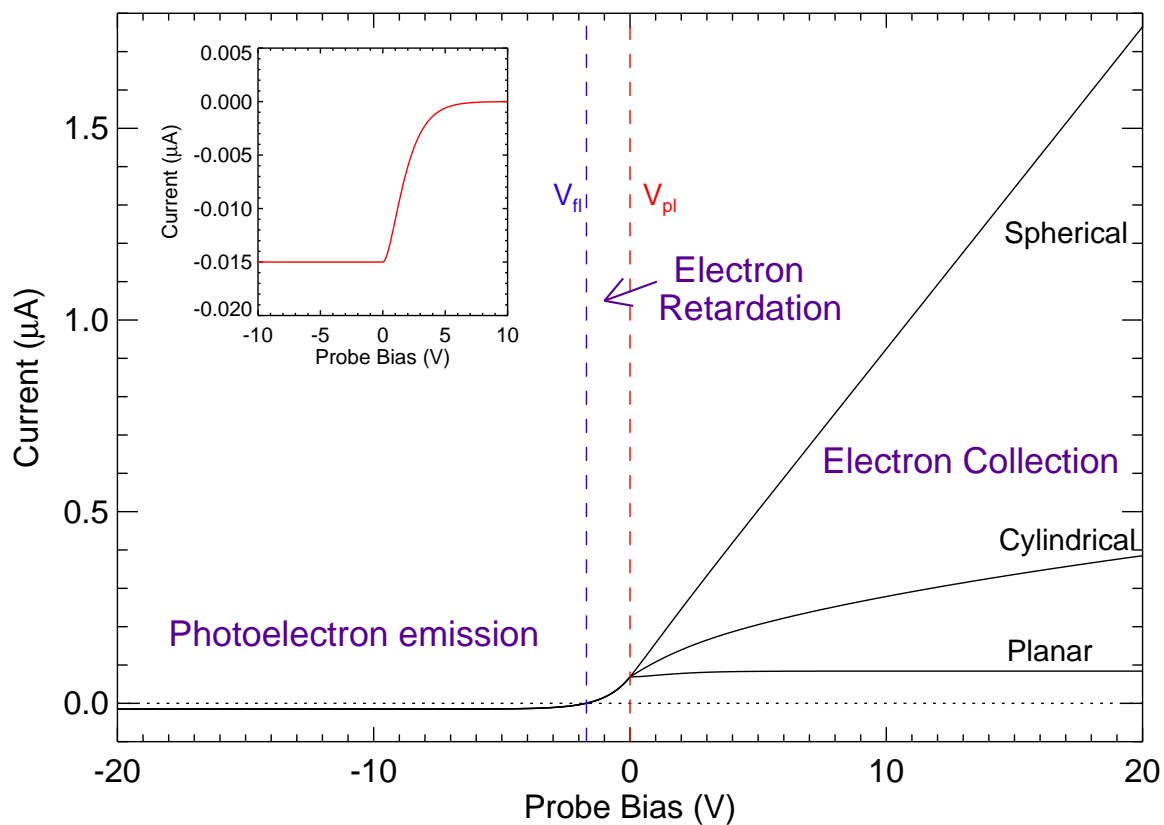


Figure 3.2: Sample ideal langmuir probe curve, with the three regions of interest (photoelectron emission, electron retardation, and electron collection regions) and the floating, V_{fl} , and plasma, V_{pl} potentials labeled. To the right of the plasma potential, the curve splits into three curves, representing the ideal curves measured with a planar, cylindrical, or spherical probe. The inset is zoomed in on only the photoelectron current that is emitted from the probe.

(Kremer et al., 2007). For a photoemitting probe, however, the floating potential is determined by the balance between the emission and collection currents that yields no net current to the probe. Typically, the floating potential is more negative than the actual plasma potential. Due to the high electron thermal speeds the probe tends to draw a higher electron current than ion current, and so the probe floats to a potential more negative than the plasma potential to retard further collection of electrons and enhance ion collection, setting the balance (Merlino, 2007).

Of more interest, but less easily determined, is the local plasma potential, V_{pl} . At V_{pl} , the probe potential equals the local plasma potential, and there is no electric field around the probe, so electrons impact the probe at their thermal velocities. In an ideal probe sweep, the plasma potential is easily identified as the “knee” in the curve, where there is a clear change in slope. In Fig. 3.2, this is most easily identified in the planar probe sweep, and becomes less obvious for the cylindrical and spherical probes. However, in reality this quantity is often affected by noise and probe effects that result in a rounding of the curve so that the knee is less easily determined. Several techniques have been developed to determine the plasma potential in these cases. For instance, by fitting a straight line to the electron saturation region and to the transition region, the plasma potential is determined by the value where these two lines intersect.

In a typical plasma, when the bias potential on the probe is very negative, almost all of the electrons are repelled and ions are collected, resulting in a ion sheath around the probe and an ion collection current. In the absence of ions, there would be no net current in this region. However, in the presence of a UV source, the probe photoemits. In previous work with Langmuir probes in UV, Wang et al. (2008) found that the photoemission current can actually be significant enough to influence the $I - V$ sweep characteristics. As seen in Fig. 3.3, a graphite coating significantly reduced the photoemission current from the probe. If this current is small it can be treated as an apparent ion collection term, which must be subtracted out from the rest of the signal before proceeding with the analysis of the plasma electrons.

The transition region begins when the probe bias is still slightly more negative than the plasma potential, and in a plasma with Maxwellian electrons, the transition region provides some

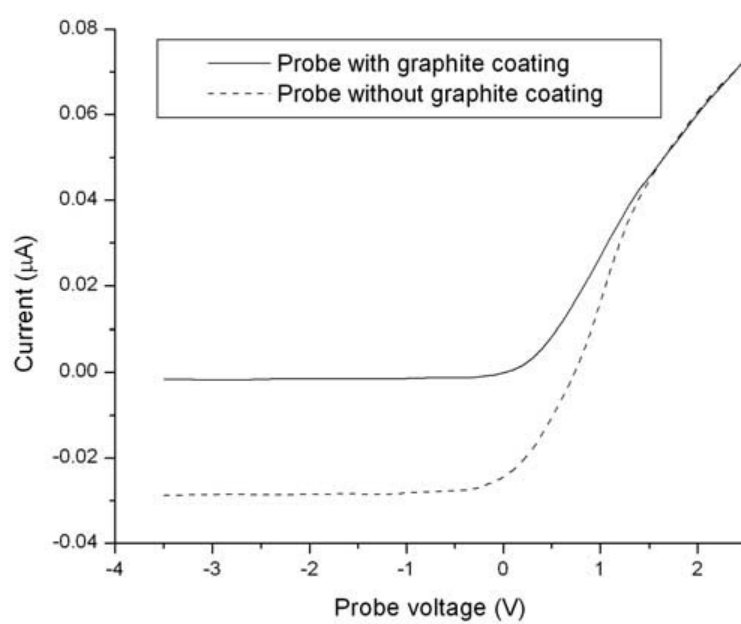


Figure 3.3: Currents measured on a Ni wire cylindrical Langmuir probe without and with a graphite coating, from Wang et al. (2008).

of the most pertinent information about the local plasma. Once the ion or electron emission currents have been subtracted, this portion of the curve is exponential; thus it is relatively straightforward to determine the electron temperature, T_e , as discussed in the following section.

When the probe is biased positively with respect to the plasma, plasma electrons are accelerated toward the probe. In a neutral plasma, ions are repelled from the probe, and in the case of photoemission, any electrons emitted from the probe are returned. This builds up an excess of negative charge, forming a very thin sheath around the probe. Electrons enter the sheath and hit the probe due to their random thermal motions, building up the saturation electron current. The value of the local plasma electron density, n_e , can be determined from this portion of the Langmuir probe sweep. In general, the ion and electron collection currents will be very different, not only due to the mass, but also because the electrons tend to be hotter than the ions, and sheath formation differs between these hot and cold species. Additional effects, such as collisions or magnetic fields, will not be considered here, but can have a significant impact on all aspects of the Langmuir probe $I - V$ curve.

3.2.2 Probe current equations

When calculating the electron currents to a probe, the assumption is made that the relationship between the plasma and probe falls into either the thin- or thick-sheath approximation. In this case, the “sheath” refers to the sheath, with characteristic dimension, d , that will form around the probe, with radius a . The thin sheath approximation is used when the sheath dimensions are small compared to the probe dimensions, such that current is space-charge limited and all particles entering the radius d reach the probe. For a 1D Maxwellian population of electrons, the distribution function is

$$f(x, v, t) = n_e \left(\frac{m_e}{2\pi T_e} \right)^{1/2} \exp \left[-\frac{m_e v^2}{2T_e} \right]. \quad (3.1)$$

Knowing the distribution function, the current is then determined by $j = e \int f(v) v dv$. Thus, the current to the probe, I_e , as a function of the probe bias, V_b is

$$\begin{aligned} I_e(V_b) &= I_e^* \exp\left[\frac{-e(V_{pl}-V_b)}{T_e}\right] && \text{for } V_b \leq V_{pl} \\ &= I_e^* && \text{for } V_b > V_{pl} \end{aligned} \quad (3.2)$$

where the electron saturation current, $I_e^* = S n_e e \sqrt{T_e/2\pi m_e}$, n_e is the plasma electron density and S is the collection (probe) area. For the case when $V_b > V_{pl}$, the electron current is not a function of the probe voltage - this constant value is the electron saturation current.

The thick sheath approximation is used when the probe dimensions are small compared to the sheath dimensions. In this case, the orbit-motion limited theory is applied. For these equations, there is a new quantity, the impact parameter, p , which is the radius at which all entering particles will be collected. The impact parameter is determined by the initial and final energy and angular momentum equations,

$$\frac{1}{2} m v_0^2 = \frac{1}{2} m v_a^2 + q V_a \quad (3.3a)$$

$$p v_0 = a v_a, \quad (3.3b)$$

where v_0 is the initial speed of the electrons and v_a is the speed of the electrons at radius a . Thus, for attractive potentials ($-qV < 0$), when $-qV_0 \equiv \frac{1}{2} m v_0^2$, and the radius of closest approach is the probe radius, a , all particles are collected when the impact parameter is

$$p = a \left(1 + \frac{V_a}{V_0}\right)^{1/2} \quad (3.4)$$

For these cases, the currents to cylindrical or spherical probes are given by:

$$\text{Cylindrical : } I = 2\pi a l j \left[1 + \frac{(V_b - V_{pl})}{V_0}\right]^{1/2} \quad (3.5)$$

$$\text{Spherical : } I = 4\pi a^2 j \left[1 + \frac{(V_b - V_{pl})}{V_0}\right] \quad (3.6)$$

Previous work in pure-electron plasmas has shown that for a Maxwellian electron population, the collected current equation is that same as that shown above (Kremer et al., 2007).

Even if the electron distribution function is previously unknown, it is possible to use the Langmuir probe data to determine the electron distribution function (Hershkovitz, 1989). For a large planar probe, the current and its derivatives are proportional the electron energy distribution function, $f(\epsilon)$, as

$$I_e = I_e^* \exp \left[\frac{-e(V_{pl} - V_b)}{T_e} \right] \propto f(\epsilon) \quad (3.7)$$

$$\frac{\partial I_e}{\partial V_b} = \frac{eI_e^*}{T_e} \exp \left[\frac{-e(V_P - V_B)}{T_e} \right] = \frac{ef_z(v_z)}{T_e} \propto f(\epsilon) \quad (3.8)$$

and

$$\frac{\partial^2 I_e}{\partial V_b^2} = \frac{e^2 f_z(v_z)}{T_e^2} \propto f(\epsilon) \quad (3.9)$$

Even for non-semi-infinite planar probes, the second derivative of the Langmuir probe current sweep is proportional to $f(\epsilon)$ and the energy distribution function by

$$\begin{aligned} \frac{\partial^2 I_e}{\partial V_b^2} &= \frac{2\pi e^3 S}{m_e^2} f(\epsilon) \Big|_{\epsilon=e(V_{pl}-V_b)} \\ &= \frac{1}{4} S e^2 \left(\frac{2e}{m_e(V_{pl} - V_b)} \right)^{1/2} f_E(\epsilon) \Big|_{\epsilon=e(V_{pl}-V_b)} \end{aligned} \quad (3.10)$$

However, $f(\epsilon)$ or $f_E(\epsilon)$ cannot be converted to $f(v)$ unless the plasma potential V_{pl} is known (Hershkovitz, 1989).

3.2.3 Langmuir probe analysis

Probe sweeps are obtained with a LabView program that controls both the input to (bias voltage) and output from (current) the probe. This $I - V$ curve is then analyzed with an IDL program that automatically produces the derived variables described below. Because some signals are weak, they are strongly affected by noise and portions of the analysis are done manually.

First, the floating potential is determined to be where $I = 0$, and the probe photoemission current is subtracted from the total current, so that the new current represents only the electron collection current. This method is valid as long as the photoemission current is small. Next, the plasma potential is determined by finding the peak in the first derivative (Hershkovitz, 1989); it is this step that is most affected by noise, such that the peak is often found by eye. Once the plasma

potential is determined, the current is shifted to place the plasma potential at 0 V. This simplifies the calculation of the electron temperature, so that the slope of the transition region is determined by $\exp(V_b/T_e)$, instead of $\exp[(V_b - V_{pl})/T_e]$. In order to determine the electron temperature, we then take the natural log of I in a small region near the plasma potential. This linear portion is fit to find the slope of the line, and then T_e is determined by the inverse of the slope.

The thermal velocity of the electrons is calculated by $v_e = \sqrt{eT_e/2\pi m_e}$. In the next step, this velocity and the "saturation electron current" are used to determine the electron density, n_e . Because of the imperfection of real probe measurements, as mentioned above, the measured electron current does not level off, even for the planar probe. Thus, we use a standard value of the current at the plasma potential for these calculations, and the density is determined by $n_e = I_e^*/eA_p v_e$, where I_e^* is the electron current and A_p is the probe area. Finally, n_e is used to calculate the Debye length in the photoelectron sheath, $\lambda_e = \sqrt{2\varepsilon_0 T_e/3n_e e^2}$ (Sickafoose et al., 2001).

3.3 Characterizing the electron populations in the chamber

In order to characterize the UV emission from the UV lamps, we use the Zr flag probe in several configurations. Initial measurements are done with a single UV lamp oriented vertically in the center of the chamber, and measurements are then taken radially outward from the lamp. Additional measurements are done with two lamps oriented horizontally, 180° apart in the chamber to determine the variation of UV radiation with distance from the both lamps. Finally, we measured the variation of UV radiation with height directly under the lamps and 90° off axis.

Because of the large collecting area of the Zr surface (area = 1275 cm^2), we have used it for initial measurements of the photoelectron emission within the chamber. We can use these measurements to characterize the photoelectron sheath that forms just above the Zr surface. Additionally, we use this data to determine the levels of emission from the Zr table itself compared to the surrounding walls of the chamber. The table can be used as a Langmuir probe by attaching it to a circuit that sweeps through voltages applied to the table and measures the resulting current at each voltage. We can also use a high-impedance circuit to measure the floating potential of the

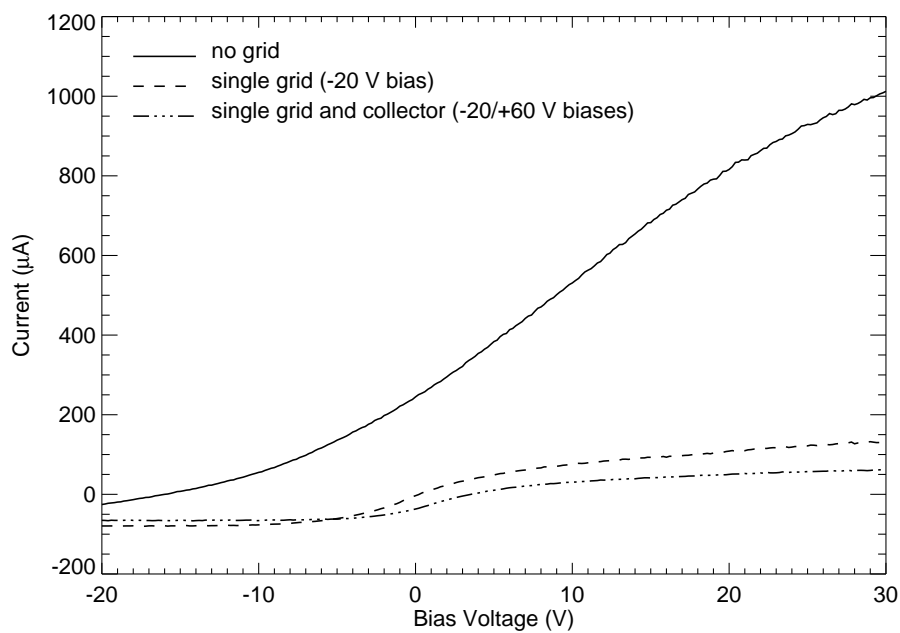
table. When the biased grid is above the table, the table-grid combination acts as a large retarding-potential analyzer with which we can determine if the surface floats positively or negatively with respect to the grid.

3.3.1 Diagnostics with the Zr table

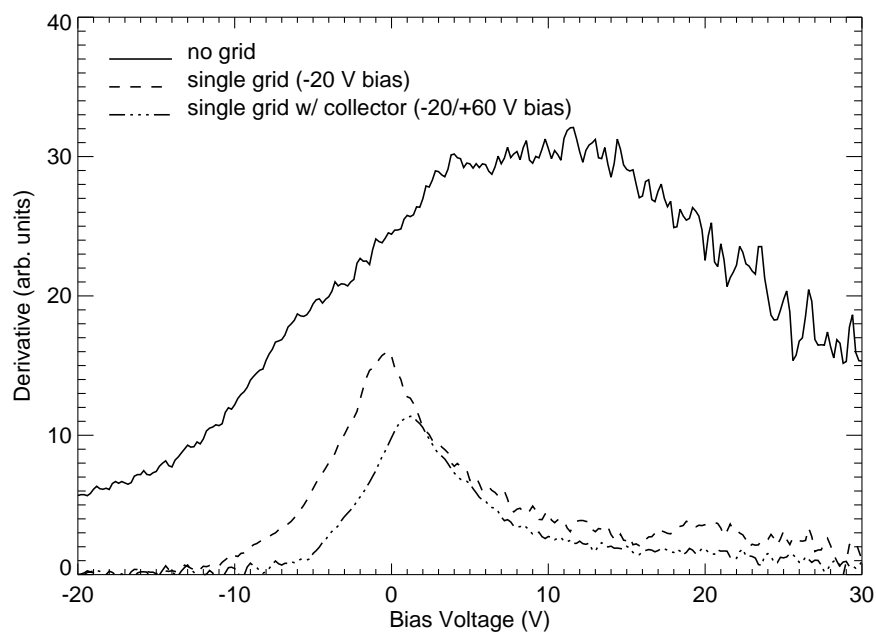
3.3.1.1 Retarding potential analysis

To determine the relative levels of emission of the Zr table and the chamber walls, we have taken Langmuir probe sweeps and high-impedance circuit measurements using the Zr table itself as a probe. Initial measurements (taken without a grid in place above the surface) indicated that these sweep were significantly affected by the collection of wall electrons from the chamber, with the current from these electrons far exceeding that due to emission from the Zr table. This is readily seen in Fig. 3.4(a). When the voltage on the table is very negative, we measure the emission current from the table because the large negative bias accelerates all of the emitted electrons away from the table while at the same time repelling all of the excess electrons from the rest of the chamber. As seen in Fig. 3.4(a), the emission current from the Zr surface is about two orders of magnitude less than the collection current (the current when $V_b > V_{pl}$) of electrons produced in the rest of the chamber volume. One apparent downside of utilizing the grid in this setup is that it reduces the flux of UV radiation to the surface; however, this grid optimizes the amount of incident light and the effectiveness in reducing excess electron populations.

We observe a significant reduction in excess electron collection when a grid was placed above the surface and biased negatively to repel the electrons from the space above the grid. Fig. 3.5 shows an example of the variation seen with changing grid bias. From Fig. 3.5(a), it is apparent that as the bias voltage on the grid goes from positive to negative values, the emission current from the Zr surface stays approximately the same, but the collection current decreases significantly. Adding the collector to this setup approximately halves the collection current again, as shown in Fig 3.4(a). Additionally, the spread in the energy distribution of the electrons (proportional to the

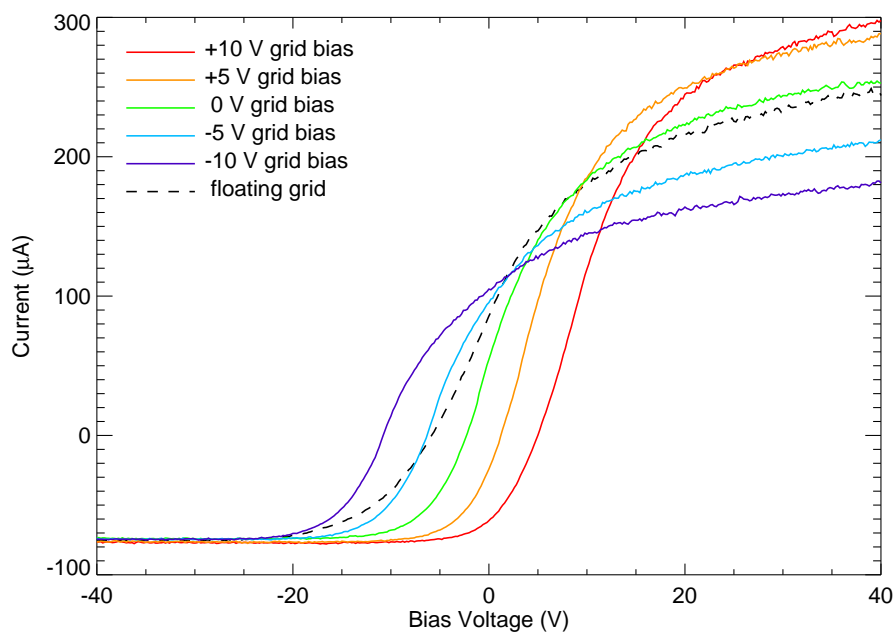


(a)

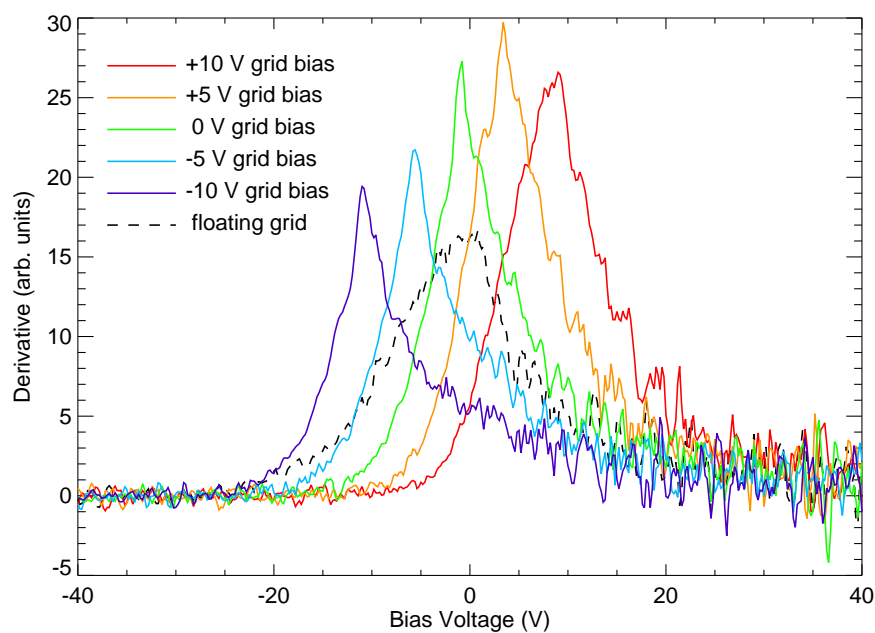


(b)

Figure 3.4: (a) Characteristic I-V probe traces from the Zr table without a grid present, with the grid over the table biased -20 V (the sweep is shifted +20 V), and with the grid (at -20 V) and collector (at +60 V) present. (b) First derivatives of the I-V curves shown in (a).



(a)



(b)

Figure 3.5: (a) Sweeps of the Zr table below the grid biased to different voltages and electrically floating. (b) First derivatives of the sweeps shown in (a). As more negative biases are applied to the grid, the overall collection of electrons decreases, as does the spread in the energy distribution.

width of the derivative peaks) decreases significantly when the grid is negatively biased, as shown in Figs. 3.4(b) and 3.5(b). The characteristics of the photoelectron populations, derived from the Zr surface sweeps, are given in Table 3.1.

Table 3.1: Data derived from Zr surface sweeps beneath a grid (and collector biased to +60 V). Characteristics are determined as described in Section 3.2.3.

Grid Bias (V)	V_f (V)	V_p (V)	I_{table} (μA)	T_e (eV)	n_e ($\times 10^{10} \text{ m}^{-3}$)	λ_e (cm)
0	0.0	0.0	46.5	1.78	2.17	5.51
-5	-3.8	-4.8	46.9	1.75	1.56	6.43
-10	-7.8	-9.4	47.2	1.68	1.46	6.52
-15	-12.2	-14.4	47.8	1.70	1.27	7.04
-20	-16.8	-19.2	48.2	1.75	1.23	7.25
-25	-21.4	-24.2	49.1	1.77	1.21	7.35
-30	-26.2	-29.2	49.3	1.80	1.14	7.63
-35	-31.0	-34.2	49.3	1.86	1.10	7.90
-40	-35.6	-39.0	49.5	1.86	1.14	7.77

3.3.1.2 Floating potential

We use a high-impedance (1 G Ω) circuit to measure floating potential on the Zr table. If the electrons emitted from the table were the only electrons in the chamber, then we would expect the Zr table (work function = 4.05 eV, lamp photons with energy ~ 7.2 eV) to float to about +3 V. However, sweeps have shown that there is clearly more collection of electrons (produced from the other surfaces in the chamber) than emission from the Zr surface, so that the table floats at a negative potential. As shown in Fig. 3.6, below about -5 V grid bias, the table potential follows the grid bias voltage, with an increasing difference between the two at more negative bias potentials. With 2 lamps illuminating the chamber, the surface floats about 0.5 V more positive than the -10 V biased grid. At very negative grid biases, the Zr table is floating to a potential that returns some, but not all, of the electrons that it emits, and the electrons from above the grid are not passing through toward the surface. However, when the grid is less negative, some of the electrons from the rest of the chamber can pass through the grid. The floating potential of the surface is

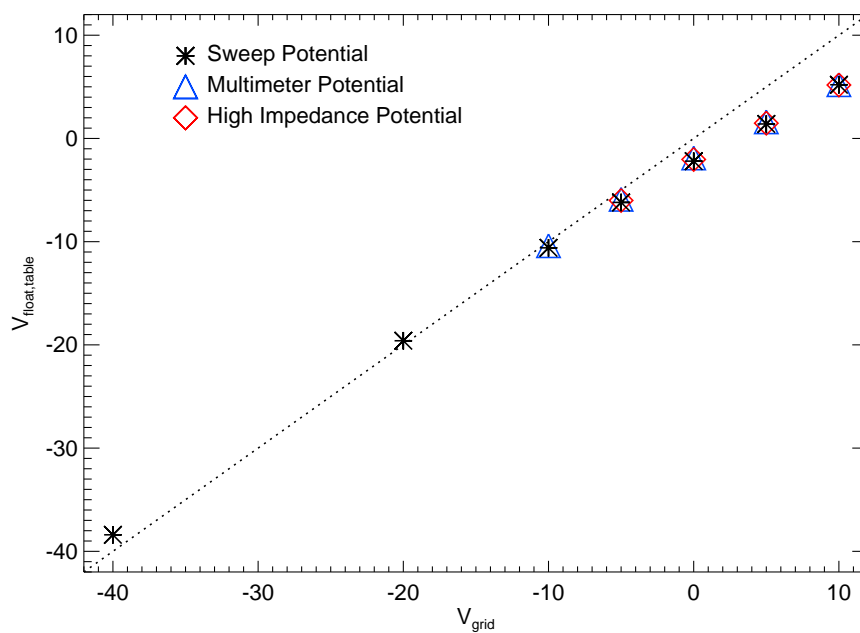


Figure 3.6: Floating potential on the table as a function of grid bias, measured by 3 different techniques: by sweeping the voltage on the Zr surface, by directly measuring the floating potential with a multimeter, and by using a high-impedance circuit.

approximately equal to the grid bias when there is a -5 V bias on the grid, indicating that the number of electrons passing through the grid are about equal to the electrons emitted from the Zr table. At biases ≤ -20 V, the Zr surface floats to a positive potential relative to the grid bias, indicating that the goal of significantly reducing the collection current has been achieved, and the system can be utilized for the studies of photoemission sheaths above the surface.

Chapter 4

Experimental studies of photoemission above a Zr surface

In our first set of photoemission experiments, we start with a study of Langmuir probes measurements over a large, planar photoemitting Zr surface, for which there is extensive modeling in the literature (Guernsey and Fu, 1970; Fu, 1971; Grard and Tunaley, 1971). Previous laboratory studies of photoelectron sheaths and the development of methods to mitigate the effects of these sheaths have been conducted in our laboratory, but were made difficult by a lack of ultraviolet sources with sufficient intensity for the observation of the photoelectric charging of surfaces and the associated space-charge electric fields. These experiments utilized a Hg-Xe arc lamp with a collimated beam to produce photoemission from surfaces (Sickafoose et al., 2000, 2001; Wang et al., 2007a, 2008). In these experiments, photoelectron populations were characterized with the retarding potential method and with Langmuir probes. Because of the small planar sheath geometry created by the limited photoemissive region, the measurements do not represent the large, planar geometry and so the sheath is likely modified due to edge effects. Additionally, the probe size is significant compared with the size of the emission region. The present experiments have nearly uniform illumination with a radial extent three times larger than previous experiments (Wang et al., 2008). In this configuration, the distance to an equipotential surface within the sheath is thus largely increased, and Langmuir probe data can be taken throughout the planar sheath and directly compared with results from a one-dimensional model.

The specific experimental setup and the diagnostic tools are described in Section 4.1, and the data are presented in Section 4.2. Results from particle-in-cell (PIC) code simulations and

their comparison to the experimental results are presented in Section 4.3. Section 4.4 provides a discussion of these results and conclusions.

4.1 Apparatus

Experiments are conducted in the vacuum chamber as described in Section 3.1. The photoemissive surface is a 50 cm diameter disk that is covered with overlapping strips of Zr foil 12.5 cm wide. In our previous work, Zr was found to give the greatest photoemission of the materials tested (Zr, Hf, Ti, and Zn) (Sickafoose et al., 2000, 2001). The surface is electrically isolated and the equipment can be operated in either one of two configurations. In the first, the surface is operated as a Langmuir probe. The bias potential of the surface is either fixed or swept in time and the current to the surface is measured. In the second configuration, the surface is connected to a high impedance voltmeter and the floating potential is recorded.

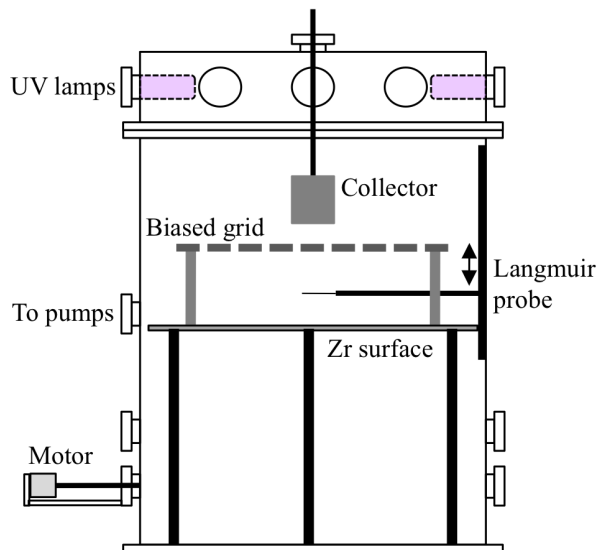


Figure 4.1: The experimental apparatus, slightly modified from Fig. 3.1. The chamber is 60 cm in diameter and 82 cm tall, and a motor moves the Langmuir probe vertically above the Zr surface. The experiment can be operated with no grid above the Zr surface, with a single grid, or with a single grid plus collector.

Data interpretation is complicated by the presence of photoelectrons emitted from the inner surfaces of the vacuum chamber. The relatively large interior surface area of the chamber ($\sim 2.5 \text{ m}^2$)

emits a photoelectron current comparable to that of the Zr surface, which is an order of magnitude smaller in area but has a larger photoelectron yield. A circular nickel wire mesh grid with 74% transparency is placed above the Zr surface to define an equipotential surface. This grid is usually biased negatively to reduce the number of electrons from the chamber walls that enter the volume between the grid and the Zr surface. The wire mesh is supported by a stainless steel ring with an outer diameter of 58 cm and an inner diameter of 28 cm, and is placed 7.6 cm above the Zr surface. The ring partially blocks UV illumination to the Zr surface hence only a region of ~ 28 cm in diameter is directly illuminated. A collecting metal sheet (the “collector”), 10×15 cm, is placed vertically above the grid, near the top of the chamber, to draw in the photoelectrons from the grid and chamber surfaces without blocking the UV photons from reaching the Zr surface.

4.1.1 Photoemission Probe

Photoelectron emission was measured as a function of distance from a single lamp using a photoelectron emission probe. This probe is a 6.25 cm^2 surface of either Pt or Zr that is operated as a Langmuir probe. Pt was used because there are accurate measurements of the photoelectron yield (Lin et al., 1971). Zr was used for comparisons with the larger photoemissive surface. The bias voltage of the emitting probe is made lower than $\sim 3 \text{ V}$ in order to prevent collection of photoelectrons from the chamber surfaces. Pt and Zr have work functions of 5.65 eV and 4.05 eV, respectively (Michaelson, 1977); the work function of stainless steel walls is assumed to be approximately the same as its constituents Fe (4.5–4.7 eV), Ni (5.15 eV), and Co (5.0 eV).

The Pt and Zr probes were each translated vertically beneath the center of a single lamp to measure the photoemission current as a function of distance. Fig. 4.2 shows the measured photoemission from the Pt, up to a distance of 17 cm, where the platinum photoemission is $1.9 \mu\text{A}$, or 3.0 mA/m^2 . For comparison, typical photoemission currents from a spacecraft surface of gold illuminated by the solar spectrum at 1 AU are $\sim 3 \times 10^{-2} \text{ mA/m}^2$, and currents from the lunar surface are in the range of $5\text{--}15 \mu\text{A/m}^2$ from solar minima to solar maxima, respectively (Sternovsky et al., 2008). The quantum yield of Pt has been measured to be $\sim 9.5 \times 10^{-4}$ at 172 nm Lin et al.

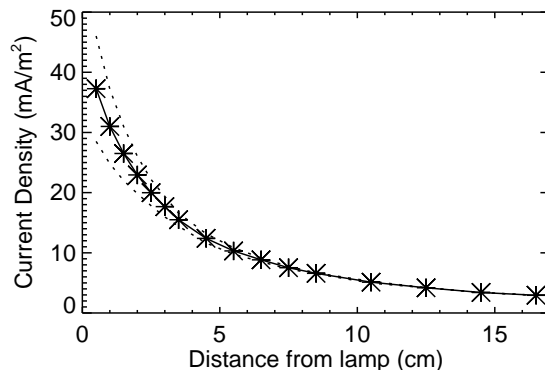


Figure 4.2: Photoemission current density (mA/cm^2) from the Pt probe as a function of radial distance from a single UV lamp. Dotted lines are the range of experimental error that represents the reproducibility of the measurements.

(1971), hence this current density corresponds to a photon flux of $\sim 2 \times 10^{19} \text{ m}^{-2}\text{s}^{-1}$. If we assume the lamp emits isotropically, this photon flux corresponds 8 W of emission, which agrees with the manufacturers stated power output (OSR, 2009). Comparison of Zr and Pt emitters of equal area shows that the quantum yield of Zr at 174 nm is $\sim 8 \times 10^{-4}$, or $\sim 84\%$ of the quantum yield of Pt.

4.1.2 Langmuir Probe

The electron density and temperature are measured by a cylindrical Langmuir probe that is a nickel wire 0.5 mm in diameter and 4 cm long. Probe sweeps are controlled by computer data acquisition system, so that the probe is swept from -40 V to +20 V in increments of 0.2 V, and each data point is an average of 5000 measurements at each voltage step. The probe is regularly discharge-cleaned to minimize surface contamination. The effective electron temperature is determined by fitting a line on a semi-log plot, that is the probe current plotted as a function of probe voltage, even though the photoelectron distribution is not necessarily Maxwellian. The density is determined from the electron saturation current, defined as the current at the voltage for which the first derivative of the $I - V$ curve has a maximum. Photoemission from the Langmuir probe surface is less than $0.05 \mu\text{A}$, which is negligible in comparison with the currents collected from other surfaces.

4.2 Experimental results

4.2.1 Current-voltage characteristics of the emitting surface

Photoemission from the Zr surface and from the chamber walls is characterized by measuring the electron current to or from the surface as a function of bias voltage. The current-voltage data, shown in Fig. 4.3a, were taken using the same circuit that sweeps the Langmuir probe. These data, taken with no grid or collector in the chamber, show that at positive bias voltages the surface collects a greater photoelectron current from the chamber surfaces than the surface emits when biased negatively. In order to observe the surface emission alone, the biased grid (described in Sec. 4.1) was placed 7.6 cm above the Zr surface. This grid is biased to -20 V (relative to the grounded chamber walls) to repel electrons from the interior surfaces of the chamber. Electrons from the chamber walls can have energies greater than the difference between the photon energy and the work function of the metal surface as a consequence of contamination. The walls have patches of insulating contamination which will charge negatively (Robertson et al., 2004). Electrons emitted from negative surfaces have their kinetic energies increased when they enter regions with electrostatic potentials that are more positive. Thus the grid bias voltage of -20 V is necessary to repel the electrons from the chamber is much more negative than one would estimate from the photon energy and work functions. Additionally, the collector (described in Sec. 4.1) is placed ~ 5 cm above the grid and biased to +60 V to collect electrons from the chamber surface that would otherwise enter the region between the Zr surface and the grid. This collector is more positive than the grid and thus also attracts photoelectrons emitted from the grid itself. Voltage sweeps with both the biased grid and collector in place show that the current emitted by the Zr surface approaches a constant value of $65 \mu\text{A}$ as the surface bias voltage is made more negative. (Note that the horizontal axis in Fig. 4.3a is the Zr surface voltage relative to the -20 V on the grid.) This relatively constant current is the photoemission current from the Zr surface with negligible contribution from the electrons from the walls.

The Zr surface – Ni grid combination acts as a retarding potential analyzer. For example,

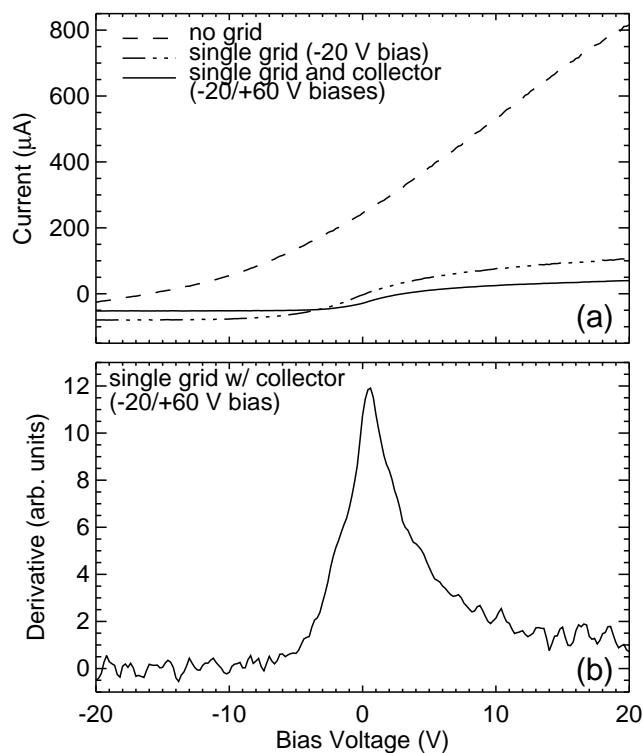


Figure 4.3: (a) Zr surface current as a function of bias voltage without a grid, with a single grid, and with a grid and biased collector to partially remove electrons emitted by the walls and the grid. The grid is biased to -20 V, and for the case of the grid plus collector, the collector is biased to +60 V. Sweeps are plotted as a function of the grid bias for these cases. (b) Derivative of the current for the Zr surface sweep with a grid and collector in the chamber.

Table 4.1: Photoelectron sheath parameters derived (1.) from sweeps of the Zr surface and (2.) from Langmuir probe sweeps taken with the Zr surface floating.

		V_f (V)	V_p (V)	J_{pe} (mA/m ²)	kT_e (eV)	n_e ($\times 10^{10}$ m ⁻³)	l (cm)
1.	Surface Sweep	-16.8	-19.2	0.78	1.75	2.46	5.12
2.	Probe Sweep	-16.8	-16.2	0.47	1.03	3.99	3.08

with the surface 1 V more positive than the grid, electrons emitted perpendicularly from the surface with more than 1 eV of energy are able to pass through the grid. The cutoff energy varies as the surface is swept hence the derivative is a measure of the axial energy distribution function. With the surface 1 V more negative than the grid, photoelectrons from the grid and other nearby surfaces are repelled from the Zr surface, and the derivative is a measure of energy distribution of these “contaminating” electrons. The electrons with many tens of electron volts of energy that come from the negative surfaces of the grid and the walls have a broad distribution and the derivative of this distribution is small relative to that of the photoelectrons from clean surfaces. The half-width at the half maximum, Fig. 4.3b, is about 3 V, which is comparable to the maximum photoelectron energy of 3.16 eV that is calculated from the difference between the photon energy (7.21 eV) and the Zr work function (4.05 eV).

For an illuminated area with a diameter of 28 cm, the emission current from the electrically floating Zr surface, J_{ph} , is ~ 0.78 mA/m² (Table 4.1). From this measurement, we also determined an emitted photoelectron temperature, T_e , by fitting the slope of the linear portion of the current on a semi-logarithmic plot as is done for the Langmuir probe. For the case of the single grid plus collector, we measured a $T_e = 1.75 \pm 0.9$ eV. We assume the photoelectrons are moving with a mean axial velocity, $v = \sqrt{2kT_e/\pi m_e}$. Thus, the density of photoelectrons emitted from the surface is approximately $n_0 = 2J_{ph}/qv = 2.5 \times 10^{10}$ m⁻³ with a Debye shielding distance of 5.12 cm; this distance is less than the spacing between the Zr surface and the grid.

A photoemitting surface in vacuum will electrically float to the potential that returns all the photoemitted electrons. For a Zr surface illuminated with 7.2 eV photons, this potential is ~ 3 V.

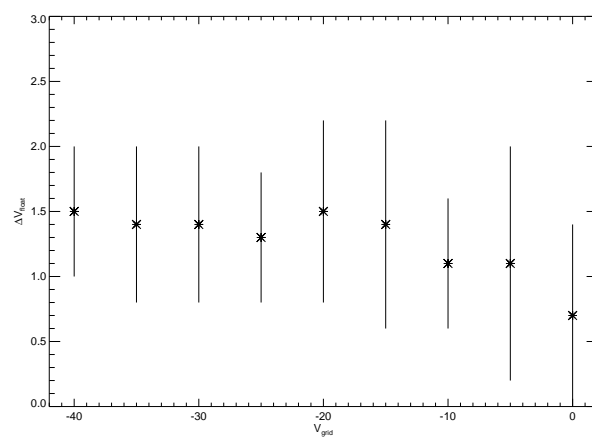


Figure 4.4: The floating potential of the Zr surface is determined by sweeping the voltage on the surface itself and determining the voltage where the current goes to zero. Data points are the voltage difference between the measurements and the grid potential, and errors are determined by the width of the peak.

In the experiment, photoelectrons from other surfaces are incident upon the Zr surface and the floating potential has the value that balances the currents to and from its surface. The nearest surface to the Zr surface is the grid, thus in the absence of photoelectrons from other surfaces, the surface should float to a potential ~ 3 V more positive than the grid potential. Fig. 4.4 shows the potential of the surface relative to the grid for a range of grid bias voltages. The surface potential is determined by two methods: (1) a high impedance (~ 1 G Ω) voltmeter; and (2) by sweeping the surface and determining when the current is zero. These two methods agree to within ± 0.2 V. The data show that the floating potential approaches +1.5 V as the grid potential is made more negative to reduce the contribution of electrons from the walls. Hence at this potential the photoemission current is equal to the current of photoelectrons that pass through the grid or are emitted from the grid.

4.2.2 Langmuir probe data

Cylindrical Langmuir probe I-V traces and their derivatives are shown in Fig. 4.5 for the standard experimental setup with a grid and collector above the biased Zr surface and the probe placed 4 mm above the Zr surface. When the probe is biased to ≤ -30 V, the measured current is primarily an emission current produced by photoemission from the probe (Wang et al., 2008); in Fig. 4.5a it is evident that, for most cases, the probe emits significantly less than the photocurrent collected from the Zr surface. Although the plasma consists solely of electrons, we use the orbit-motion-limited (OML) theory (H. Mott-Smith and Langmuir, 1926) for analysis of the Langmuir probe data because the validity of the theory is not dependent upon the presence of ions.

Fig. 4.5a shows that the current collected by the probe is greatest when the surface bias is the most positive relative to the grid, which is the condition that returns photoelectrons to the Zr surface and results in an electron distribution function that is nearly symmetric about zero velocity. For these conditions the electron temperature from the probe analysis is 1.28 eV and the density is $4.35 \times 10^{10} \text{ m}^{-3}$. As shown in Table 4.2, the density of photoelectrons just above the surface, as measured by the Langmuir probe, decreases as the surface is made more negative.

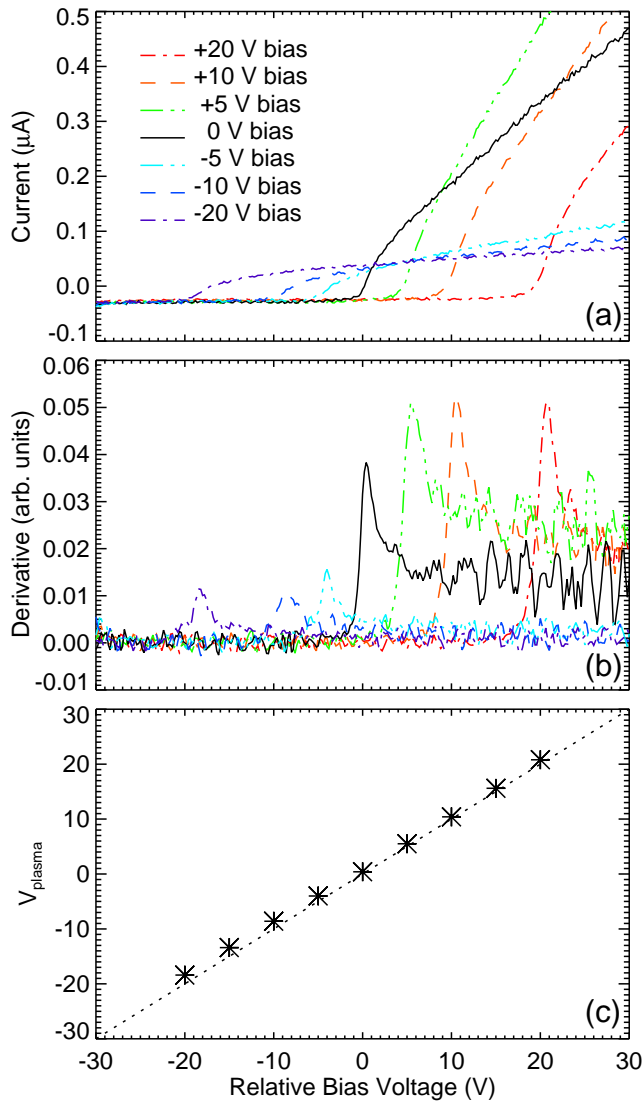


Figure 4.5: (a) Cylindrical Langmuir probe sweeps taken ~ 4 mm above the Zr surface; voltages are measured relative to the -20 V biased grid, with data plotted for surface bias voltages from $+20$ to -20 V. (b) Derivatives of the sweeps shown in (a). (c) Plasma potential at the probe location, determined from the peak in the first derivatives of the voltage sweeps.

Table 4.2: Photoelectron temperature and density data determined from Langmuir probe sweeps taken ~ 4 mm above the biased Zr surface. The surface bias is given with respect to the -20 V grid bias.

Bias (V)	kT_e (eV)	n_e ($\times 10^{10} \text{ m}^{-3}$)	l (cm)
+20	1.28 (± 0.15)	4.35 (± 0.24)	3.29 (± 0.27)
+10	1.11 (± 0.11)	3.64 (± 0.18)	3.35 (± 0.25)
+5	1.06 (± 0.10)	3.82 (± 0.18)	3.20 (± 0.22)
0	1.06 (± 0.28)	2.26 (± 0.30)	4.16 (± 0.82)
-5	1.55 (± 0.10)	0.96 (± 0.03)	7.72 (± 0.30)
-10	2.0 (± 0.11)	0.94 (± 0.028)	8.86 (± 0.35)
-20	1.64 (± 0.12)	0.80 (± 0.030)	8.70 (± 0.48)

First derivatives of the probe data are shown in Fig. 4.5b. The peak in the first derivative is identified as the plasma potential in probe data from plasma of electrons and ions. For the photoelectron data, the peak in the first derivative of the probe data is observed to be at a voltage that is always slightly above the bias potential on the emitting surface. This point is shown more clearly in Fig. 4.5c, where the location of the peak is plotted as a function of the surface bias. A detailed analysis shows that, except for very positive biases, the peak is always about 1.4 V more positive than the surface potential. Future efforts will attempt to utilize an emissive probe as an additional measurement of the potential throughout the sheath. These efforts have thus far been impeded due to the fact that the probe emission produces a large perturbation in the low density photoelectron sheath.

In Table 4.1, the temperatures and densities derived from the floating surface sweeps are shown to be different than those derived from the Langmuir probe sweeps. Electron density is related to the probe current and electron temperature by the expression $J = n_e q \sqrt{T_e / 2\pi m_e}$, where T_e is in eV and n_e is the density of electrons. This population of electrons is measured by the probe just above the surface, and can be treated as a two-sided Maxwellian distribution because the electrons are emitted from and returning to the surface, effectively doubling the measured density. This effect also explains why the densities measured by the probe (Table 4.2) increase with positive surface voltages. When the surface is biased to -20 V, the density is reduced because the electrons

are accelerated away.

4.3 Density profiles in photoelectron sheaths

Langmuir probe measurements are taken throughout the volume of the photoelectron sheath, and the data are used to derive the electron density at each height. To gain a more complete understanding of these measurements, we simulated the photoelectron sheath between the Zr surface and Ni grid using a 1-D particle-in-cell (PIC) code (described in detail in Poppe and Horányi (2010)). Emission from the Zr surface was simulated by defining a photoelectron current density such that the surface emits a Maxwellian distribution of photoelectrons with a defined $T_{e,Zr}$. Grid emission is defined as a given percentage of the surface current density and a specified $T_{e,grid}$. For this work, the current density of photoelectrons emitted from the Zr surface, determined from the experimentally measured photoemission current, is $J_{ph} = 0.9 \text{ mA/m}^2$, emission from the grid is 10% of the surface photoelectron current density, and $T_{e,Zr} = T_{e,grid} = T_e = 1.75 \text{ eV}$. Although the surface and grid electron populations are not expected to have exactly the same effective T_e , they are expected to be between 1-2 eV, and a value of $T_e = 1.75 \text{ eV}$ fit the measured densities well. The voltage on the grid was fixed at -20 V and the bias on the Zr surface boundary was varied between 0 V to -40 V, as in the experiments.

When the surface is biased very positively with respect to the grid, as illustrated in Fig. 4.6a, the surface photoelectrons are returned to the surface and the grid electrons are drawn toward the surface, so that a Langmuir probe positioned just above the Zr surface will measure contributions from both populations. When the surface is very negatively biased, photoelectrons from the Zr surface are drawn toward the grid and grid photoelectrons do not reach the surface, so that a Langmuir probe just above the surface will primarily measure the surface photoelectron population. Fig. 4.6b graphically illustrates the change in electron density due to the changing surface bias. In the case of the positively biased Zr surface, the density just above the surface will be about 2.5 times higher than that expected from a photoelectron population with only upward-directed motion, due to the returning photoelectron population and the contribution from grid electrons.

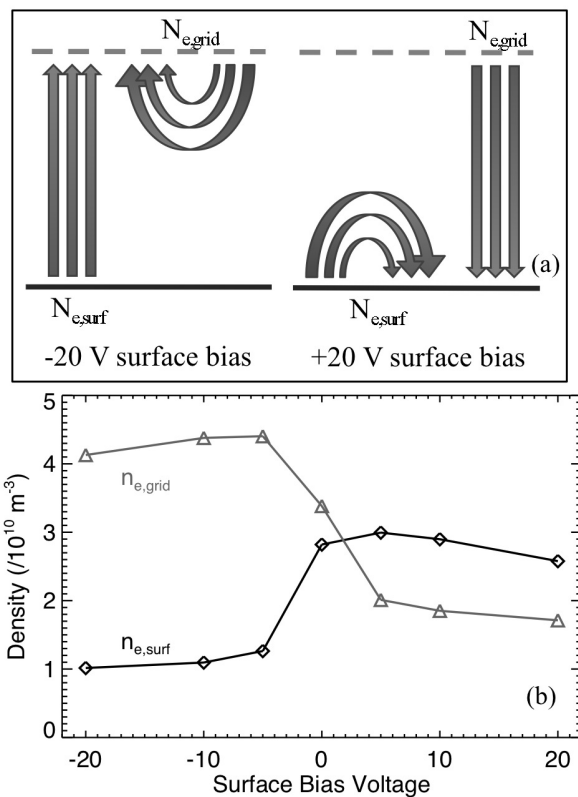


Figure 4.6: (a) Cartoon illustrating the effect of surface bias potential on the photoelectron populations. (b) Results from the 1-D PIC simulations showing the difference in densities at the Zr surface and the grid as a function of surface bias potential.

However, with the surface negatively biased, the density increases about 2.5 times just below the equipotential grid, and falls to the expected value just above the surface.

In Fig. 4.7, electron densities derived from Langmuir probe data are compared directly with PIC simulation results, which can be broken down into components from both the surface and the grid. Errors given for the derived densities are a result of the error in the temperature determination from the Langmuir probe sweep, which propagates through to the density. Overall, the measured and predicted densities show good agreement. When the surface and grid are at the same bias (Fig. 4.7, 0 V), the predicted density profile is relatively flat due to the extended Debye length; the measured densities decrease only slightly toward the grid. The data has a slight discrepancy with the simulations near the very positively biased surface. This is likely a measurement effect due to the increased electron population as a result of photoelectrons returning to, and grid electrons being drawn toward, the more positive surface.

4.4 Discussion of Zr surface photoelectron sheath results

The characteristics of photoelectron sheaths that occur at surfaces in space have been studied in the laboratory using a large planar surface of Zr illuminated by four Xe-excimer lamps each generating 8 W at 172 nm. Electron densities are measured in the photoelectron sheath between the emitting surface and a grid spaced 7.6 cm above the surface that is used to repel electrons emitted from the chamber walls. The surface-grid combination is operated as a retarding potential analyzer to determine the photoelectron density ($\leq 4.3 \times 10^{10} \text{ m}^{-3}$) and temperature (1-2 eV). The Debye shielding distance (~ 7 cm) is comparable to the surface-grid separation, thus the entire area between the surface and grid can be probed to understand the sheath physics. Langmuir probe data, analyzed by OML theory, give temperatures and densities within a factor of two of those from retarding potential analysis. A PIC simulation was used to simulate the sheath, including the electrons originating at the Zr surface and at the grid. These simulations show that the change in photoelectron density with grid bias is explained by photoelectrons from the surface being returned to the surface by a retarding potential and by photoelectrons from the grid. Densities measured

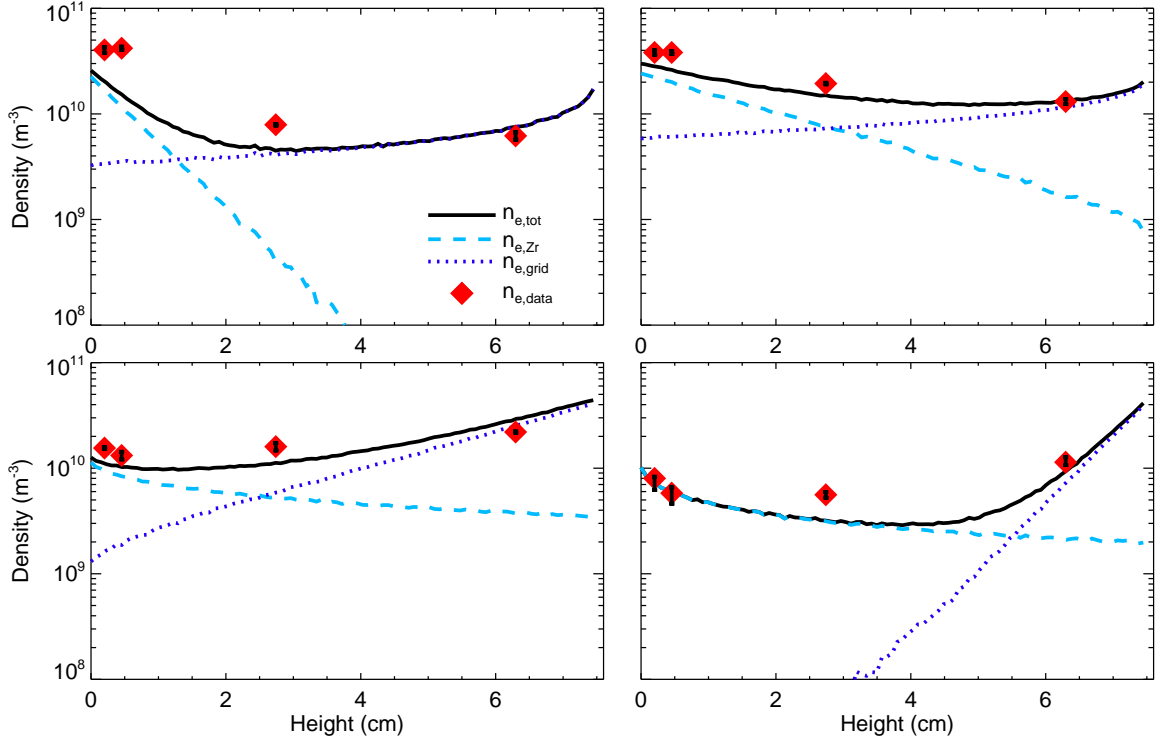


Figure 4.7: Comparisons of the electron densities from 1-D PIC simulations with experimental measurements (diamonds) derived from Langmuir probe sweeps taken at four locations between the surface and the grid. Experimental errors (for the most part are smaller than the symbol size) are a result of the error in the derivation from the temperature from the Langmuir probe sweep, which propagates through in the density calculation. The given surface bias relative to the grid bias (-20 V) is given for each plot. Each of the simulations has the same emission current from the Zr surface, $J_{e,Zr} = 9 \times 10^{-4} \text{ A/m}^2$, with emission from the grid, $J_{e,gr}$ set to 10% of the Zr surface emission, and $T_e=1.75 \text{ eV}$ for the photoelectrons from both the grid and Zr surface.

throughout the sheath by the Langmuir probe are comparable to PIC simulation results.

In these experiments, we successfully create a photoelectron sheath above a surface with sufficient density and dimensions such that we can also demonstrate the use of a Langmuir probe to determine the characteristics of the photoelectron sheath above a surface. Measurements demonstrate that a Langmuir probe whose dimensions are small compared to the area of study can accurately determine the floating potential of an underlying surface, and can also provide information about the density of the photoelectron population above the surface and how that density is affected by the surface charge. These measurements are directly applicable to the interpretation of measurements of photoelectrons above surfaces (such as metallic surfaces on spacecraft) in space. Based on this work, signals from photoelectron populations can be isolated from signals from electrons of geophysical or solar origin.

Chapter 5

Photoelectron plasmas above insulating surfaces with varied material properties

Previous work has analyzed the photoelectron sheath generated above conducting surfaces (Dove et al., 2012; Sickafoose et al., 2001; Wang et al., 2008), and these observations agree with theoretical models. Additionally, theoretical and numerical models have been developed to explain the formation of sheaths above dusty planetary surfaces (Grard and Tunaley, 1971; Singer and Walker, 1962; Walbridge, 1973; Tunaley and Jones, 1973), such as on the Moon and asteroids, but these observations have not yet been supported by experimental observations. In this set of experiments, we take an initial step toward that goal of understanding the characteristics of a photoelectron sheath formed above an insulating surface. We place CeO_2 , in solid and powder form, and JSC-1 lunar simulant in an opaque layer on an underlying Zr surface to measure the properties of the plasma generated above the surfaces. With this setup, we will begin to understand the charge balance that is controlled by the photoemission from an insulating surface, and how this balance is affected by potential differences with the surrounding region.

Section 5.1 describes the basic theory for charging of a photoemitting insulating surface in a plasma, and Section 5.2 describes the setup and experimental procedures. We present the results of measurements above the insulating surfaces in Section 5.3, and, in Section 5.4, discuss these results in the context of the charging processes above surfaces with varied material properties.

5.1 Charge balance of an insulating surface

Unlike the conducting surface utilized for experiments in Chapter 4, insulating surfaces cannot be forced to a particular bias potential. Instead, each portion of the surface will float to an equilibrium potential that balances the photoemission from the surface with an incoming population of electrons, so that the net current to the surface is zero. For a bulk collection of insulating particles, the values for the absorption and yield of the surface maybe be modified from those of the individual particles.

Photoemission from a surface is determined by the incident flux of photons with high enough energy to liberate electrons from the surface, J_γ , and the photoelectric yield of the bulk material, Y . Assuming the photoemitted electrons are a Maxwellian population, the resulting photoemission current is

$$J_{pe} = Y J_\gamma \exp\left(-\frac{e\phi_s}{T_{pe}}\right), \quad (5.1)$$

where ϕ_s is the surface potential and T_{pe} is the mean energy of the photoelectrons. This equation also assumes that the absorption of the photons approaches unity, and that all photoemitted electrons escape the surface and are not reabsorbed onto other particles. An additional factor could be included to account for these loss mechanisms. If photoemission from the surface is the only source of electrons, this will be the current from the surface. If an additional electron component is also present due to photoemission from the surrounding surface, the photoemission current is balanced by an electron collection current determined simply by the random current density to the surface,

$$J_e = n_e \left(\frac{T_e}{2\pi m_e}\right)^{1/2}, \quad (5.2)$$

where n_e and T_e are the electron density and temperature of the collected electrons, and m_e is the electron mass.

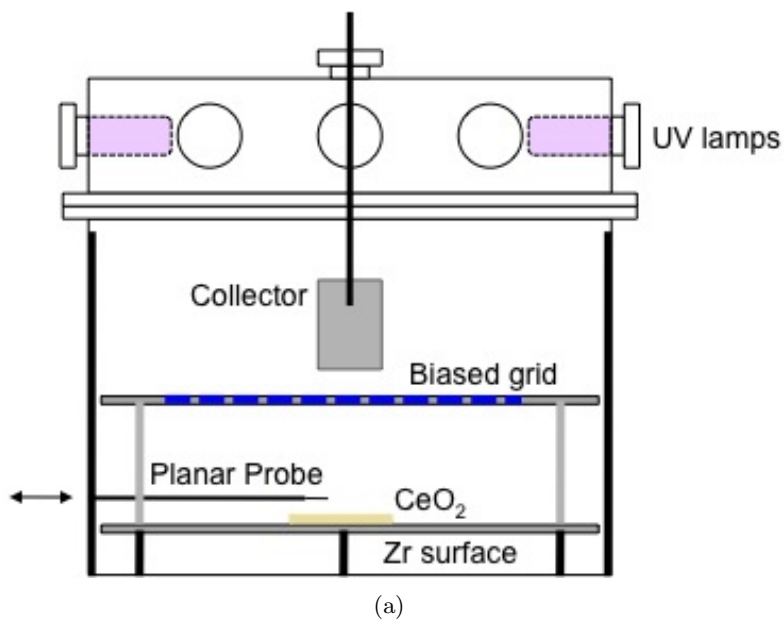
5.2 Experimental Setup

Experiments are conducted in the chamber described in Chapter 3, with the same grid and collector setup that successfully reduced excess electron emission for the Zr experiments (Chapter 4;

in all experiments, the grid is biased to -20 V and the collector is biased to +60 V (Fig. 5.1(a)). In addition, insulating materials are placed on the Zr surface, in the center of the chamber - this placement ensures uniform illumination, and allows for measurements utilizing both the cylindrical Langmuir probe and the single-sided planar Langmuir probe. For some of the experiments presented here, photoemission from the surface is significantly less than that from the Zr surface in the previous experiments. In these cases, the cylindrical probe collection current is not significantly greater than the probe photoemission current. In previous experiments (Wang et al., 2008), probe photoemission was reduced by coating the probe in graphite; however, because of the higher energy of the photons in this set of experiments, coating the probe does not have a measurable effect. Because it is not straightforward to remove such a significant current from the signal, the cylindrical probe cannot be used to derive the electron temperatures and densities for these experiments.

Instead for consistency we use only the single-sided planar Langmuir probe for all experiments. The probe is oriented parallel to the surface, with the tantalum (collecting) side facing downward, toward the surface, and the ceramic side facing the UV lamps. With this geometry, the downward-facing probe surface is not directly illuminated by the UV photons and probe photoemission is largely reduced. The probe is manually controlled to move horizontally above the surface, beginning at $r = 0$, above the center of the insulating material, and moving radially outward so that probe measurements are taken above the insulator and Zr surface in the same experiment.

Figure 5.1 shows the three types of insulating surfaces used in this experiment. CeO_2 was chosen as the initial insulating material to be used in this study because of its photoemissive characteristics. Various size distributions of CeO_2 have been used in dusty plasma experiments, including those aboard the Mir space station (Fortov et al., 1998). Table 5.1 lists the relevant material properties of the CeO_2 . The high yield of this material is the most useful property for these experiments, as it ensures that UV illumination will create a population of photoelectrons with a measurable current. A solid disk of CeO_2 and CeO_2 powder are both used to enable comparison of the effects of the surface roughness. Additionally, JSC-1 lunar soil simulant (Table 5.1) is utilized to represent lunar soil properties. JSC-1 fairly accurately reproduces the spectral characteristics of



(b)



(c)



(d)

Figure 5.1: (a) Diagram of the chamber setup for the experiments with insulating material on the surface. Images of the (b) solid CeO_2 , (c) CeO_2 powder, and (d) JSC-1 lunar simulant on the Zr surface. The grid is shown over the surface in (b), and both the cylindrical and planar Langmuir probes are visible in (c) and (d).

lunar mare, and so is a reasonable proxy for our experiments. The yield of bulk JSC-1 under UV illumination is not known, but it is expected to be slightly lower than that of CeO₂.

Table 5.1: Values of the particle radius, r_p , the work function, W , and the quantum yield, Y of the insulating materials used in this study and lunar soil samples for comparison.

^a(Michaelson, 1977), ^b(Dove et al., 2012), ^c(Fortov et al., 1998), ^dmean radius (McKay et al., 1994), ^e(Sternovsky et al., 2002), ^f(Willis et al., 1973)

Material	r_p	W (eV)	Y
Zr (solid)	–	4.05 ^a	few x 10 ⁻⁴ [^b]
CeO ₂ (solid)	–	3 ^c	10 ⁻² [^c]
CeO ₂ (powder)	15 nm	3 ^c	10 ⁻² [^c]
JSC-1 (dust)	~ 105 μ m ^d	5.6 ^e	–
Lunar soil	bulk	5 ^f	7x10 ⁻² max (at 90 nm)[^f]

5.3 Experimental results

5.3.1 Current measurements

Figure 5.2 is an example of probe sweeps over each of the insulating surfaces (for the case shown here, the Zr surface is grounded). Additionally, Zr surface sweeps from the same experiments are plotted; these are obtained by sweeping the probe in a region of the surface not covered by the insulator (at $r = 11$, or about 11 cm from the center of the surface). Although the Zr sweeps are not taken in the center of the chamber, the illumination is approximately uniform in the entire area under the grid, so that these values can be directly compared. For the most part, the photoemission current from the dusty insulating surfaces is less than that from the Zr surface. As shown in Fig. 5.2, the currents are large enough to produce a measurable signal, and, in the case of the solid CeO₂, the current is actually stronger than that from the Zr surface. This is not surprising, considering the high value of the photoelectron yield of CeO₂; however it is interesting that the emission from CeO₂ powder is highly reduced.

To get an estimate of how the probe collection current varies both between the insulating surfaces and relative to the Zr, we take a ratio of the probe collection currents over the insulating and Zr surfaces. The value for the probe collection current is measured over the center of the

insulating patch, and then a few centimeters away from the edge of the insulator, over the Zr. We take an estimate of the ratios at the measured plasma potential, and average over 1 V to get the mean and standard deviation shown in Table 5.2. Several interesting features emerge from this analysis. First, as stated above, the probe collection current over the solid CeO₂ is always greater than or equal to that over the Zr. The probe collection current in the case of the negatively biased surface is high for all of the insulating materials; this will be discussed more in Section 5.4.

Table 5.2: Ratio of the probe collection currents measured above the given insulators to the probe collection current measured over the Zr in the same experiment. See text for method of determining these ratios.

Insulator	Zr surface bias			
	float	-20 V	0 V	+20 V
CeO ₂ (solid)	0.99 (± 0.02)	1.67 (± 0.02)	1.14 (± 0.02)	1.70 (± 0.02)
CeO ₂ (powder)	0.22 (± 0.02)	0.80 (± 0.01)	0.32 (± 0.02)	0.34 (± 0.01)
JSC-1	0.42 (± 0.01)	0.72 (± 0.01)	0.56 (± 0.01)	0.95 (± 0.01)

Table 5.3: Relative photoemission currents from the probe, measured above the given insulators and normalized by the probe photoemission current measured over the Zr in the same experiment. All values have a standard deviation of 0.001.

Insulator	Zr surface bias			
	float	-20 V	0 V	+20 V
CeO ₂ (solid)	0.69	1.00	0.78	0.75
CeO ₂ (powder)	0.69	0.68	0.63	0.64
JSC-1	0.67	0.70	0.62	0.60

Not only does the probe collection current provide information about the surface emission, but when $V_b < V_{pl}$, the probe sweeps also can tell us something about the underlying surface. As mentioned in Section 5.2, the downward-facing planar probe should produce very little photoemission, as the UV-facing surface is coated in a ceramic, and thus will not contribute to the signal. Neither the Zr surface nor the insulating surfaces are perfectly smooth, however, so there could be some extra scattering of light onto the probe. Additionally, there is enough reflection of the UV photons from both the Zr and insulating surfaces to produce a measurable photoelectron current

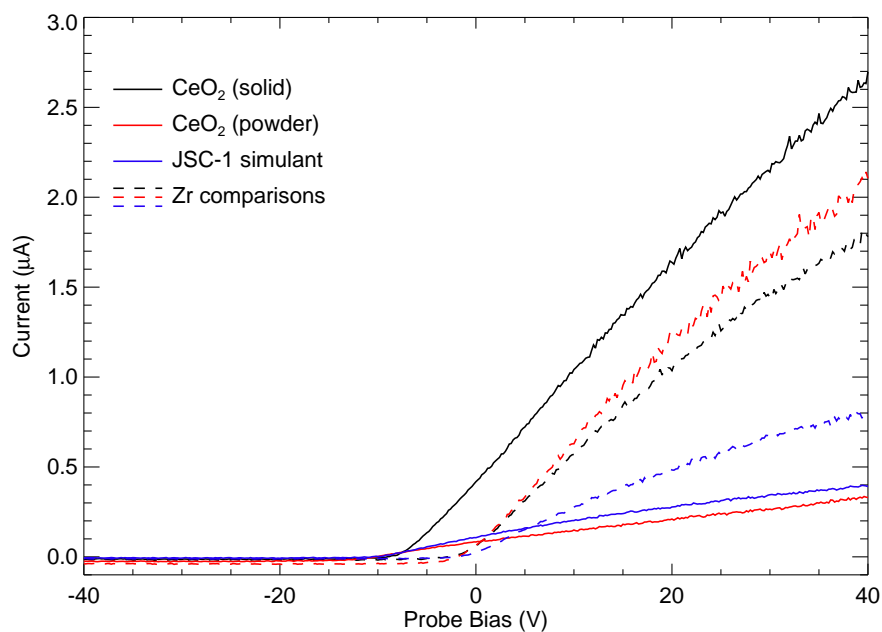


Figure 5.2: Single-sided planar probe sweeps, highlighting the probe collection currents over the insulating (probe at $r = 0$) and Zr (probe at $r = 11$) surfaces when the Zr surface was grounded. Solid lines are the measurements over the insulators, and the dashed lines are the measurements over the Zr for the same experiments. The overall reduction in current for the blue lines is the result of a low photon flux from the UV lamps for the JSC-1 experiments.

from the probe. In Table 5.3, the photoemission current measured by the planar probe over the insulating surfaces is normalized by the photoemission current measured by the planar probe over the Zr surface (at the same locations as the collection current measurements). This gives a ratio of the probe relative photoemission currents, and it also eliminates the effects of day-to-day variations due to the UV photon flux from the lamps.

As far as we know, this is a previously undiscussed application of Langmuir probe measurements. In addition to being used as probe of electrons emitted from the surface, we find here that the probe is sensitive to those photons that are reflected back toward the probe. The reflectance is not sensitive to the Zr surface bias, which is a further indication that this is an effect of photon reflection and the UV albedo, and not due to an additional electron current. All of the insulators reflect around 60–70% of the smooth Zr surface, and it appears that the solid CeO_2 maybe have a slight enhancement over that, as well. This is likely attributed to the surface roughness; a smooth surface is expected to reflect back more directly than a rougher surface, which will have more scattered, diffuse reflection. Although surface roughness appears to be the dominant effect in this experiment, we would also expect results to vary over different mineralogies.

5.3.2 Potential measurements

Beyond looking at the basic features of the probe currents, we can determine both the plasma and floating potentials from the probe sweeps (Table 5.4). The measured current is only significantly affected by electronic noise levels in a few cases (predominantly when the surface is negatively biased), and in these cases the floating potentials are the most cleanly determined data. The floating potential represents the balance between the photoemission current from the probe and the electron collection current. By using the downward facing probe, in theory, there should be no photoemission from its surface; however, as discussed above, some light is reflected from the underlying surfaces, producing a photoemission current. Ideally, with this downward-facing probe, all of the measured collection current is due to upward-directed photoelectrons from the underlying surface. Because of the low photoelectron density, the Debye length is long in these systems, so that

the probe, which is only a few millimeters above the surface, is always within the plasma sheath, and is thus most sensitive to the electron population emitted from the surface.

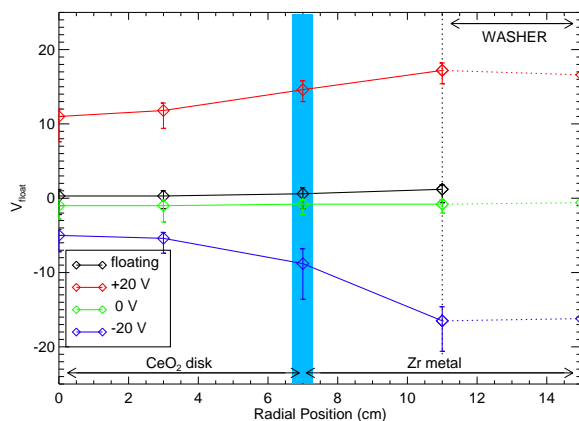
Table 5.4: Properties of the photoelectron plasma generated over the insulating surfaces, derived from single-sided planar Langmuir probe measurements. Zr surface bias is given with respect to the -20 V biased grid, and errors on V_{pl} and V_{fl} are determined by data collection to be approximately 0.2 V. Standard deviations given for T_e , n_e , and λ_e are determined from the error in fitting the slope of the linear portion of the $I - V$ curve.

	Zr surface bias (V)	V_{pl} (V)	V_{fl} (V)	T_e (eV)	n_e ($\times 10^{10} \text{ m}^{-3}$)	λ_e (cm)
CeO ₂ (solid)	float	2.8	0.4	1.3 (± 0.05)	3.6 (± 0.07)	3.6 (± 0.10)
	-20	-2.2	-5.0	1.3 (± 0.17)	5.1 (± 0.32)	2.9 (± 0.03)
	0	1.0	-0.8	1.1 (± 0.07)	3.6 (± 0.12)	3.3 (± 0.16)
	+20	15.8	11.0	2.5 (± 0.45)	5.8 (± 0.53)	4.0 (± 0.55)
CeO ₂ (powder)	float	2.1	1.1	2.1 (± 0.07)	1.1 (± 0.02)	8.7 (± 0.21)
	-20	-5.4	-8.0	3.1 (± 0.06)	1.6 (± 0.02)	8.5 (± 0.12)
	0	0.9	0.4	2.4 (± 0.06)	0.9 (± 0.01)	9.8 (± 0.18)
	+20	11.1	9.8	2.8 (± 0.18)	0.7 (± 0.02)	12.2 (± 0.56)
JSC-1 simulant	float	2.9	0.5	1.5 (± 0.10)	1.1 (± 0.04)	7.2 (± 0.33)
	-20	-3.4	-5.9	2.2 (± 0.46)	1.0 (± 0.12)	9.4 (± 1.33)
	0	0.9	-0.2	1.1 (± 0.16)	1.2 (± 0.07)	5.7 (± 0.59)
	+20	11.9	9.8	1.7 (± 0.11)	0.8 (± 0.03)	9.3 (± 0.47)

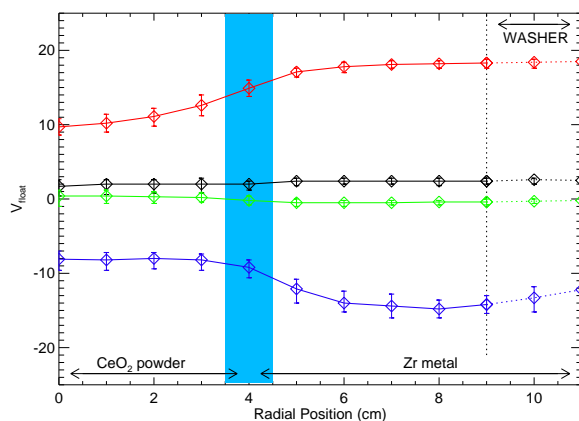
Figure 5.3 shows the variation in the measured floating potential as a function of radial distance from the center of the experiment. At $r = 0$, the probe is above the center of the patch of insulating material, and with increasing r , the probe position is moved toward the edge of the insulating material (indicated by the vertical blue bar) and then over the uncovered Zr. The last few centimeters of the plots (to the right of the dashed vertical line) show that the probe is under the “washer” that supports the grid; this effectively blocks most of the direct UV illumination and significantly reduces the flux of UV photons to the surface. Both the photoemission and collection currents are reduced in this region.

The floating potential is uniform across each of the insulating and Zr surfaces, with a smooth increase in the magnitude of the potential across the transition region. When the Zr surface is biased positively, the floating potential over the insulating materials is more negative, and when the Zr surface is biased negatively, the floating potential over the insulating material is more positive.

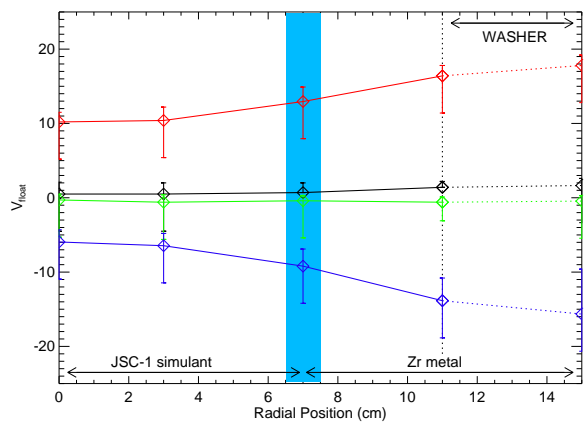
Figure 5.3: Floating potential measured by the single-sided planar Langmuir probe above (a) CeO_2 solid, (b) CeO_2 powder, and (c) JSC-1 simulant, as function of radial distance, r , above the surface. Potentials are given with respect to the -20 V grid bias. Error bars are determined by the voltage range over the current ± 0.1 A from the determined floating potential. The blue bar marks the approximate transition region from the insulator to the Zr surface, and the horizontal dashed line marks where the probe is under the “washer” of the grid.



(a)



(b)



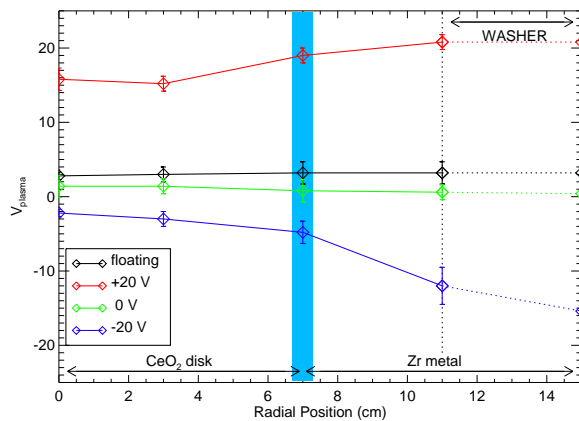
(c)

When the Zr surface is biased to 0 V, the floating potential over the insulating materials (most clearly seen in Fig. 5.4(b)), is slightly more positive than over the Zr surface. On the other hand, the floating potential above the insulating surfaces tends to be more negative than that above the Zr surface.

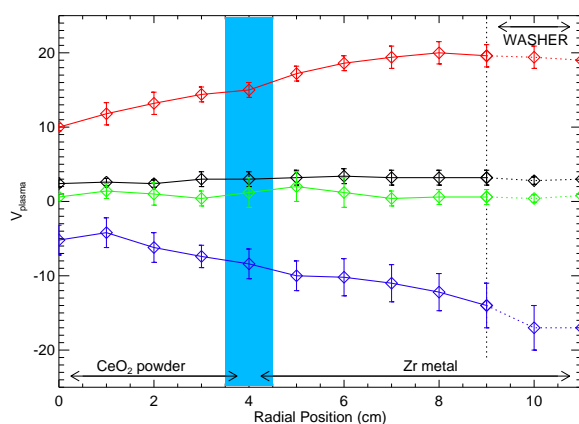
The plasma potential measurements (Fig. 5.4, Table 5.4) exhibit the same trends as those observed for the floating potentials. As expected from probe theory, the plasma potentials are more positive than the floating potentials. The most noticeable effect on the plasma potential occurs when the Zr surface is negatively biased (at -20 V); while the measured plasma potential above the Zr surface is close to this bias, the plasma potential above the center of the insulating surfaces never becomes more than about -5 V negative.

The features of these potential measurements can be explained as follows. In the absence of any additional electric field or electron source, the photoemitting insulating surface will tend to charge to approximately 1–3 V, as determined by the mean energy of the emitted electron population, which is a function of the difference between the UV lamp photon energy (7.2 eV) and the insulating surface work function. This is evident in the probe data for the case when the surfaces are floating, and the surfaces are observed to charge as expected. With the addition of the grid and surrounding Zr surface, the system has added complexity. We will discuss each of the biased cases shown.

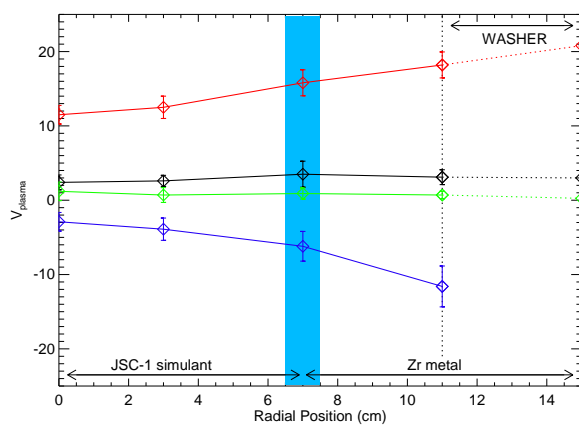
- (a) **0 V** When the Zr surface is forced to the same bias as the grid, there is only a very weak electric field present due to the electron populations. Because the surfaces are photoemitting, the insulator comes to a net positive equilibrium charge, as discussed above. In this case, however, the electrons from the slightly more negative Zr surface will be attracted to the insulating surface, so that the surface will charge less positively than in the floating case.
- (b) **-20 V** When the Zr surface is biased to -20 V with respect to the grid potential, an upward-pointing electric field is set up between the surface and grid. In this case, the plasma (and floating) potentials measured by the probe above the insulating surface are found to be



(d)



(e)



(f)

Figure 5.4: Plasma potentials measured by the single-sided planar Langmuir probe above (a) CeO_2 solid, (b) CeO_2 powder, and (c) JSC-1 simulant, as function of radial distance above the surface. Potentials are given with respect to the -20 V grid bias. Error bars are determined by the half-width at half-max of the peak in the current sweep derivatives. Additional features of the plot are described in Fig. 5.3.

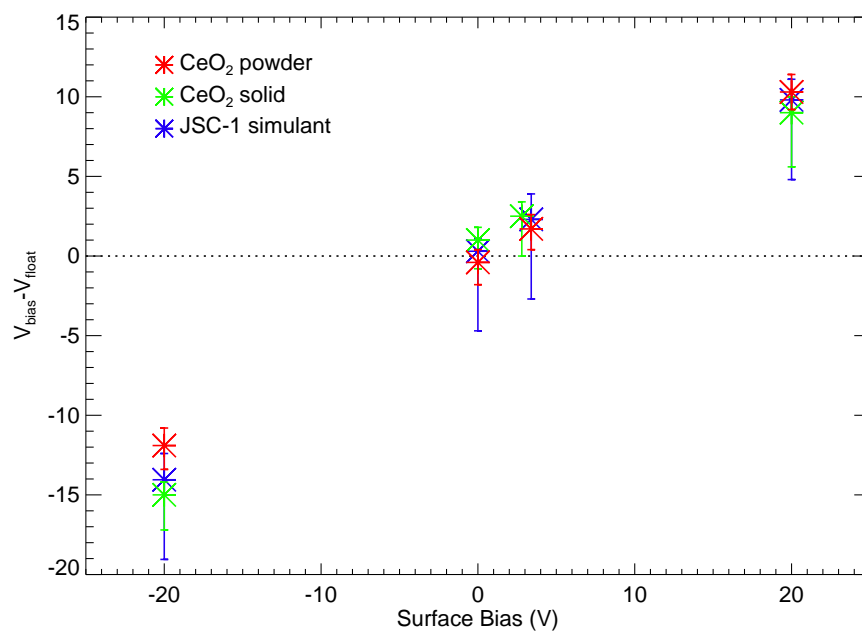
negative, although not as negative as the bias potential. This results from an amplified effect of the previous case. An additional electric field component will point toward the insulating surface, so that electrons from the Zr surface are attracted to the more positive insulator surface. Because the total amount of photoemission from the Zr surface is greater than from the insulating surfaces (due to the fact that there is more surface area of the Zr that can photoemit, and because the yield is higher than the dusty surfaces), this current of electrons will force the surface potential of the insulator more negative. This is supported by the fact that the solid CeO_2 charges less negatively than the dusty surfaces because it has a stronger photoemission current to balance that from the Zr.

(c) **+20 V** Finally, when the Zr surface is biased positively with respect to the grid (+20 V), a downward-pointing electric field is set up between the surface and the grid. The insulating surfaces charge less positively than their surroundings in this case. This sets up an electric field pointing outward from the insulator toward the Zr. The electrons must have slightly higher energies to move through the vertical electric field, and this current of electrons away from the insulating surface results in a more positive charge on the insulating surface.

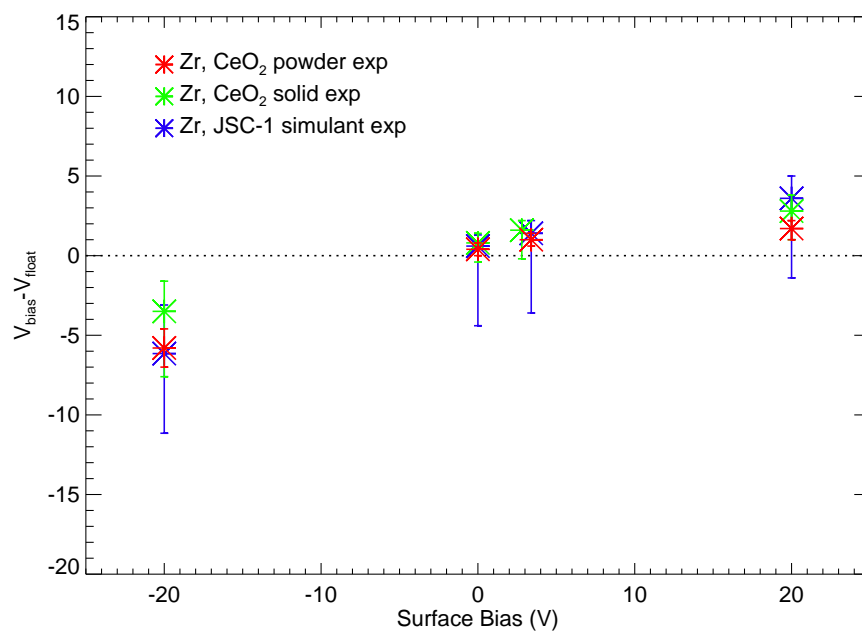
These effects are well-illustrated in Figs. 5.5 and 5.6, where the differences between the floating (or plasma) potential and the surface bias potential are plotted as a function of surface bias. For the case of a biased conducting surface, as in the Zr, the floating and plasma potentials are forced to closely follow the bias voltage (as shown in Figs. 5.5(b) and 5.6(b), and discussed further in Chapter 4). However, the voltage on an insulating surfaces is not set by the applied bias voltage, and thus will float to an equilibrium surface potential.

5.3.3 Densities

Figure 5.7(a) shows the derived densities above the three insulating surfaces as a function of the bias voltage on the surrounding Zr surface, with linear fits to the data that show very shallow slopes. These densities indicate that there is a minimal, if any, dependence of the density above the

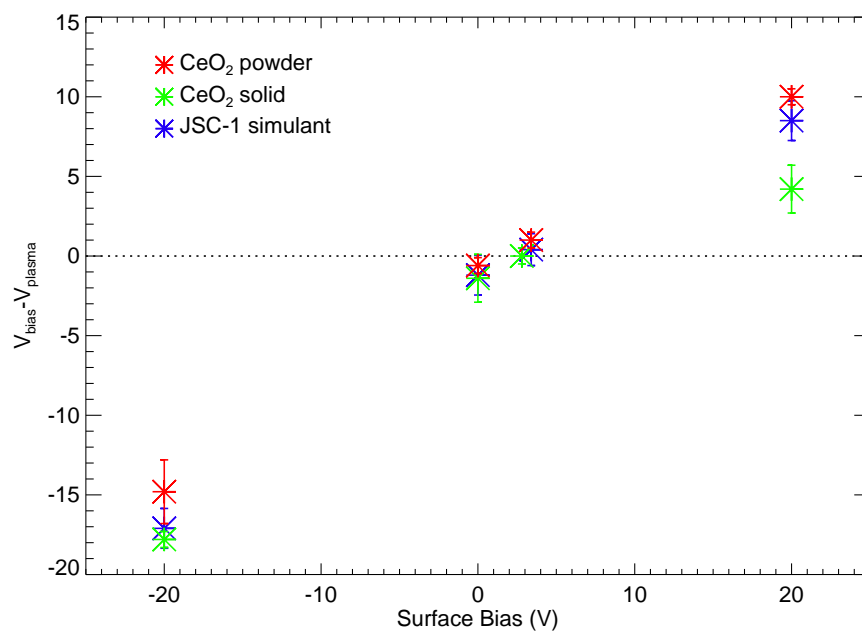


(a)

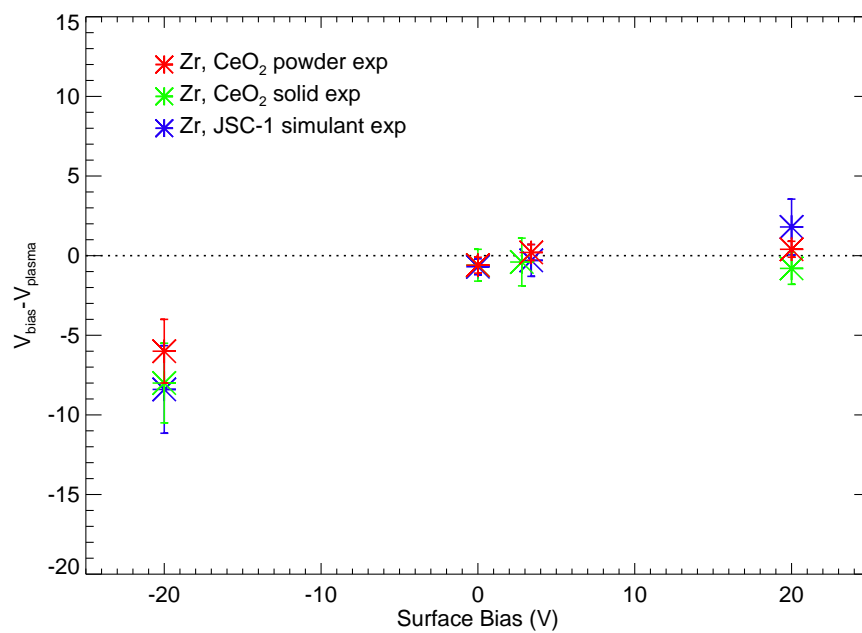


(b)

Figure 5.5: Difference between the floating potential measured with the single-sided planar Langmuir probe above (a) the insulating surfaces and (b) the Zr surface and the bias potential applied to the Zr surface (given with respect to the -20 V bias on the grid). Error bars are determined by the voltage range over the current ± 0.1 A from the determined floating potential.

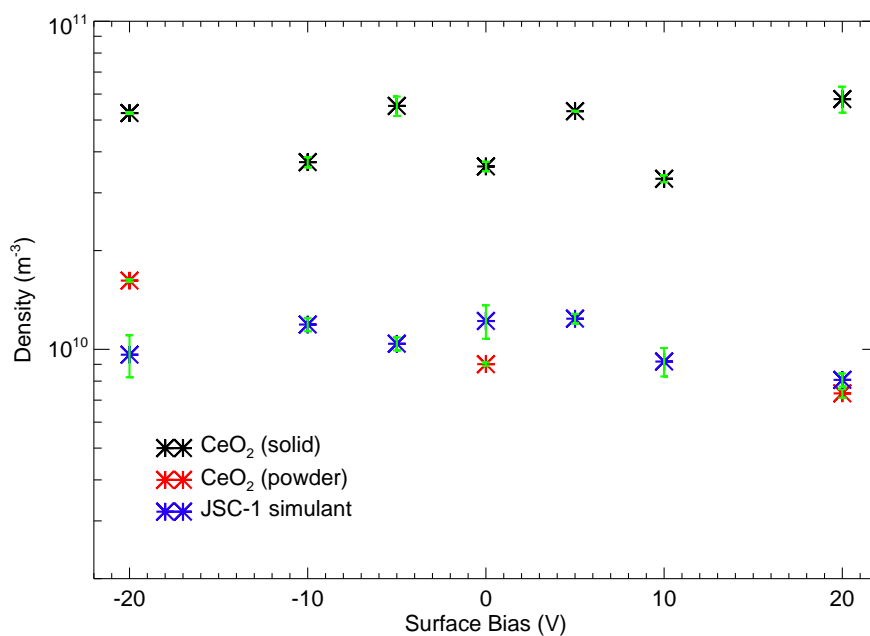


(a)

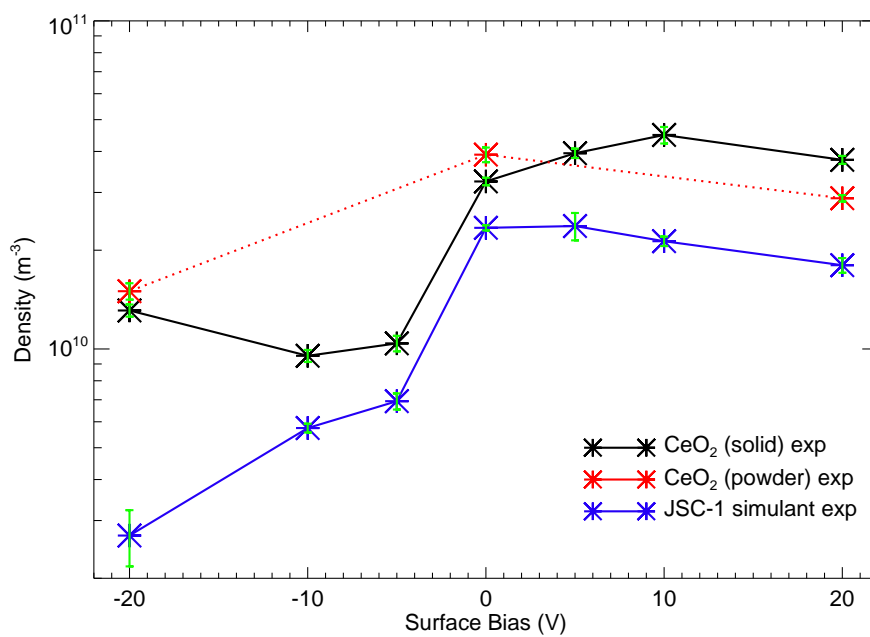


(b)

Figure 5.6: Difference between the plasma potential measured by the single-sided planar Langmuir probe above (a) the insulating surfaces and (b) the Zr surface and the bias potential applied to the Zr surface (given with respect to the -20 V bias on the grid). Error bars are determined by the half-width at half-max of the peak in the current sweep derivatives.



(a)



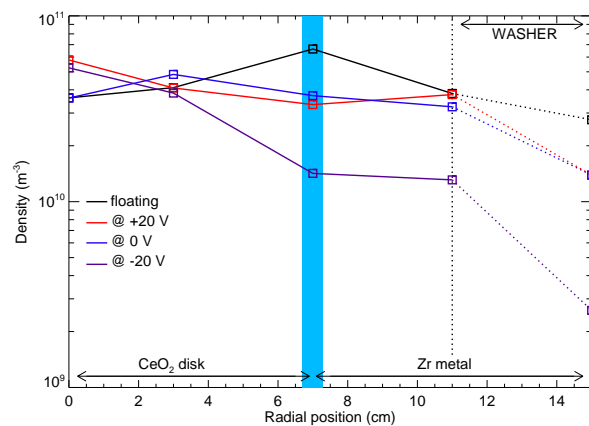
(b)

Figure 5.7: Densities derived from the single-sided planar Langmuir probe data above (a) the insulating surfaces, and (b) the Zr surface for each of the different insulator experiments, as a function of the surface bias (given with respect to the -20 V grid bias). Errors are a result of the error in the derivation from the temperature from the Langmuir probe sweep, which propagates through in the density calculation.

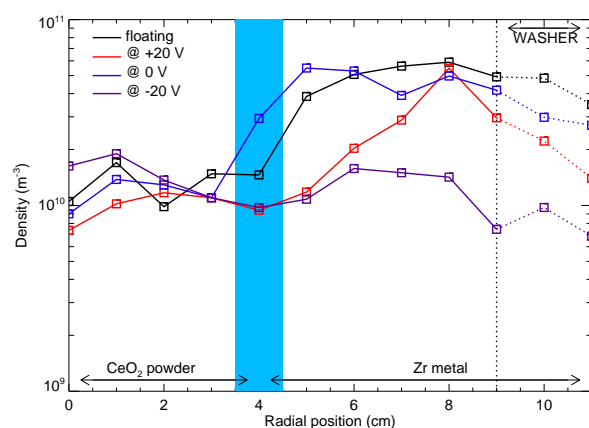
insulating surfaces on the bias of the Zr surface, unlike the Zr surface itself (as seen in Fig. 5.7(b) and Chapter 4). This reflects the fact that the photoemission from the insulating surfaces is controlled by the balance of currents, and is coupled to the surface bias by the electric field that is set up between the biased grid and surface. The density is only slightly modified by the change in electron population from the surrounding regions, which indicates that these measurements are dominated by and representative of the density of photoelectrons emitted from the insulating surfaces.

Unlike the relatively flat profile of density as a function of bias voltage observed above the insulating surfaces, the densities measured above the Zr surface show an interesting dichotomy. There appears to be a potential threshold, below which the densities are a factor of 2–3 times lower than those above the threshold. This effect was observed, with even greater magnitude, for the cylindrical Langmuir probe above Zr (Dove et al., 2012), but with an ideal, single-sided planar probe, we do not expect to measure a smaller difference. Several factors may account for the observed densities. As previously mentioned, the Zr surface is not perfectly smooth, and the probe might not be exactly parallel to the surface, so that additional electrons that leave the surface at an angle could impact the probe. Also importantly, these measurements are taken *within* the sheath. Thus, at positive biases, the probe could see an effect of the doubled electron population as electrons return to the surface. The probe could measure these electrons due to the angle effects just mentioned, and/or because of edge effects that occur for real probes that have physical dimensions and edges that are not accounted for in the ideal theory. If the probe were outside of the sheath, we expect to observe the opposite effect for the electron densities.

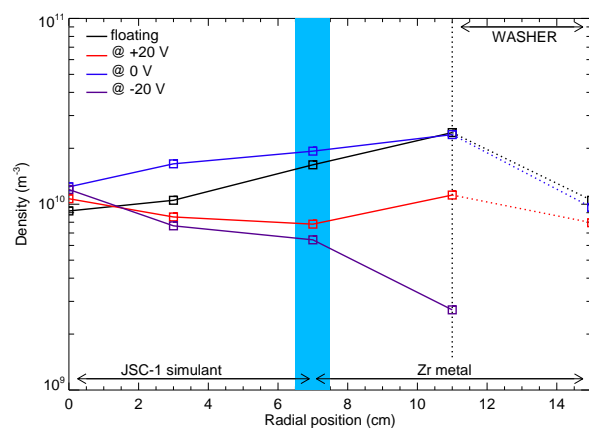
Additional interesting features are observed when the density is plotted as a function of the radial position above the surface. As expected from the observations of elevated collection currents (Table 5.2), the density above the CeO₂ solid is comparable to or greater than the density measured above the Zr surface, and is greater than that above the other two insulating surfaces. Finer resolution of measurements above the CeO₂ powder surface (Fig. 5.8(b)) shows the details of where the densities drop off slightly at the transition between the insulating and conducting surfaces, and then increase again over the Zr surface. Finally, the densities measured over the



(a)



(b)



(c)

Figure 5.8: Photoelectron densities measured by the single-sided planar Langmuir probe above (a) CeO₂ solid, (b) CeO₂ powder, and (c) JSC-1 simulant, as function of radial distance above the surface. Additional features of the plot are described in Fig. 5.3. Errors are a result of the error in the derivation from the temperature from the Langmuir probe sweep, which propagates through in the density calculation.

JSC-1 lunar simulant are comparable to those over the CeO_2 powder. This is an unexpected result because the work function of CeO_2 is lower than that of JSC-1, and the yield of CeO_2 is assumed to be higher. However, it is possible that the yield of the simulant is greater than expected; in previous experiments with Apollo dust samples, Willis et al. (1973) measured a peak in the photoelectric yield around 900 Å, and although the curve for the lunar samples then turned over and decreased toward 500 Å, the yield curves for bulk insulators tend to increase toward short wavelengths. Alternatively, electrons emitted from a rough surface may re-impact upon another portion of the surface, resulting in less net emission to the surrounding environment.

5.4 Discussion and conclusion

Planar Langmuir probe sweeps above photoemitting insulator surfaces show significant differences in the potentials compared to the measured potentials above a photoemitting biased Zr surface, and some differences between the materials themselves. Measured temperatures of the emitted photoelectron populations are around 1-2 eV for all three of the insulators, which is within the range of temperatures expected above insulators exposed to 7.2 eV photons. CeO_2 powder has the highest derived temperatures, which could be due to the ~ 4 V difference between the UV lamp photon energy and the work function of CeO_2 .

Analysis of the CeO_2 powder properties in light of the other two surfaces allows us to interpret the relative role of different material properties. First, the fact that the photoemission current is less than that from the solid CeO_2 illuminates the fact that photoemission from surfaces is affected by surface roughness. This effect has also been observed in the production of secondary electrons; Martin and von Engel (1977) observed an approximately five-fold decrease in the production of secondary electrons from soot than smoother graphite, and Wang et al. (2010) observed that the secondary electron production above dusty surfaces exposed to an electron beam was significantly lower than that from the surrounding graphite plate. Second, because the photoemission currents from the CeO_2 powder are more similar to those from the JSC-1 than the solid CeO_2 , this suggests that surface roughness plays a bigger role in determining the net amount of photoemission from

a surface than the work function or yield. Additional experiments that more carefully control for these parameters can be done to evaluate the relative importance of each of these factors.

While this experiment was originally designed to measure the properties of a photoelectron sheath generated above an insulating surface, this setup lends itself to interpretations of charge transfer between two surfaces with different charge densities. The probe measurements taken above the floating surfaces are the least affected by charge transfer between the surfaces, as is seen by the plasma potentials that approach the expected values, and so are most representative of the isolated insulating surface charging situation. The cases of the biased surfaces, however, are representative of situations that occur on the lunar surface, on spacecraft, and in other natural environments, where regions of differential potential are adjacent. The potential structures, electric fields, and magnitude of charging will be affected, whether these surfaces are naturally differentially charged, or the difference is due to the presence of an object such as a spacecraft body.

In this set of experiments, utilizing the Langmuir probe measurements with standard analysis techniques has accurately measured the characteristics of photoelectrons emitted from CeO₂ and JSC-1 surfaces, as well as the potentials in the plasma above those surfaces, to characterize the photoelectron sheath and plasma currents. Although not a standard use of Langmuir probe measurements, we also observe that the Langmuir probe sweeps may provide a useful measurement of the UV photon reflectance from surfaces, or UV albedo, and use of this technique should be explored further.

Langmuir probes are compact, simple instruments capable of measuring plasma properties in a wide variety of environments. Beginning with the experiments done by Wang et al. (2008), we have seen that a significant amount of information can be gleaned by placing a Langmuir probe above the lunar surface. This work has shown that there is more capability than previously thought, but also that many factors can change the signal measured by a Langmuir probe, and that they are not easily identifiable. For instance, the UV albedo of the lunar surface varies significantly over the surface due to differences in mineralogy, but it is also likely affected by the roughness and grain of the surface material. This variation will change the photoemission current from a

probe placed above the surface. Composition, roughness, and grain size all influence the emission factor from a surface as well, such that patches of the lunar surface that are covered with very fine material would be expected to photoemit at far lower levels than a rock composed of the same material. Whether a decrease in the photoemission from a surface is due to one of these effects, or if the surface composition of the surface just means that it has a naturally lower yield will be difficult to discern from standalone measurements. Additionally, it is common to find areas on the lunar surface that have different surface potentials and charge densities due to factors such as composition or illumination differences. We observe that these differences can create currents between the surfaces that significantly change the measured plasma potential.

Thus, utilizing Langmuir probe measurements, even over surfaces with unknown composition or with mixed mineralogy, for instance, is a useful approach to measuring charging and potential distributions above insulating surfaces, such as the dusty regoliths of the Moon and other airless planetary bodies. These probes nicely complement other instrument packages which are designed to measure surface material properties, but more laboratory work should be done to be able to accurately identify which properties influence the measurements.

Chapter 6

Summary and Future Work

6.1 Dust adhesion and surface modification

Dust has been identified as a significant hazard to future planetary surface exploration due to its jagged shape and tenacious adhesive properties, but little is known about the mechanisms of adhesion on widely varying surface types. Surface energy, roughness, mechanical properties and electronic properties are all known to contribute to the adhesion characteristics. In Chapter 2 we explored the effect of van der Waals and electrostatic forces to identify dominant components of the adhesive force and to determine if surface modification has a significant effect on those components.

Through collaboration with Ball Aerospace and Technologies Corporation (BATC), an ion beam process was used to modify (treat) the surfaces of three dramatically different materials spanning the range of conductor (black Kapton), semiconductor (silicon), and insulator (quartz). Adhesive forces between less than $25\ \mu\text{m}$ JSC-1 lunar simulants and these virgin/treated surfaces are measured in vacuum using a centrifugal force detachment method. By measuring the charges on JSC-1 grains that experience triboelectric charging on the surfaces, we were able to calculate the electrostatic forces between the two. We find that JSC-1 particles adhere less to treated silicon and quartz surfaces, correlated with a reduction in the van der Waals force due to a reduced surface energy. The large reduction in adhesion for treated black Kapton is mainly due to the large decrease in the electrostatic force that results from reduced contact charging. Surfaces that were also exposed to UV-radiation do not show the same beneficial results. Both virgin and treated quartz surfaces are most affected by the UV-irradiation, showing dramatically increased adhesion.

These promising results bode well for future exploration of dusty planetary bodies. Lunar dust is angular and therefore abrasive and may damage spacesuits and equipment. Dust it was found to adhere tenaciously to space suits and other materials during the Apollo missions (Gaier, 2005a), and in the future it may damage mechanical components, clog sensors, and degrade the performance of optical components placed on the lunar surface. It can also affect thermal optical properties such as absorptance and emittance and thus influence thermal radiation of instruments to space, possibly leading to dangerous increases in temperature (Gaier, 2009a). Some research is being done into the use of ‘active’ mitigation methods, typically by electrostatic mechanisms (for example, see (Calle et al., 2008)). However, these methods require power sources, and may be difficult to apply to complex surfaces. ‘Passive’ mitigation techniques such as this one, however, allow surface modification prior to a mission, do not require additional hardware, and can be applied to a wide variety of surfaces.

Many complex factors have an effect on adhesion forces, giving rise to difficulty in fully understanding the mechanisms of dust adhesion. Our experiments consistently show reduction in adhesion after surface modification, and theoretical estimates are in agreement with the experimental results. Continued analysis will focus on more complete characterization of surface properties (i.e. roughness, hardness, chemistry), evaluation of the long-term robustness of the surface modification, and the development and testing of the surface modification on a broader range of substrates. Some of the analysis techniques presented here have been replicated in a setup at Ball in order to continue testing. Additional simulants, such as LHT and JSC-Mars-1, silica, and alumina particulates with different surface characteristics will also be used to evaluate the changes in adhesive forces due to surface modification. These tests will allow us to more accurately predict how this surface modification will benefit future spacecraft missions, whether in orbit or on the surface of the Moon or another dusty planetary body.

6.2 Photoelectron Sheaths

We constructed an infrastructure inside of a large vacuum chamber to explore photoelectron sheaths created by ultraviolet illumination of surfaces in vacuum. In an initial set of experiments (Chapter 4), a large Zr surface is illuminated, creating a photoelectron sheath above the surface with a Debye shielding distance of ~ 7 centimeters, small in comparison to the diameter of the photoemitting surface. *This setup is unique due to the large volume of the photoelectron sheath, which enables Langmuir probe measurements above the surface.* The vertical extent of this sheath is such that a cylindrical Langmuir probe can be used to take data at many heights throughout the volume to observe the changes in the characteristics of the electron populations.

The emitting surface electrically floats to a potential approximately 1.5 V more positive than a nearby equipotential surface. Both a retarding potential analysis of the energy distribution of the electrons emitted from the electrically floating surface and Langmuir probe data measure an effective electron temperature of 1.4 (± 0.3) eV and a density of $4 \times 10^{10} \text{ m}^{-3}$. The electron densities measured throughout the sheaths by the Langmuir probe show good agreement with results from a 1-D PIC simulation. *The accuracies of both the measured potentials and derived densities indicate that measurements using similar Langmuir probes can be reliably applied above spacecraft and planetary surfaces.*

One interesting possible application of the Zr surface experiments is in interpretation of Cassini Langmuir probe data. Olson et al. (2010) have developed a useful new model to explain certain features of Cassini Langmuir probe data that accounts for the fact that the probe might be located within the sheath of the spacecraft. While this model is promising, the data also indicate that there is a strong photoemission feature (seen as the peak between 2.5–3.5 eV in Fig. 6.1b) that is acknowledged by the authors but not accounted for in their model. Similar sweep features have been observed in some of our Zr sheath experiments, so further analysis of this data will be useful for interpretation and modeling of the spacecraft data.

To study the photoelectron sheath above a surface that is more similar to the Moon or

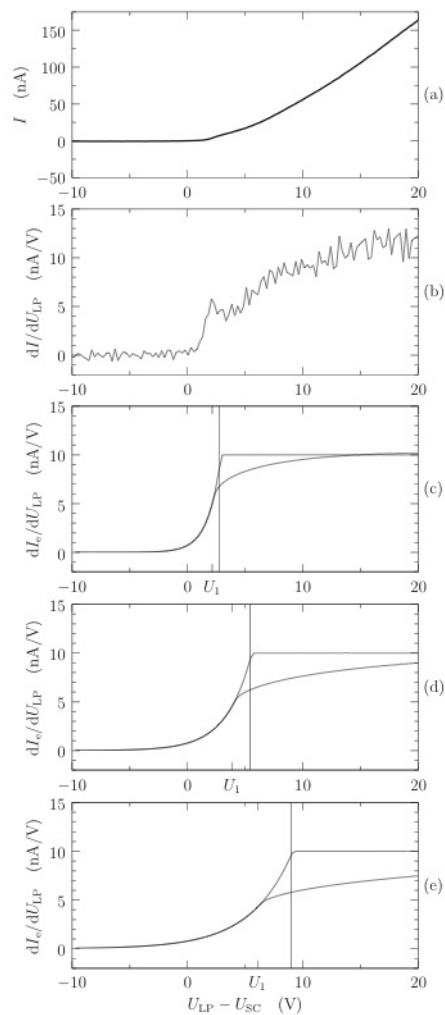


Figure 6.1: (a) A measured Cassini Langmuir probe sweep and (b) its derivative. The feature seen between 2.5–3.5 V is suggested to be due to photoelectrons, but the model fits shown in (c)–(e) are done without accounting for this feature. See Fig. 10 in Olson et al. (2010) for a full description of the parameters used for the models in (c)–(e).

any other such dusty planetary body, in the experiments presented in Chapter 5 a portion of the conducting Zr surface is covered with an insulating material. CeO_2 is used both in powdered and solid disk form, and unsieved JSC-1 is used to represent the lunar surface. We benefit from the use of a single-sided probe to measure the photoelectron populations above these surfaces and the Zr surface because the probe predominantly measures the photoelectrons from the surface that have upward motions (perpendicular to the surface).

Measurements taken above the CeO_2 surfaces are compared with those taken above the Zr surface to observe the differences in photoemission and determine how the insulating surface modifies the structure of the photoelectron sheath and the photoelectron characteristics. The densities above the surfaces are only found to have a modest dependence on the surrounding surface bias, and the plasma potentials measured above the insulating surfaces are significantly different than those above the Zr, due to the fact that the potential on the insulating materials is not set by the bias on the Zr surface, but by the equilibrium floating potential. We have shown that this floating potential is not fixed, however, and will adjust to balance the charging currents to and from the surrounding Zr surface.

None of these experiments are intended to exactly replicate the photoelectron sheaths above surfaces in space. Instead, they allow us to study the basic physical processes and how probes operate in these environments. *These measurements indicate that plasma probes placed on or around a planetary body can accurately determine potentials and densities above the surfaces – valuable information for understanding the charging environment of spacecraft and other objects.* As observed in Chapter 5, regions of differential charging will occur on surfaces. One obvious example is the lunar terminator region, but smaller patches can occur as well due to shadowing, surface composition, surface roughness, etc. In a different set of experiments, Wang et al. (2007b) explored the effect of “supercharging,” demonstrating that a moving lit-dark boundary will induce differential charging that builds up the surface potential over that expected from a stationary illumination source. An interesting follow-up to our experiments would be to explore similar lit/dark boundary conditions, utilizing Langmuir probe measurements above both insulating and conducting surfaces.

A logical continuation of the experiments that comprise this thesis will be to expand the scope to include additional features of the lunar environment and to address some of the questions raised by these experiments. Some possibilities for continued experimentation are briefly discussed here.

Composition Zirconium and cerium oxide are used in these experiments because of their desirable material characteristics for photoelectron sheath formation. Only JSC-1 is used for its relevance to planetary surfaces. An extended catalog of materials relevant to both planetary and spacecraft surfaces (these will be both insulators and conductors) should be evaluated for their UV reflectance and photoemission characteristics, to be used as a reference for future missions.

Surface roughness We have already observed that surface roughness plays a significant role in both the reflection of photons and emission of photoelectrons from surfaces exposed to UV illumination. A more controlled survey of the effect of surface roughness (for both insulators and conductors) would increase our understanding of UV albedo and photoemissive properties, and would again be useful for interpreting data from spacecraft or on a planetary surface.

Grain sizes Grain size distributions have an effect on surface roughness (due to size, packing efficiency, etc.), but grains also charge differently based on their sizes. The lunar soil has a fairly broad grain size distribution, but some size fractionation can occur on the Moon and other small bodies. Additionally, electrostatic levitation is likely size-dependent (Poppe and Horányi, 2010). We expect to see a strong difference over dust grains with narrow size distributions, and by studying specific size ranges, we can learn how they contribute to the bulk properties.

Ambient plasma Above the lunar surface (as well as spacecraft in space), the photoemission current is balanced by the solar wind. Experiments which include an ambient plasma plus photoelectrons are essential to explore the wide range of surface effects. While it is

relatively straightforward to add a plasma component in the chamber used for these studies, one difficulty will be to create a plasma of sufficiently low density so as not to completely overwhelm the photoelectron density.

Magnetic effects Small-scale magnetic anomalies have been observed on the lunar surface (Hood and Schubert, 1980), and some of these anomalies are associated with distinct surface albedo features. These are sometimes attributed to effects of dust charging and motion (see recent work by (Garrick-Bethell et al., 2011)). Some experiments have been conducted in which a small dipole is placed below a surface exposed to plasma (Wang et al., 2012), and we would like to measure the full effect of these in a simulated lunar environment by including both photoelectron and quasi-neutral plasmas.

The experiments presented in this thesis enable the better understanding of the photoelectron plasma environment surrounding spacecraft, the Moon and other airless bodies in the solar system. We have created a unique setup to explore some of the processes responsible for the charging, mobilization, and transport of dust particles on these surfaces, and have laid the groundwork for future studies, both in the laboratory and with spacecraft and planetary surface missions.

Bibliography

- M. M. Abbas, D. Tankosic, P. D. Craven, J. F. Spann, A. LeClair, and E. A. West. Lunar dust charging by photoelectric emissions. Planet. Space Sci., 55:953–965, 2007.
- J. H. Agui, P. Hambourger, J. Wirfs-Brock, J. N. Griffin, J. T. Hindall, and A. G. Morgan. Durable coating technology for lunar dust protection and mitigation. Technical Report 2006012205, NASA, 2006.
- N. Borisov and U. Mall. Charging and motion of dust grains near the terminator of the moon. Planet. Space Sci., 54:572–580, 2006.
- N. A. Burnham, D. D. Dominguez, R. L. Mowry, and R. J. Colton. Probing the surface forces of monolayer films with an atomic force microscope. Phys. Rev. Lett., 64:1931–1934, 1990.
- C. I. Calle, M. K. Mazumder, C. D. Immer, C. R. Buhler, J. S. Clements, P. Lundeen, A. Chen, and J. G. Mantovani. Controlled particle removal from surfaces by electrodynamic methods for terrestrial, lunar, and martian environmental conditions. J. Phys. Conf. Ser., 142(012073), 2008. doi: 10.1088/1742-6596/142/012073.
- M. H. Cho, C. Chan, N. Hershkowitz, and T. Intrator. Measurement of vacuum space potential by an emissive probe. Rev. Sci. Instrum., 55:631, 1984.
- P. Clark. An electrostatically based low power and mass tool for lunar dust removal. Presented at the Lunar Science Forum, NASA Ames, 2009.
- J. E. Colwell, S. Batiste, M. Horányi, S. Robertson, and S. Sture. Lunar surface: Dust dynamics and regolith mechanics. Rev. Geophys., 45:RG2006, 2007. doi: 10.1029/2005RG000184.
- M. Crowder and C. Haley. Mitigating molecular and particulate contamination via surface energy. In SPIE, volume 7069, pages 706909–706909–9, 2008.
- C. M. Cully, R. E. Ergun, and A. I. Eriksson. Electrostatic structure around spacecraft in tenuous plasma. J. Geophys. Res., 112:A09211, 2007. doi: 10.1029/2007JA12269.
- R. C. Davidson. Electrostatic shielding of a test charge in a non-neutral plasma. J. Plasma Phys., 6:229–235, 1971.
- B. V. Derjaguin, V. M. Muller, and Y. P. Toporov. Effect of contact deformation on adhesion of particles. J. Colloid Interface Sci., 53:314–326, 1975.

- D. Diebold, N. Herskowitz, A. D. Bailey, III, M. H. Cho, and T. Intrator. Emissive probe current bias method of measuring dc vacuum potential. Rev. Sci. Instrum., 59(2):270–275, 1988.
- A. Dove, M. Horányi, X. Wang, M. Piquette, A. Poppe, and S. Robertson. Experimental study of a photoelectron sheath. Phys. Plasmas, 19(043502), 2012. doi: 10.1063/1.3700170.
- Jr. E. C. Whipple. Theory of the spherically symmetric photoelectron sheath: A thick sheath approximation and comparison with the ats 6 observation of a potential barrier. J. Geophys. Res., 81:601–607, 1976. doi: 10.1029/JA081i004p00601.
- B. Feuerbacher, B. Fitton, and R. F. Willis, editors. Photoemission and the electronic properties of surfaces. John Wiley & Sons, 1978.
- V. E. Fortov, A. P. Nefedov, O. S. Vaulina, A. M. Lipaev, V. I. Molotkov, A. A. Samaryan, V. P. Niiikitskii, A. I. Ivanov, S. F. Savin, A. V. Kalmykov, A. Ya. Solov’ev, and P. V. Vinogradov. Dusty plasma induced by solar radiation under microgravitational conditions: an experiment on board the mir orbiting space station. J. Exp. and Theor. Physics, 87:1087 – 1097, 1998.
- J. W. Freeman and M. Ibrahim. Lunar electric fields, surface potential and associated plasma sheaths. The Moon, 14:103–114, 1975.
- J. H. M. Fu. Surface potential of a photoemitting plate. J. Geophys. Res., 76:2506–2509, 1971.
- B. Gady, R. Reifengerger, and D. S. Rimai. Contact electrification studies using atomic force microscope techniques. J. Appl. Phys., 84:319–322, 1998.
- J. R. Gaier. The effects of lunar dust on eva systems during the apollo missions. Technical Report 2005-213610, NASA, 2005a. URL available at <http://gltrs.grc.nasa.gov>.
- J. R. Gaier. Effect of illumination angle on the performance of dusted thermal control surfaces in a simulated lunar environment. Technical Report 2009-215647, NASA, 2009a. URL available at <http://gltrs.grc.nasa.gov>.
- J. R. Gaier. The effects of lunar dust on eva systems during the apollo missions. Technical Report 2005-213610, NASA, 2005b. URL available at <http://gltrs.grc.nasa.gov>.
- J. R. Gaier. Effect of illumination angle on the performance of dusted thermal control surfaces in a simulated lunar environment. Technical Report 2009-215647, NASA, 2009b. URL available at <http://gltrs.grc.nasa.gov>.
- I. Garrick-Bethell, J. W. Head III, and C. M. Pieters. Spectral properties, magnetic fields, and dust transport at lunar swirls. Icarus, 212:480–492, 2011.
- C. K. Goertz. Dusty plasmas in the solar system. Rev. Geophys., 27:271–292, 1989.
- M. Gotzinger and W. Peukert. Adhesion forces of spherical alumina particles on ceramic substrates. J. Adhes., 80:223–242, 2004.
- R. J. L. Grard. Properties of the photoelectron sheath derived from photoemission laboratory measurements. J. Geophys. Res., 78:2885–2906, 1973a. doi: 10.1029/JA078i016p02885.
- R. J. L. Grard, editor. Photon and Particle Interactions with surfaces in space, volume 37, 1973b. 6th ESLAB Symposium, Springer, New York.

- R. J. L. Grard. Solar photon interaction with the martian surface and related electrical and chemical phenomena. *Icarus*, 114:130–138, 1995.
- R. J. L. Grard and J. K. E. Tunaley. Photoelectron sheath near a planetary probe in interplanetary space. *J. Geophys. Res.*, 76:2498–2505, 1971. doi: 10.1029/JA076i010p02498.
- R. L. Guernsey and J. H. M. Fu. Potential distribution surrounding a photo-emitting plate in a dilute plasma. *J. Geophys. Res.*, 75:3193–3199, 1970.
- Jr. H. Mott-Smith and I. Langmuir. The theory of collectors in gaseous discharge. *Phys. Rev.*, 28: 727–763, 1926. doi: 10.1103/PhysRev.28.727.
- W. R. Harper. Contact and Frictional Electrification. Oxford: Clarendon Press, London, 1967.
- D. A. Hays. Adhesion of charged particles. *J. Adhes. Sci. Technol.*, 9:1063–1073, 1995.
- N. Hershkowitz. Plasma Diagnostics, Vol 1: Discharge Parameters and Chemistry, chapter 3. How Langmuir Probes Work, pages 113 – 183. Academic Press, Inc., San Diego, CA, 1989.
- H. E. Hinteregger, L. A. Hall, and G. Schmidtke. Space Research V, page 1175. North Holland, 1964.
- L. L. Hood and G. Schubert. Lunar magnetic anomalies and surface optical properties. *Science*, 208:49–51, 1980. doi: 10.1126/science.208.4439.49.
- M. Horanyi. Charged dust dynamics in the solar system. *Annu. Rev. Astron. Astrophys.*, 34: 383–418, 1996.
- M. Hyatt, P. Greenberg, V. Pines, A. Chait, W. Farrell, T. Stubbs, and J. Feighery. Lunar and martian dust: Evaluation and mitigation. In 45th AIAA Aerospace Sciences Meeting and Exhibit, Reno, NV, January 2007.
- C. Immer, J. Starnes, M. Michalenko, C.I. Calle, and M.K. Mazumder. Electrostatic screen for transport of martian and lunar regolith. In Lunar and Planetary Science XXXVII, number 2265, 2006.
- J. Israelachvili. Intermolecular and Surface Forces. Academic Press, New York, 1985.
- R. F. Kemp and Jr. J. M. Sellen. Plasma potential measurements by electron emissive probes. *Rev. Sci. Instrum.*, 37(4):455–461, 1966.
- J. P. Kremer, T. Sunn Pedersen, Q. Marksteiner, R. G. Lefrancois, and M. Hahn. Diagnosing pure-electron plasmas with internal particle flux probes. *Rev. Sci. Inst.*, 78:013503, 2007. doi: Add data for field: Doi.
- D. Y. Kwok and A.W. Neumann. Contact angle interpretation in terms of solid surface tension. *Colloids Surf., A*, 161:31–48, 2000.
- Q. Li, V. Rudolph, and W. Peukert. London-van der waals adhesiveness of rough particles. *Powder Technol.*, 161:248–255, 2006.
- S. F. Lin, D. T. Pierce, and W. E. Spicer. Photoemission studies of platinum. *Phys. Rev. B*, 4: 326–329, 1971. doi: 10.1103/PhysRevB.4.326.

- N. L. S. Martin and A. von Engel. The reflection of slow electrons from a soot-covered surface. J. Phys. D, 10:863–868, 1977.
- D. S. McKay, J. L. Carter, W. W. Boles, C. C. Allen, and J. H. Allton. Jsc-1: A new lunar soil simulant. In Engineering, Construction, and Operations in Space IV, pages 857–866. American Society of Civil Engineers, 1994.
- D. A. Mendis and M. Rosenberg. Cosmic dusty plasma. Annu. Rev. Astron. Astrophys., 32:419–463, 1994.
- R. L. Merlino. Understanding langmuir probe current-voltage characteristics. Am. J. Phys., 75(12):1078–1085, 2007.
- H. B. J. Michaelson. The work function of the elements and its periodicity. J. App. Phys., 48:4729–4733, 1977. doi: 10.1063/1.323539.
- H. Mizes, M. Ott, E. Eklund, and D. Hays. Small particle adhesion: measurement and control. Colloids Surf., A, 165:11–23, 2000.
- M. E. Mullins, L. P. Michaels, V. Menon, B. Locke, and M. B. Ranade. Effect of geometry on particle adhesion. Aerosol Sci. Technol., 17:105–118, 1992.
- T. Nitter, T. Aslaksen, F. Melandso, and O. Havnes. Levitation and dynamics of a collection of dust particles in a fully ionized plasma sheath. IEEE Trans. Plasma Sci., 22:159–172, 1994.
- T. Nitter, O. Havnes, and F. Melandso. Levitation and dynamics of charged dust in the photoelectron sheath above surfaces in space. J. Geophys. Res., 103:6605–6620, 1998.
- C. Olsen. The hidden ion population of the magnetosphere. J. Geophys. Res., 87(A5):3481–3488, 1982. doi: 10.1029/JA087iA05p03481.
- J. Olson, N. Brenning, J.-E. Wahlund, and H. Gunell. On the interpretation of langmuir probe data inside a spacecraft sheath. Rev. Sci. Instrum., 81(105106), 2010. doi: 10.1063/1.3482155.
- XERADEX lamp manual. OSRAM SYLVANIA, Inc., Danvers, MA, version 1.5 edition, Nov 2009. URL www.sylvania.com.
- M. A. Pelizzari and D. R. Criswell. Differential photoelectric charging of nonconducting surfaces in space. J. Geophys. Res., 83:5233–5244, 1978.
- W. Peters. <http://www.sciencedaily.com/releases/2009/09/090923112547.htm>, 2009. URL <http://www.sciencedaily.com/releases/2009/09/090923112547.htm>.
- A. Poppe and M. Horányi. Simulations of the photoelectron sheath and dust levitation on the lunar surface. J. Geophys. Res., 115:A08106, 2010. doi: 10.1029/2010JA015286.
- Y.I. Rabinovich, J.J. Adler, A. Ata, R.K. Singh, and B.M. Moudgil. Adhesion between nanoscale rough surfaces: I. role of asperity geometry. J. Colloid Interface Sci., 232:10–16, 2000.
- D. L. Reasoner and W. J. Burke. Measurement of the lunar photoelectron layer in the geomagnetic tail. In R. J. L. Grard, editor, Photon and Particle Interactions with Surfaces in Space, volume 37 of Astrophysics and Space Science Library, pages 369–387, 1973.

- J. J. Rennilson and D. R. Criswell. Surveyor observations of lunar horizon-glow. The Moon, 10: 121–142, 1974.
- S. Robertson, Z. Sternovsky, and B. Walch. Reduction of asymmetry transport in the annular penning trap. Phys. Plasma, 11:1753–1756, 2004. doi: 10.1063/1.1688337.
- G. R. Salazar-Banda, M. A. Felicetti, J. A. S. Gonçalves, J. R. Coury, and M. L. Aguiar. Determination of the adhesion force between particles and a flat surface, using the centrifuge technique. Powder Technol., 173:107–117, 2007.
- H. Schröder. Spherically symmetric model of the photoelectron sheath for moderately large plasma debye lengths. In R. J. L. Grard, editor, Photon and Particle Interactions with Surfaces in Space, volume 37 of Astrophysics and Space Science Library, pages 51–58, 1973.
- E. E. Scime, J. L. Phillips, and S. J. Bame. Effects of spacecraft potential on the three-dimensional electron measurements of the solar wind. J. Geophys. Res., 99(A8):14769–14776, 1994.
- J. D. Scudder, X. Cao, and F. S. Mozer. Photoemission current-spacecraft voltage relation: Key to routine, quantitative low-energy plasma measurements. J. Geophys. Res., 105(A9):21281–21294, 2000.
- A. A. Sickafoose, J. E. Colwell, M. Horányi, and S. Robertson. Photoelectric charging of dust particles in vacuum. Phys. Rev. Lett., 84:6034–6037, 2000. doi: 10.1103/PhysRevLett.84.6034.
- A. A. Sickafoose, J. E. Colwell, M. Horányi, and S. Robertson. Experimental investigations on photoelectric and triboelectric charging of dust. J. Geophys. Res., 106:8343–8356, 2001. doi: 10.1029/2000JA000364.
- A. A. Sickafoose, J. E. Colwell, M. Horanyi, and S. Robertson. Experimental levitation of dust grains in a plasma sheath. J. Geophys. Res., 107(A1110408), 2002. doi: 10.1029/2002JA009347.
- S. F. Singer and E. H. Walker. Photoelectric screening of bodies in interplanetary space. Icarus, 1: 7–12, 1962. doi: 10.1016/0019-1035(62)90004-0.
- J. R. Smith, N. Hershkowitz, and P. Coakley. Inflection-point method of interpreting emissive probe characteristics. Rev. Sci. Instrum., 50(2):210–218, 1979.
- J. J. Sojka, G. L. Wrenn, and J. F. E. Johnson. Pitch angle properties of magnetospheric thermal protons and satellite sheath interference in their observation. J. Geophys. Res., 89:9801–9811, 1984. doi: 10.1029/JA089iA11p09801.
- Z. Sternovsky, M. Horányi, and Scott Robertson. Charging of dust particles on surfaces. J. Vac. Sci. Technol., A, 19, 2001.
- Z. Sternovsky, S. Robertson, A. A. Sickafoose, J. Colwell, and M. Horányi. Contact charging of lunar and martian dust simulants. J. Geophys. Res., 107(E11), 2002. doi: 10.1029/2002JE001897.
- Z. Sternovsky, P. Chamberlin, M. Horányi, S. Robertson, and X. Wang. Variability of the lunar photoelectron sheath and dust mobility due to solar activity. J. Geophys. Res., 113(A12):A10104, 2008. doi: 10.1029/2008JA013487.
- T. J. Stubbs, R. R. Vondrak, and W. M. Farrell. A dynamic fountain model for lunar dust. Adv. Sp. Res., 37:59–66, 2006.

- S. Szita, A. N. Fazakerley, P. J. Carter, A. M. James, P. Trávníček, G. Watson, M. André, and K. Torkar. Cluster peace observations of electrons of spacecraft origin. Ann. Geophys., 19: 1721–1730, 2001. doi: 10.5194/angeo-19-1721-2001.
- L. Tonks and I. Langmuir. A general theory of the plasma of an arc. Phys. Rev., 34:876–922, 1929. doi: 10.1103/PhysRev.34.876.
- J. K. E. Tunaley and J. Jones. The photoelectron sheath around a spherical body. In R. J. L. Grard, editor, Photon and Particle Interactions with surfaces in space, volume 37 of Astrophysics and Space Science Library, page 59, 1973.
- E. Walbridge. Lunar photoelectron layer. J. Geophys. Res., 78:3668–3687, 1973. doi: 10.1029/JA078i019p03668.
- O. R. Walton. Adhesion of lunar dust. Technical Report 2007-214685, NASA, 2007. URL <http://gltrs.grc.nasa.gov/reports/2007/CR-2007-214685.pdf>.
- O. R. Walton. Ranking adhesion forces for charged lunar dust particles on conducting surfaces. In ASCE Conf. Proc., volume 323, pages 22–36, 2008.
- X. Wang, J. Colwell, M. Horányi, and S. Robertson. Charge of dust on surfaces in plasma. IEEE Trans. Plasma Sci., 35:2–10, 2007a.
- X. Wang, M. Horányi, Z. Sternovsky, S. Robertson, and G. E. Morfill. A laboratory model of the lunar surface potential near boundaries between sunlit and shadowed regions. Geophys. Res. Lett., 34:L16104, 2007b. doi: 10.1029/2007GL030766.
- X. Wang, M. Horányi, and S. Robertson. Plasma probes for the lunar surface. J. Geophys. Res., 113:A08108, 2008. doi: 10.1029/2008JA013187.
- X. Wang, M. Horanyi, and S. Robertson. Experiments on dust transport in plasma to investigate the origin of the lunar horizon glow. J. Geophys. Res., 114(A05103), 2009. doi: 10.1029/2008JA013983.
- X. Wang, M. Horányi, and S. Robertson. Investigation of dust transport on the lunar surface in a laboratory plasma with an electron beam. J. Geophys. Res., 115(A11102), 2010.
- X. Wang, M. Horanyi, and S. Robertson. Characteristics of a plasma sheath in a magnetic dipole field: implications to the solar wind interaction with the lunar magnetic anomalies. in prep, 2012.
- E.C Whipple. Potentials of surfaces in space. Rep. Prog. Phys., 44:1197–1250, 1981.
- R. F. Willis, M. Anderegg, B. Feuerbacher, and B. Fitton. Photoemission and secondary electron emission from lunar surface material. In R. J. L. Grard, editor, Photon and Particle Interactions with Surfaces in Space, volume 37 of Astrophysics and Space Science Library, pages 51–58, 1973.
- A. D Zimon. Adhesion of Dust and Powder. Plenum, New York, 1969.

Appendix A

Additional diagnostic techniques and troubleshooting

Early measurements of the current balance to the Zr surface revealed a population of electrons in the chamber that were from sources other than the Zr itself, as described in Section 3.3. These “excess electrons” are generated by the UV photons incident every surface within the vacuum chamber. Because the surface area of all of these surfaces (chamber walls, linear rails, etc.) is much larger than that of the Zr surface, the current contribution of these excess electrons dominated the signal in the Langmuir probe sweeps. Several techniques were implemented in an attempt to reduce this excess electron population in order to measure a cleaner signal from the surface.

A.1 Characterizing the photoelectron gas

First, we needed to understand the populations of electrons produced by the chamber walls. A 2-inch diameter spherical probe was constructed to measure the electron energy distribution of the photoelectron gas throughout the chamber. Druyvesteyn (1930) first demonstrated that the electron distribution function could be determined from the second derivative of the Langmuir probe characteristics, and we use the spherical probe to measure this distribution. The spherical shape and large size were ideal for collecting the electron population and understanding the velocity distribution of electrons impacting the probe. The probe was inserted into the chamber on a linear feedthrough on one side of the chamber, such that the probe could be moved perpendicularly to the wall of the chamber, and measurements were taken both in the center of the chamber and closer to the walls.

Using the Langmuir probe circuitry and the spherical probe, we swept the probe from -60 V to +30 V. Our first sweeps were very noisy, making it almost impossible to learn anything from the second derivative. In order to decrease the noise, we increased averaging during the sweeps, and averaged over 5 successive sweeps. The probe was placed near the center of the vacuum chamber (x-y centered, about 20 cm from the lamps) and then moved to a few centimeters from the wall in order to analyze the effect of the population of wall electrons on the electron distribution. Both spherical probe sweeps are shown in Fig. A.1.

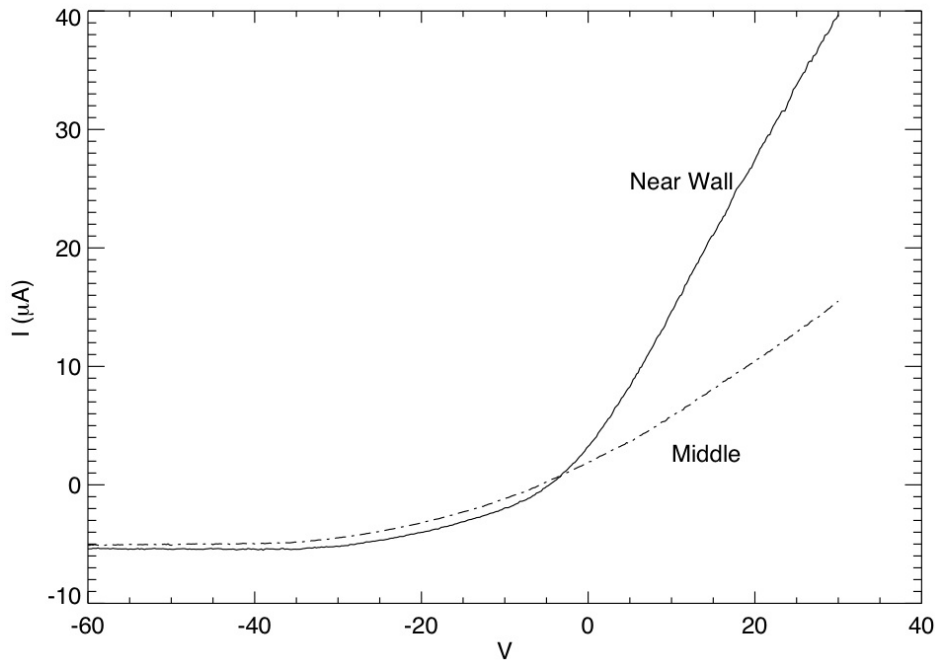


Figure A.1: Spherical probe sweeps at two measurement locations, a few centimeters from the wall and in the center of the chamber (radially).

We used a Savitzky-Golay fitting technique to smooth the probe sweeps while finding the second derivative. In Fig. A.2 the sweeps are smoothed over 20, 30, 40, 50, 60, 70, and 80 data points to produce the second derivative curves. The second derivative of the wall sweep shows an obvious and pronounced peak in the distribution function, with a maximum around -1.5 V. There is also a higher energy tail of the peak around -30 V (the ends of the derivatives are lost due to avoidance of edge effects in the smoothing). However, the second derivative of the sweep from the

center of the chamber is much less clear, and seems to have multiple peaks (although this might also be a side effect of the noise).

The work function of stainless steel is ~ 4.5 eV, and the peak emission from the UV lamps is at 7.2 eV, so we would expect electrons emitted from the walls to have energies on the order of 2.5 eV. This is similar to the peak in the wall sweep distribution. The FWHM of the peak in the wall distribution is about 20 V. A single Gaussian fit to the peak has a mean of -1.6 V with a standard deviation of 6.1 V (red line in Fig. A.2(c)), and a linear combination of two Gaussian peak fits has peak means at -1.5 V and -27.7 V (blue line in Fig. A.2(c)).

A.2 Techniques to reduce the excess electron population

A.2.1 Diagnostics with a grid

Secondary measurements were taken using a version of the biased grid with a wider total radius and greater grid area. Comparing the two cases in which the grid was 3" above the table (Fig. A.3(a)), the Zr surface emitted about twice as much as in the previous grid setup, and collection was somewhat reduced. However, in the case in which the grid was 9" above the table (Fig. A.3(b)), emission was again increased, but the collection was significantly above the levels of the previous grid. This is due to the greater percentage of light that is transmitted through the grid and is thus incident on the walls between the grid and the surface when the grid is so far above the table.

A.2.2 Using a magnetic field to reduce the excess electron population

If the electrons emitted by the wall are confined to small region close to the walls, that electron population would not significantly contribute to the experimental measurements. In order to create this confinement effect with a magnetic field, we constructed two Helmholtz coils with radius $R = 0.5$ m around the chamber. Each coil had 22 turns, and between 0-40 (55 max rated) Amps of current could be passed through the wires. To determine the resulting electric field, we

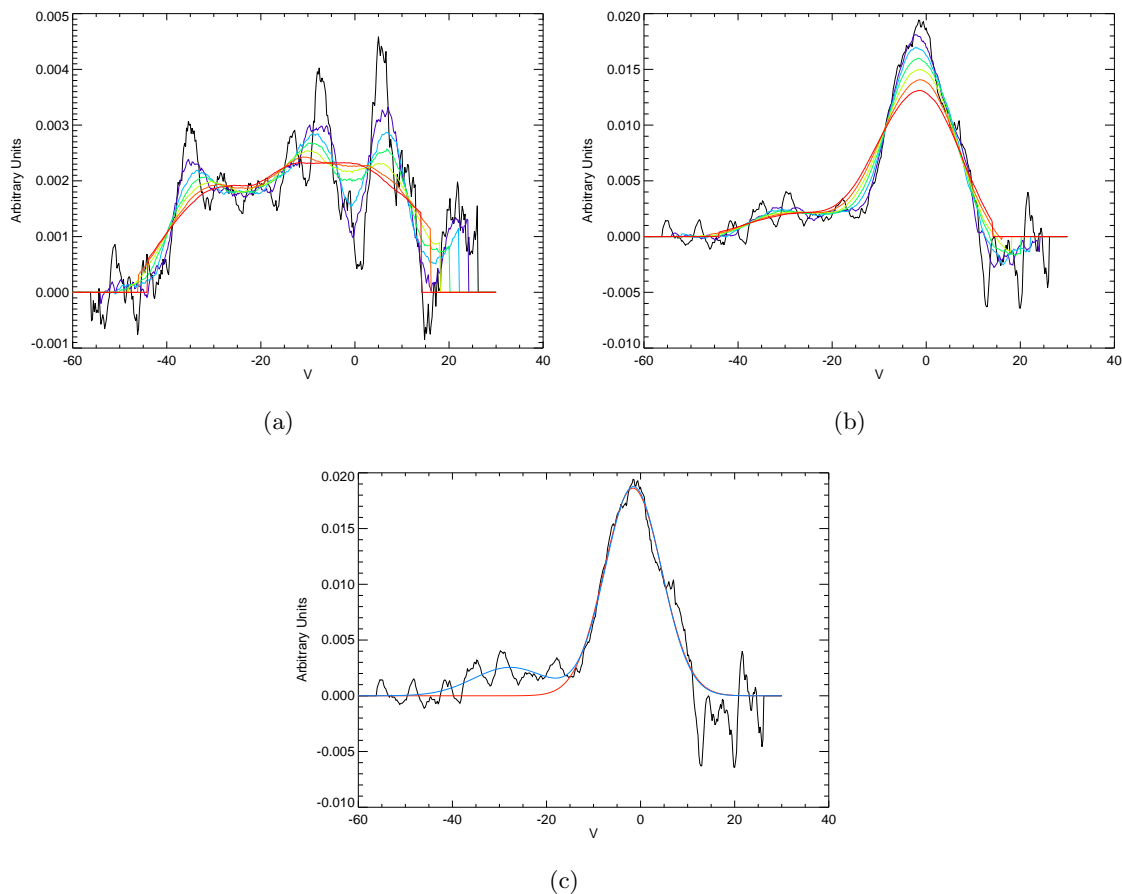
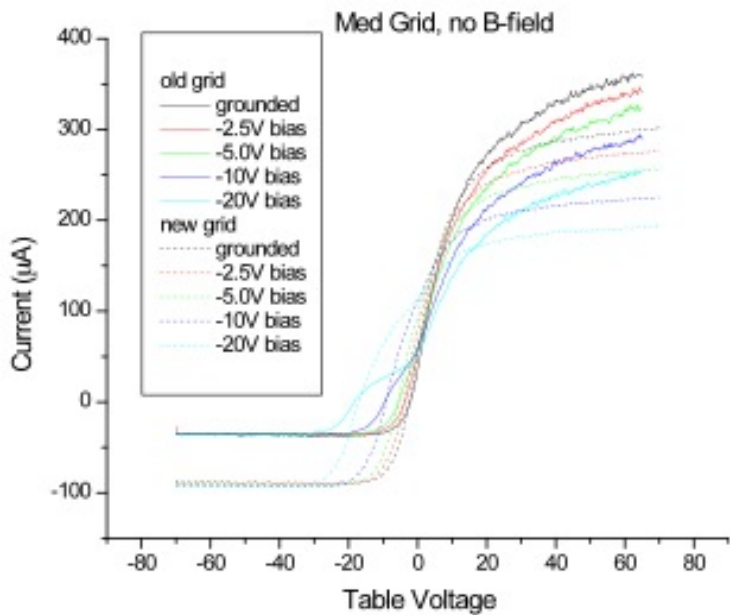
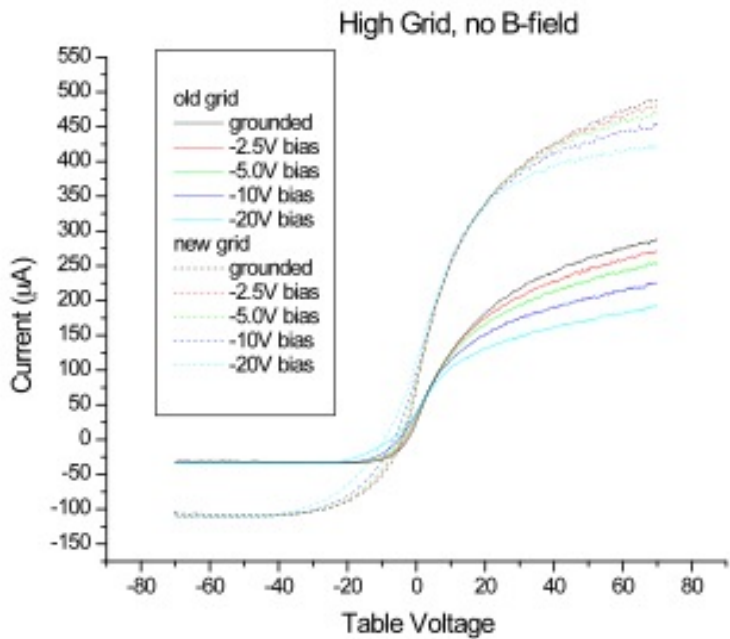


Figure A.2: Second derivatives of the sweeps shown in Fig. A.1, for (a) the center of the chamber and (b) near the wall. The derivatives are shown smoothed over an increasing number of points to determine the effect of trends compared to noise. Sweeps are smoothed over 20 (black), 30 (purple), 40 (blue), 50 (green), 60 (yellow), 70 (orange) and 80 (red) points. (c) Gaussian least-squares fits to the (20-point smoothed) second derivative of the near-wall probe sweep. A single Gaussian fit is shown in red, and the blue line is the fit of the sum of two Gaussians; both fits are described in the text.



(a)



(b)

Figure A.3: Characteristic $I - V$ probe traces using the Zr surface as a Langmuir probe, with the grid over the table biased to the voltages shown. In these plots, two grids (old and new versions) are compared at two different heights: (a) 3" above the surface and (b) 9" above the surface.

use the equation for the magnetic field of a Helmholtz coil

$$B = \left(\frac{4}{5}\right)^{3/2} \frac{\mu_0 N I}{R}, \quad (\text{A.1})$$

where μ_0 is the permeability of free space, N is the number of turns per coil, and I is the current passing through the coils. From this, we determined the gyroradius of an electron interacting with the magnetic field lines,

$$r_L = \frac{m_e v}{|q| B}, \quad (\text{A.2})$$

where $v = \sqrt{2qE/m}$, with the electron energy, E , in eV. For our experiments, if we used a current $I = 20$ A (40 A), then $B = 7.9 \times 10^{-4}$ T (1.58×10^{-3} T) and $r_L = 6.0$ mm (3.0 mm).

As shown in Fig. A.4(a), we saw an interesting effect created by the magnetic field. Unfortunately, it did not seem to reduce the excess collection of wall emission. In fact, both emission and collection currents increased in the presence of a magnetic field (and we also saw a corresponding rise in the chamber pressure measurement when the magnetic field was generated). With 10 A current running through the Helmholtz coils, the emission current was approximately doubled from the nominal case of no magnetic field. Increasing the current to 20 A created another doubling, with the resulting emission current almost four times the nominal case. However, increasing the current to 40 A, we saw a decrease in the emission current. In all cases, both emission and collection currents either increased or decreased. The B-field might have inhibited collection by confining the electrons, as there did seem to be some reduction in the collected current for the larger magnetic field cases. The ratio of collected to emitted current was closest to 1:1 in the 20 A case. Of note, we also saw a difference in the magnitude of the emitted and collected currents if the magnetic field was pointing up or down (Fig. A.5). We have concluded that the magnetic field was affecting the plasma generated in the Xeradex lamps, as well as that in the rest of the chamber.

A.2.3 Combination of the biased grid and magnetic fields

With an idea of how the magnetic field affected emission and collection in the chamber, we repeated the sweeps of the Zr table with a grid between the chamber and the lamps with the

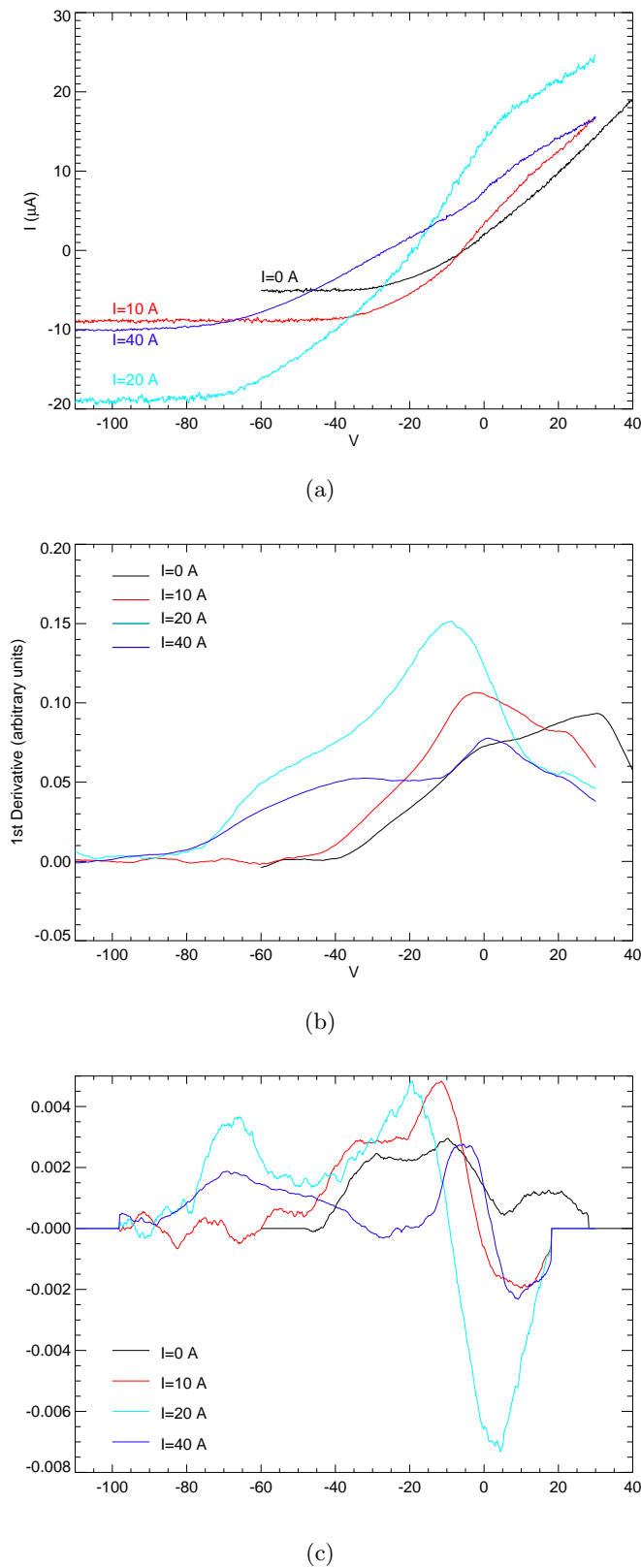


Figure A.4: (a) $I - V$ sweeps from the spherical probe at the center of the chamber in the presence of magnetic fields generated by running $I=0, 10, 20$ and 40 A through the Helmholtz coils around the chamber. (b) First derivatives of the sweeps shown in (a), with the sweeps smoothed over 50 points. (c) Second derivatives of the sweeps shown in (a), smoothed by 60 points.

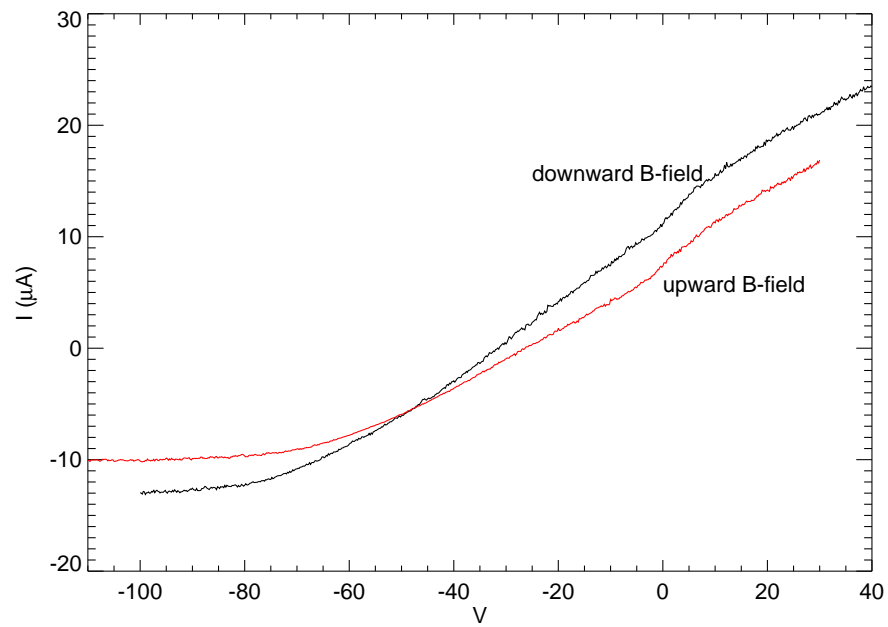
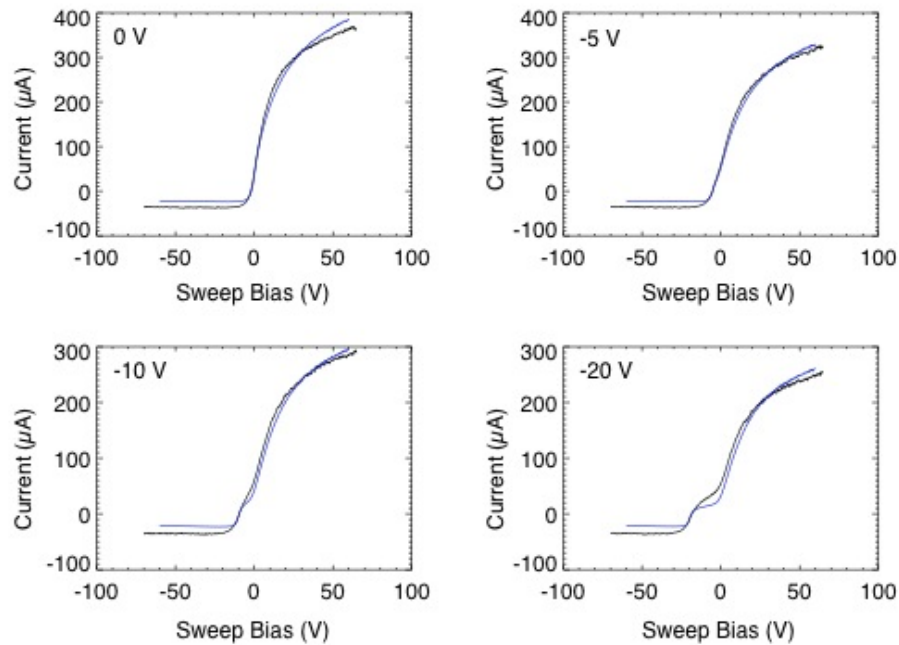


Figure A.5: Spherical probe sweeps in the presence of a magnetic field created by 40 A current running through the Helmholtz coil loops for the case of an upward- and downward-directed magnetic field (the upward-directed magnetic field curve is the same as the blue line in Fig. A.4(a)).

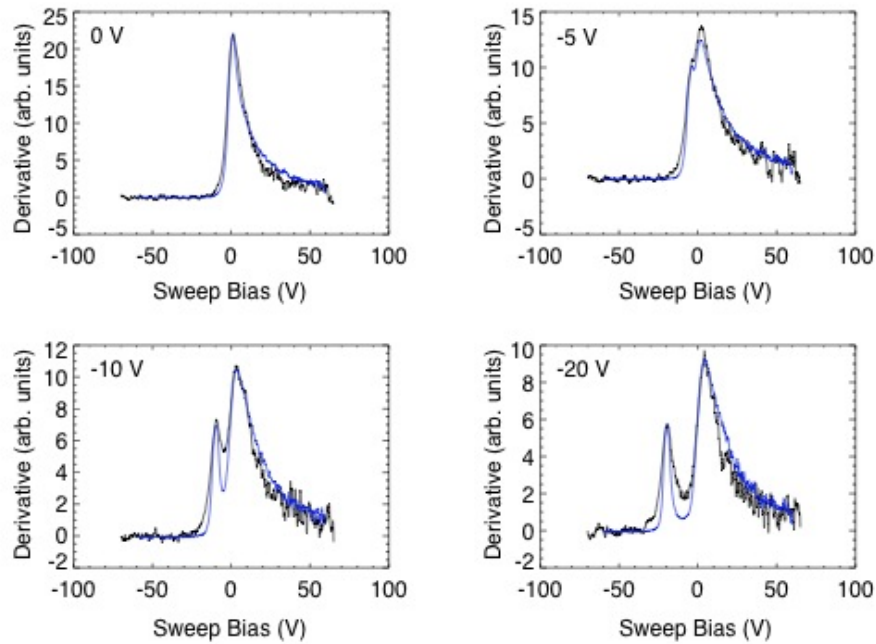
addition of the magnetic field component. As seen in Fig. A.6, the grid was supported by insulating standoffs that placed it 7.6 cm above the Zr table. Sweeps were performed on the Zr table with when the grid was biased to 0 V, -2.5 V, -5 V, -10 V, or -20 V, for each case of no magnetic field, or a magnetic field created by 10, 20, or 40 A current through the Helmholtz coils.

To check for consistency, we first compared these results to previous data taken when the grid was closer to the table. Figure A.6(a) shows a comparison of the control case from this experiment with the previous Zr table sweeps. The general characteristics of the curves are the same, with identical peaks in the derivatives (Fig. A.6(b)). There is some difference in the total emission in all cases, which could be due to the increased distance between the grid and the table, or because there were different lamps in the chamber (we replaced one of the lamps, which was problematic and had inconsistent emission). Additionally, even though both sets of sweeps were smoothed by the same amount, the new sweeps appeared much noisier than the old sweeps (perhaps due to the cleanliness of the surface).

Sweeps of the Zr table are plotted in Fig. A.7 for the cases of the biased grid. When the magnetic field is turned on with 10 A current, we saw that the emission current increased while the collected current decreased (which indicates that the signal is increasingly from the table, not from excess electrons), and the shape of the curve changes slightly. When the magnetic field was increased (20 A current through the coils), we again saw that the emission current increased and the collected current decreased, and there was also a flattening of the curve in the collection region. While the emission current decreased when the magnetic field was again increased to 40 A current through the coils, the collected current shows a significant decrease as well, and appears to be even flatter in the right hand side of the curve than the previous case. These results are summarized in Table A.1, which shows the ratio of collection to emission for each case. Additional evidence for the effectiveness of the combined grid and magnetic field is shown in Fig. A.8, where we have plotted the derivatives of the curves shown in Fig. A.7. When the grid is grounded, the derivative is clearly peaked around 0 V, and even with a -5 V bias on the grid, only a slight shift is seen in this distribution. However, in Fig. A.8(d), we see that when the grid is biased to -20 V, and the



(a)



(b)

Figure A.6: (a) Comparison of current grid sweeps with grid 7.6 cm above the surface with sweeps from the same grid at a lower height (~ 3 cm). All sweeps are taken without the presence of a magnetic field, and the grid biases are shown for each case. (b) Derivatives of the sweeps show in (a).

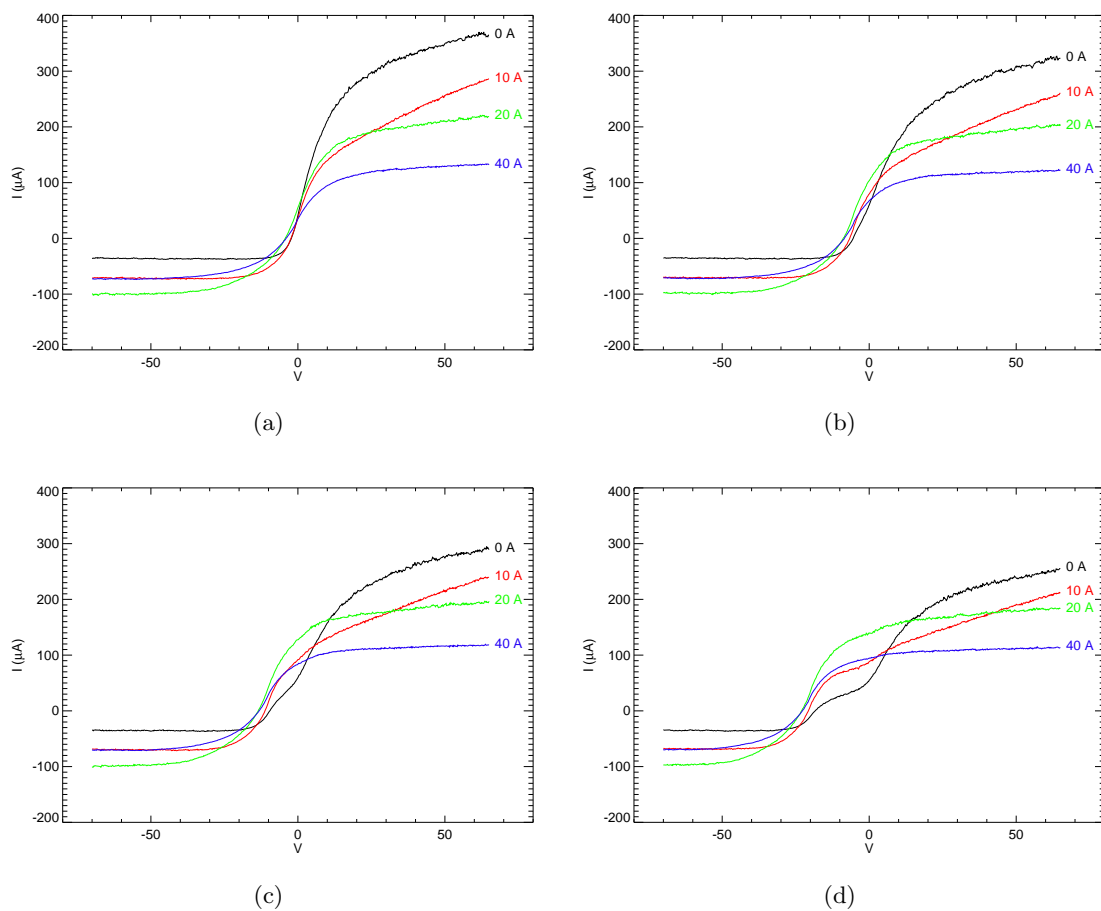


Figure A.7: Characteristic $I - V$ curves for the Zr table for the cases of the grid biased to (a) 0 V, (b) 5 V, (c) -10 V, and (d) -20 V. For each case, the effects of changing the magnetic field generated by Helmholtz coils with 0-40 A is shown.

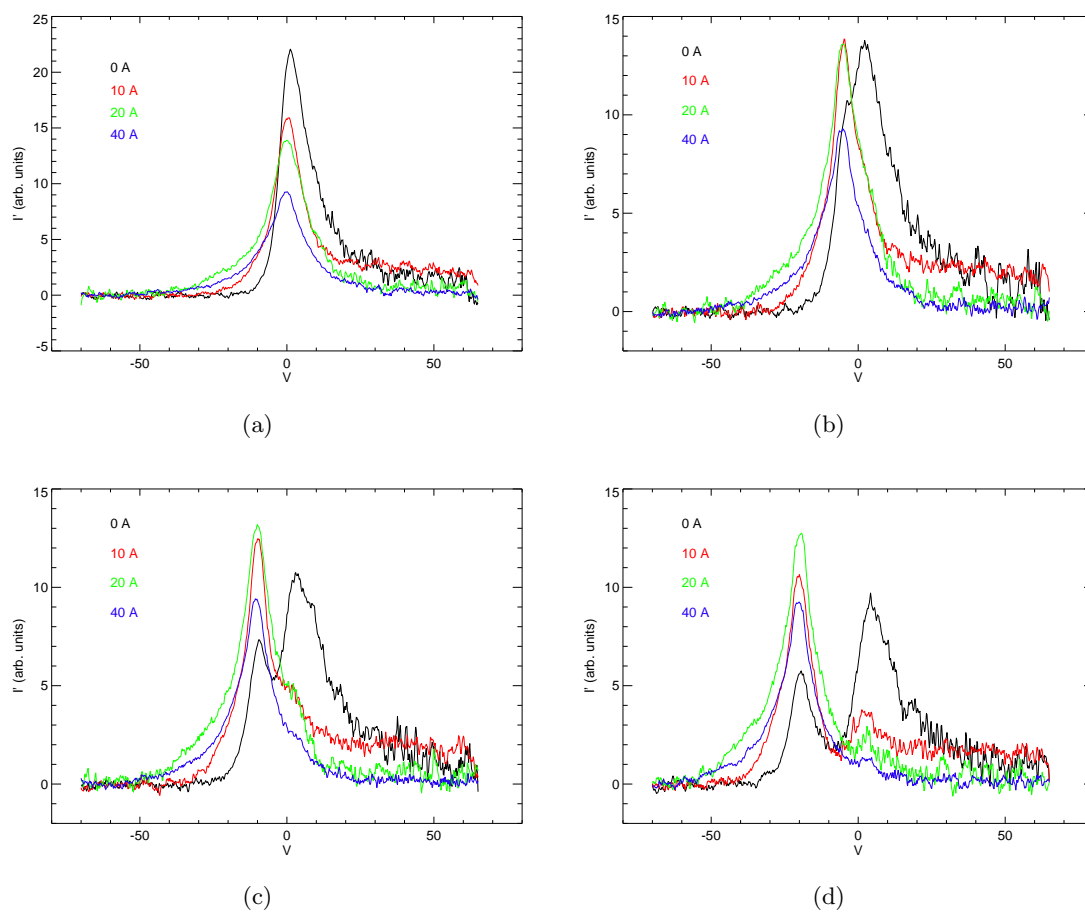


Figure A.8: Derivatives of the Zr surface sweeps shown in Fig. A.7 for the cases of the grid biased to (a) 0 V, (b) -5 V, (c) -10 V, and (d) -20 V.

Table A.1: Ratio of collection to emission current on the Zr table as a function of the current in the magnetic coils and the grid bias.

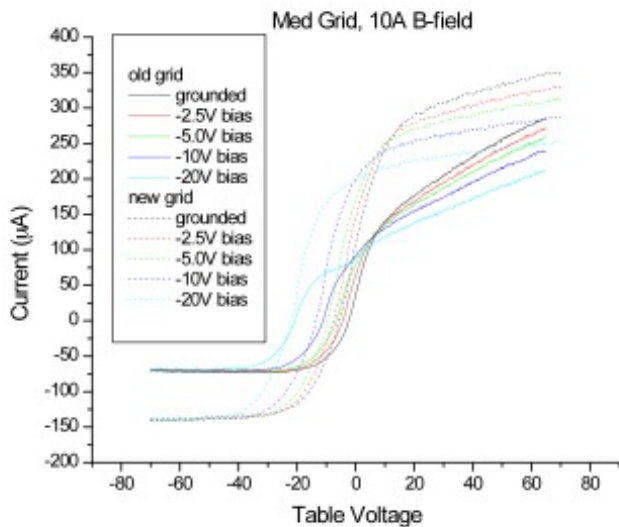
Current	Grid Bias				
	Ground	-2.5 V	-5 V	-10 V	-20 V
0 A	10	9.6	9.1	8.2	7.1
10 A	3.9	3.7	3.5	3.4	3.0
20 A	2.2	2.1	2.0	2.0	1.9
30 A	1.8	1.7	1.7	1.6	1.6

Helmholtz coils have 40 A current, there is almost no peak in the derivative around 0 V. The peak is, in fact, significantly reduced even by the magnetic field generated by 10 or 20 A current in the Helmholtz coils. For reference, the peaks of the derivatives are listed in Table A.2.

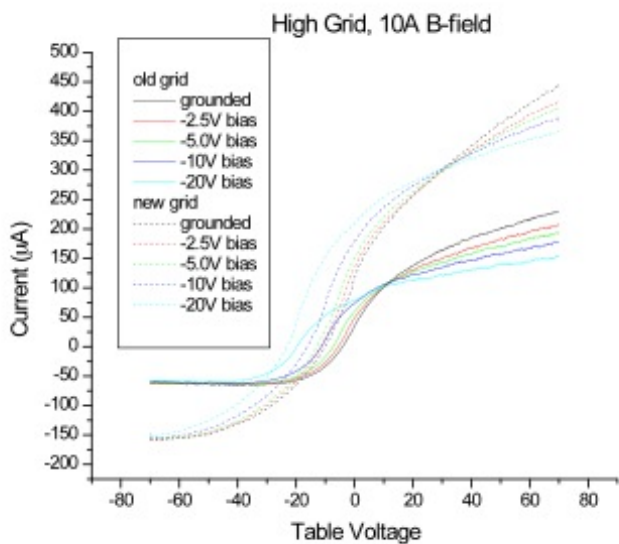
We followed up these measurements with the second version of the grid to determine if this would produce any further reduction in the amount of electrons collected by the Zr surface. Unfortunately, we did not observe a significant improvement. A significant increase in emission from the Zr surface was observed, as in the case of the measurements without a magnetic field (see the left side of the curves in Fig. A.9). The curves were still dominated by electron collection (see the right side of the curves in Fig. A.9), although there did seem to be more confinement of the electrons in these cases (the curves are flatter toward the right side of the graph than in the case of the old grid).

A.3 Results of troubleshooting

Several techniques were used in an attempt to reduce the population of excess electrons in the measurement space above the Zr surface. In the end, it was decided that the magnetic field created more complications in the interpretation of the signal, and thus would not be used for the remainder of the experiments. The final grid design implemented has a total washer outer diameter only slightly smaller than the interior dimension of the chamber, an inner diameter calculated to shade the walls below the grid from direct UV light, and a nickel mesh grid.



(a)



(b)

Figure A.9: Characteristic $I - V$ probe traces using the Zr surface as a Langmuir probe, with the grid over the table biased to the voltages shown. In these plots, the magnetic field is generated by 10 A current in the Helmholtz coils, and two grids (old and new versions) are compared at two different heights: (a) 3" above the surface and (b) 9" above the surface.

Table A.2: Voltage at the peak of the derivative of the (20-point smoothed) Zr table sweeps as a function of the current in the magnetic coils and the grid bias.

Current	Grid Bias				
	Ground	-2.5 V	-5 V	-10 V	-20 V
0 A	+1.2	+1.2	+2.2	+3.0 (-10.0)	+4.2 (-19.4)
10 A	+0.8	-2.2	-4.8	-9.8	-20.0
20 A	0.0	-3.0	-5.2	-10.0	-19.2
30 A	0.0	-3.2	-5.2	-10.6	-20.0

Appendix B

Paper and presentations

B.1 Published papers

A. Dove, M. Horányi, X. Wang, M. Piquette, A. R. Poppe, and S. Robertson. (2012) Experimental study of a photoelectron sheath, *Physics of Plasmas*, 19, 043502.

A. Dove, J. Heldmann, C. McKay, and O. B. Toon. (2012) Physics of thick seasonal snow-pack with applications for snow algae, *Arctic, Antarctic, and Alpine Research*, 44, 36-49.

A. Dove, S. Robertson, M. Horányi, A. Poppe, X. Wang. (2011) Operation of a Langmuir probe in a photoelectron plasma, *AIP Conf. Proc.* 1397, 387-388.

A. Dove, G. Devaud, X. Wang, M. Crowder, A. Lawitzke, and C. Haley. (2011) Mitigation of lunar dust adhesion by surface modification, *Planetary and Space Science*, 59, 1784-1790.

M. Crowder, R. Stover, A. Lawitzke, G. Devaud, **A. Dove**, and X. Wang. (2010) Reducing particle adhesion by material surface engineering, *Proc. SPIE* 7794, 77940G.

B.2 Papers in preparation

A. Dove, M. Horányi, X. Wang, and S. Robertson. Effects of surface material properties on photoelectron sheath characteristics.

A. Dove and M. Horányi. Charged up: Faraday cup measurements of dust lofted by lunar rover motion.

B.3 Selected Presentations

A. Dove, Experimental investigations of lunar plasma and dust dynamics, CIPS Seminar, University of Colorado, Boulder, CO (4/12)

A. Dove, Experimental investigations of lunar plasma and dust dynamics, Lunar and Planetary Institute, Houston, TX (4/12)

A. Dove, Experimental investigations of lunar plasma and dust dynamics, Planetary Science seminar, University of Central Florida, Orlando, FL (3/12)

A. Dove, X. Wang, S. H. Robertson, A. Poppe, M. Horányi, Laboratory simulations of photoelectron sheaths, AGU, San Francisco, CA (12/11)

A. Dove, A. Poppe, A. Fagan, C. Neish, H. Fuqua, G. Kramer, and M. Horányi, LunGradCon: The Lunar Graduate Conference, AGU, San Francisco, CA (12/11)

A. Dove, X. Wang, M. Horányi, Z. Sternovsky, A. Poppe, S. Robertson, Laboratory measurements of photoelectron plasmas, 4th NASA Lunar Science Forum, NASA Ames Research Center, (7/11)

A. Dove, M. Horányi, J. Minafra, Charge measurements of dust grains lofted by lunar rovers, 4th NASA Lunar Science Forum, NASA Ames Research Center (7/11)

A. Dove LunGradCon 2011 Overview presentation: Science FROM the Moon, 2nd Annual LunGradCon, NASA Ames Research Center (7/11)

A. Dove, M. Horányi, A. Poppe, S. Robertson, X. Wang, Photoemitting Dusty Surfaces in Space, 6th International Conference on the Physics of Dusty Plasmas, Garmisch-Partenkirchen, Germany, (6/11)

A. Dove, S. Robertson, X. Wang, A. Poppe, Z. Sternovsky, M. Horányi, Characterization of a laboratory simulated lunar photoelectron sheath, 42nd LPSC, The Woodlands, TX (3/11)

A. Dove, Z. Sternovsky, Z. Wang, S. Robertson, M. Horányi, Laboratory investigations of the UV-generated lunar photoelectron sheath, URSI, Boulder, CO (1/11)

A. Dove, Z. Sternovsky, X. Wang, S. Robertson, C. Lapansé, M. Horányi, A. Collette,

Experimental investigations of the lunar photoelectron sheath, AGU, San Francisco, CA (12/10)

A. Dove, S. Robertson, X. Wang, Z. Sternovsky, M. Horányi, Physics of the lunar photoelectron sheath, 3rd NASA Lunar Science Forum, NASA Ames Research Center (7/10)

A. Dove LunGradCon 2010 Overview presentation: Science FROM the Moon, 1st Annual LunGradCon, NASA Ames Research Center (7/10)

Z. Sternovsky, M. Horányi, E. Grün, S. Robertson, X. Wang, **A. Dove**, T. Munsat, A. Poppe, N. Duncan, S. Auer, Investigation of near-surface lunar dust transport in the laboratory, COSPAR, Bremen, Germany (7/10)

A. Dove, S. Dickson, S. Robertson, Z. Sternovsky, X. Wang, M. Horányi, Characterization of a UV-generated photoelectron sheath, 41st LPSC, The Woodlands, TX (3/10)

A. Dove, X. Wang, S. Robertson, M. Horányi, J. Devaud, M. Crowder, A. Lawitzke, Mitigation of lunar dust adhesion by surface treatment, AGU, San Francisco, CA (10/09)

S. Dickson, **A. Dove**, M. Horányi, T. Munsat, S. Robertson, Z. Sternovsky, X. Wang, Lunar photoemission studies with a Xe-excimer UV lamp, AGU, San Francisco, CA (12/09)

A. Dove, J. Burns, LUNAR Road Trip: Excursion in a pressurized rover to emplace a far-side radio telescope array near the South Pole, 2nd NASA Lunar Science Forum, NASA Ames Research Center (7/09)

A. Dove, B. Toon, J. Heldmann, Observations and modeling of the mass and energy balance of terrestrial snowpacks to constrain martian snowpack models, 40th LPSC, Houston, TX (3/09)